Article

Ectopic NMDAR expression in cancer unmasks germline-encoded autoimmunity

Check for updates

Sam O. Kleeman[1], Kevin Michalski[1,6], Xiang Zhao[1,6], Ruben Steigerwald[1], Miriam Ferrer[1], Llewelyn Levett[1], Ethan Ertel[1], Austin Schultz[1,2], Noriko Simorowski[1], Pamela Moody[1], Tse-Luen Wee[1], Cristina Valente[3], Sharon Fox[3], Mateusz Makuch[4,5], Selina Thomsen[4], Ruby Harrison[5], Claire Regan[1], Jonathan Preall[1], Qing Gao[1], Dennis Thomas[1], Jill Habel[1], Rachel Rubino[1], Sarosh Irani[4,5] ✉, Hiro Furukawa[1,7] ✉ & Tobias Janowitz[1,2,7] ✉

Autoimmunity and anti-cancer immunity lie on the same biological continuum[1,2], but their link remains obscure. The paraneoplastic neurological syndrome ANRE (anti-NMDA receptor (NMDAR) encephalitis) is a paradigm for their connectivity[3], given that intratumoural NMDAR expression is correlated with the generation of anti-NMDAR antibodies[4,5]. Here we verify ectopic expression of GluN1 and GluN2B NMDAR subunits in triple-negative breast cancer (TNBC)[6] and model this using orthotopic TNBC tumours with inducible expression of GluN1–GluN2B NMDARs. We show that NMDAR expression is sufficient to induce the recruitment of B cells and their affinity maturation, consistent with an integrated adaptive immune response. Reconstruction of extended intratumoural B cell phylogenies and cryogenic electron microscopy structural analyses demonstrate that affinity-matured hypermutated and class-switched antibodies emerged from pre-existing germline-configuration lower-affinity anti-NMDAR antibodies. Distinct matured antibodies targeted specific epitopes and induced conformational rearrangements within the NMDAR amino-terminal domain, predictive of their functional effects, ranging from inhibition to potentiation. Passive transfer of an NMDAR-potentiating antibody caused autonomic dysregulation and lowered the seizure threshold in healthy female mice, recapitulating key diagnostic criteria of ANRE[4,5]. We further identify a correlation between intratumoural NMDAR expression and anti-NMDAR antibody titres in patients with TNBC. Taken together, our data establish a direct connection between intratumoural NMDAR expression, antibody maturation and the onset of autoimmunity. These findings suggest that germline-encoded anti-NMDAR antibodies contribute to immune surveillance but can also trigger autoimmune disease after maturation, revealing a mechanistic trade-off between cancer immunity and neurotoxicity.

The adaptive immune system evolved to distinguish between self and non-self[7]. Nevertheless, immune responses against the self (that is, autoimmunity) occur, but their origin remains unclear[8]. In paraneoplastic syndromes, ectopic intratumoural expression of non-mutant self-proteins triggers antibody-mediated autoimmune disease[9]. These autoantigens typically have restricted expression in immunologically privileged sites, such as the central nervous system[4,10] (onconeural antigens)[11]. Germline-configuration antibodies[12] with low-affinity self-binding have been described[13–15] but not traced to disease-causing high-affinity antibodies.

Paraneoplastic autoantibodies can modulate the host, for example, by altering neuronal function, and the tumour, for example, by restraining tumour growth and metastasis[16]. In fact, spontaneous tumour regression has even been observed after the onset of autoimmunity[17].

It is accepted that both antibody- and T-cell-mediated immunity synergize to drive immune control of tumours[18]. Therapies that activate T-cell-mediated immunity can precipitate considerable antibody-mediated neuronal autoimmunity[19] that correlates with improved anti-tumour efficacy[20].

These observations suggest ectopic onconeural antigen expression recruits germline-configuration B cells, which undergo affinity maturation in tertiary lymphoid structures[21] to generate high-affinity IgG autoantibodies[22] that cross the blood–brain barrier (BBB). However, whether onconeural autoantibodies are causative of autoimmunity remains unclear[23]. For example, ANRE is characterized by autoantibodies targeting the NMDAR and a stereotypical clinical syndrome[3–5]. NMDARs are voltage-dependent cation channels activated by glycine and glutamate[24]. They comprise two GluN1 subunits (encoded by *GRIN1*)

[1]Cold Spring Harbor Laboratory, Cold Spring Harbor, NY, USA. [2]Northwell Health, Manhasset, NY, USA. [3]Department of Pathology and Laboratory Medicine, Donald and Barbara Zucker School of Medicine at Hofstra/Northwell, Manhasset, NY, USA. [4]Departments of Neurology and Neurosciences, Mayo Clinic, Jacksonville, FL, USA. [5]Oxford Autoimmune Neurology Group, Nuffield Department of Clinical Neurosciences, University of Oxford, Oxford, UK. [6]These authors contributed equally: Kevin Michalski, Xiang Zhao. [7]These authors jointly supervised this work: Hiro Furukawa, Tobias Janowitz. ✉e-mail: furukawa@cshl.edu; janowitz@cshl.edu

Article

and two GluN2 subunits (*GRIN2A*–*GRIN2D*) and/or GluN3 subunits (*GRIN3A*–*GRIN3B*)[24,25] and mediate synaptic plasticity in the central nervous system[26]. ANRE is correlated with the expression of NMDAR in multiple tumour types, including ovarian, breast and pancreas[5], and is associated with the production of high-affinity anti-NMDAR IgG antibodies[15] from tertiary lymphoid structures[22]. The anti-NMDAR humoral response constrains tumour growth[4,27] but is also associated with a debilitating neuropsychiatric syndrome characterized by psychosis, autonomic dysregulation (hyperthermia) and epileptic seizures[3–5]. Here using a mouse model of NMDAR-expressing cancer, we define how germline-encoded NMDAR-binding antibodies undergo affinity maturation to modulate receptor function, thereby constraining tumour growth and engendering neurological disease.

GluN1–GluN2B expression in TNBC

NMDAR expression has been detected in human breast cancer and is enriched in TNBC[6]. We reanalysed RNA-sequencing (RNA-seq) data from the METABRIC and TCGA breast cancer cohorts, and identified a subset of tumours that express both *GRIN1* and *GRIN2B* (Extended Data Fig. 1a). *GRIN1* expression was significantly higher in oestrogen receptor (ER)-positive tumours, whereas *GRIN2B* expression was higher in TNBC ($P = 4.98 \times 10^{-13}$; Extended Data Fig. 1b,c), consistent with reported ER-mediated repression of *GRIN2B*[28] (Extended Data Fig. 1d). We next performed spatial RNA profiling (10x Visium HD) on a TNBC tumour section (Fig. 1a), classifying bins into eight cell types (Fig. 1b,c and Extended Data Fig. 1e). *GRIN2B* transcripts were exclusively detected in the cancer cell cluster (fold change = 4.31, $P = 1.13 \times 10^{-170}$ versus other clusters), while *GRIN2C* could be detected at a lower level in endothelial cells, as observed previously[29] (Fig. 1d). *GRIN1* RNA expression was low, consistent with the findings from bulk tumour profiling (Extended Data Fig. 1b). Cancer cells also expressed NMDAR scaffold protein GKAP (encoded by *DLGAP1*) (Fig. 1e, $P < 1 \times 10^{-300}$ versus other clusters), which mediates NMDAR-dependent pro-invasive signalling[30]. Immunofluorescence (IF) analysis using the antibodies 003-102 (GluN1 amino-terminal domain (ATD))[31] and IgG2 (GluN2B ATD)[32] confirmed protein expression in 1–2% of tumour cells (Fig. 1f, compare with Supplementary Fig. 2a,b). Together, these results validate the expression of GluN1 and GluN2B NMDARs in cancer cells of human TNBC tumours.

NMDAR-induced B cell reaction

NMDAR expression is an emergent feature of tumour progression[6]. No immunocompetent mouse models of TNBC are known to express NMDAR. We hypothesized that NMDAR subunits that are not expressed by medullary thymic epithelial cells (mTECs) would be immunogenic when ectopically expressed. Reanalysis of human mTEC data[33] confirmed that *GRIN1* and *GRIN2B* are not expressed by mTECs (Extended Data Fig. 1f). By contrast, *GRIN2A* and *GRIN2D* were found to be expressed by lineage-specific mimetic TECs (mTECs)[34]. We established a mouse TNBC model using 4T1 cells[35] with doxycycline (DOX)-inducible GluN1–GluN2B expression (4T1-NMDAR) (Fig. 2a,b, Extended Data Fig. 2a and Supplementary Table 1). As expected with a DOX-inducible system, we observed low background expression, and marked RNA (Fig. 2b; fold change = 32.1, $P = 3.53 \times 10^{-7}$), protein (Fig. 2c; unprocessed blots are provided in Supplementary Fig. 1) and cell-surface (Fig. 2d) induction of GluN1–GluN2B after 48 h of DOX treatment. To model induction of GluN1–GluN2B expression during cancer progression, 4T1-NMDAR cells were implanted into immunocompetent female BALB/cJ mice (Fig. 2a (right)) and DOX was added to the drinking water. scRNA-seq analysis of CD45⁻ tumour cells ($n = 2,176$ cancer cells; Extended Data Fig. 2b–e) revealed a cluster with high *Grin1-Grin2b* (hereafter, *Grin1-2b*) expression (fold change = 12.5, $P = 3.62 \times 10^{-23}$) that showed elevated proliferation markers (*Mki67*, G2/M genes), consistent with previous reports[6,30,36]. We further detected gene expression of the cystine-glutamate antiporter xCT (encoded by *Slc7a11*) in a minority of cancer cells and a significant fraction of tumour-infiltrating neutrophils (Extended Data Fig. 2f; fold change = 100, $P = 6.24 \times 10^{-139}$ versus other clusters), as has been previously suggested[37], potentially enabling glutamate efflux and paracrine NMDAR signalling[6,36]. Serial staining of excised 4T1-NMDAR tumours confirmed *Grin1-2b* RNA expression and membranous GluN2B protein expression (Fig. 2e).

We monitored anti-NMDAR antibody titres using an enzyme-linked immunosorbent assay (ELISA). The titres peaked within 2 weeks of DOX-mediated NMDAR induction (Fig. 2f). In all three mice exhibiting titres over 500 ng ml⁻¹ (Fig. 2f), we observed spontaneous tumour regression following peak antibody levels (Fig. 2g), demonstrating that NMDAR expression is highly immunogenic and mirroring clinical features of ANRE. Bulk RNA-seq analysis demonstrated B and T cell and macrophage enrichment, and chemokine signatures indicated tertiary lymphoid structure formation (Extended Data Fig. 3a,b). IF analysis confirmed peritumoural B-cell-enriched lymphoid aggregates in DOX-treated tumours ($n = 3$) but not in the controls (Fig. 2h–i and Extended Data Fig. 3c). Furthermore, growth kinetics were significantly suppressed in DOX-treated tumours (Extended Data Fig. 3d). Together, these findings demonstrate that ectopic expression of canonical mouse NMDAR in cancer cells is highly immunogenic and sufficient to unmask robust adaptive immune responses, including anti-NMDAR humoral immunity.

Germline antibodies retain NMDAR binding

To confirm the specificity of the antibodies derived from the B cells detected in 4T1-NMDAR tumours, we isolated NMDAR-binding intratumoural B cells (Fig. 3a (top)), which showed enrichment of antigen-experienced cells relative to tumour-draining lymph node (TDLN)-derived B cells (Supplementary Fig. 3a–c). From mice with elevated titres (≥500 ng ml⁻¹), we sorted CD19⁺ B cells (2% of CD45⁺) and enriched NMDAR-binding cells (6% of B cells) using oligonucleotide-tagged recombinant NMDAR (Fig. 3a and Supplementary Fig. 3d). We sequenced 3,180 NMDAR-binding B cells, identifying naive, pre-GC, GC, pre-plasmablast (pre-PB) and antibody-secreting cell (ASC) states (Fig. 3b and Extended Data Fig. 3e). B cells segregated into B1 (*Bhlhe41*high) and B2 (*Fcer2a*high) subsets[38], with *Bhlhe41*[39] increasing stepwise through differentiation (Fig. 3b and Extended Data Fig. 3e). All pre-PBs and ASCs were *Bhlhe41*high and *Fcer2a*low.

We assembled BCR phylogenies to trace affinity-matured antibodies back to germline precursors (unmutated common ancestors), screening clonotypes with evidence of class switching and NMDAR binding (Methods and Extended Data Fig. 4a–c). We selected four clonotypes with evidence of NMDAR–oligo capture (Fig. 3c), from which we selected one representative germline and one matured sequence (annotated as G and M, respectively, in Fig. 3c). Germline sequences were imputed (Supplementary Figs. 4 and 5), except for SK5A, which was directly detected. All clonotypes showed somatic hypermutation. SK5A had four class-switching events (Fig. 3c). SK5A/SK5B originated from one mouse, with others arising from different mice (Extended Data Fig. 3f). Within the expanded clonotypes (3D, 5A and 5B), we identified cells with B1, B1–B2 intermediate and B2 differentiation (Fig. 3d and Extended Data Fig. 3g), concordant with previously reported plasticity in B1–B2 differentiation status[38]. Consistent with the loss of membrane-bound BCR expression during plasma cell differentiation, affinity maturation was not always associated with increased capture of oligo-labelled NMDAR (Extended Data Fig. 3h).

Recombinant expression and ELISA confirmed GluN1–GluN2B binding for germline and matured antibodies from all four clonotypes (Fig. 3a (bottom)), in comparison to the non-binding control (mGO53 (ref. 40); Fig. 3e). No binding was detected for BSA or known targets of polyspecific antibodies (double-stranded DNA, insulin, lipopolysaccharide; Extended Data Fig. 4d and Supplementary Table 2).
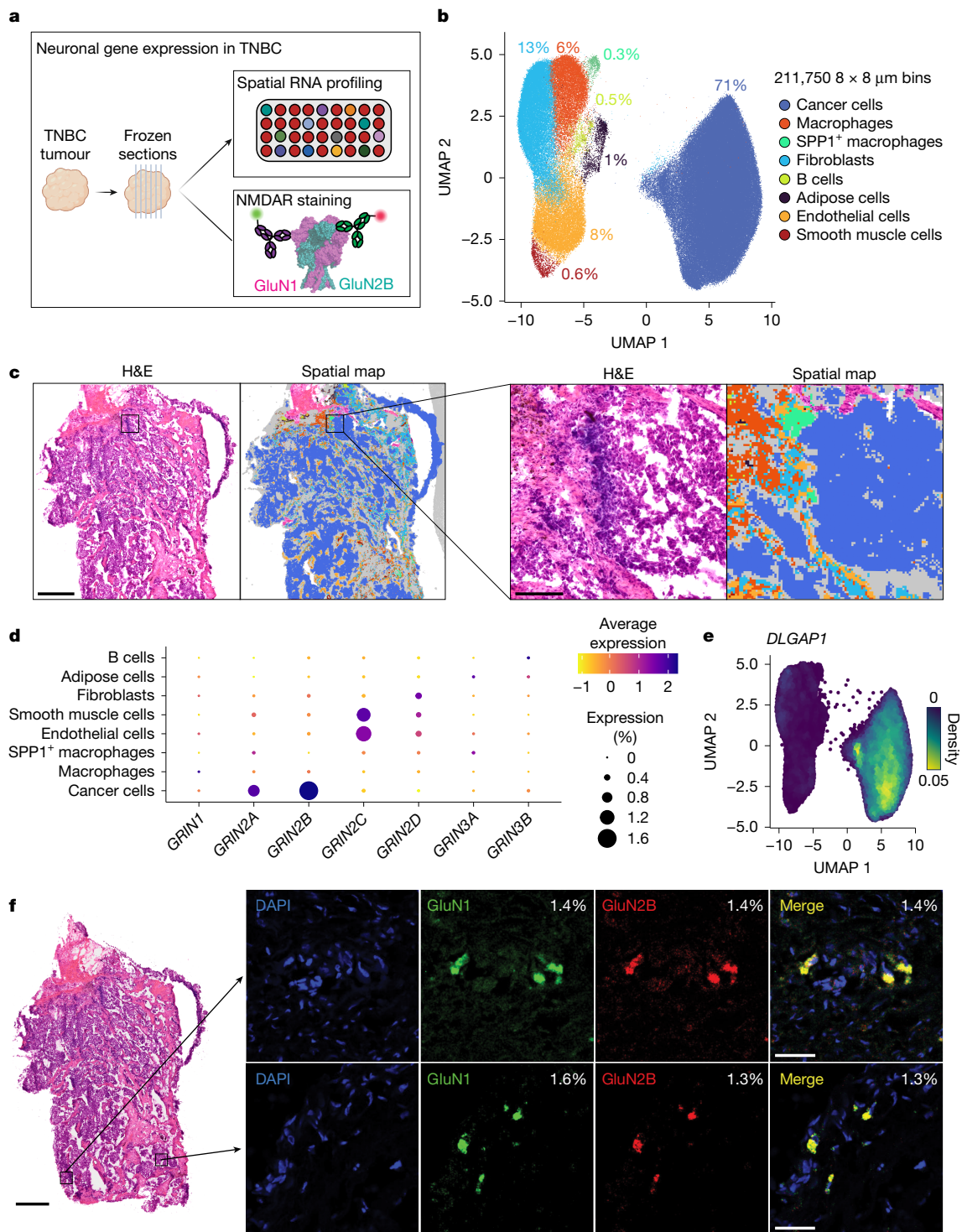
Fig. 1 | Detection of GluN1–GluN2B in human TNBC. a, Schematic of the experimental design. NMDAR expression in a TNBC section is characterized by spatial RNA profiling and IF using validated antibodies specific to the ATDs of GluN1 and GluN2B. The diagram was created using BioRender; Kleeman, S. https://BioRender.com/pw3zhmn (2026). **b,** Uniform manifold approximation and projection (UMAP) of 211,750 8 × 8 μm bins, annotated with cell type (*n* = 8) and the proportion of bins classified into each cell type. **c,** Low- and high-power TNBC section projections depicting the spatial alignment of cell clusters to haematoxylin and eosin (H&E) stain. The rectangular box depicts the single representative slide region captured in the Visium CytAssist workflow. **d,** The scaled gene expression (point colour) and percentage of expressing cells (point size) for each NMDAR gene–cell type pair. **e,** Feature plot showing UMAP projection of 8 × 8 μm bins (as described in **b**) annotated with the density of *DLGAP1* (encoding an NMDAR-associated postsynaptic scaffold protein) gene expression. **f,** High-power fields of TNBC sections stained with fluorescent antibodies to GluN1 (green) and GluN2B (red). The percentage of DAPI-positive cells in each high-power field is indicated. These fields are representative of at least five clusters of NMDAR expression in this sample. Scale bars, 1 mm (**c** (left) and **f** (left)), 40 μm (**f** (right)) and 200 μm (**c** (right)).
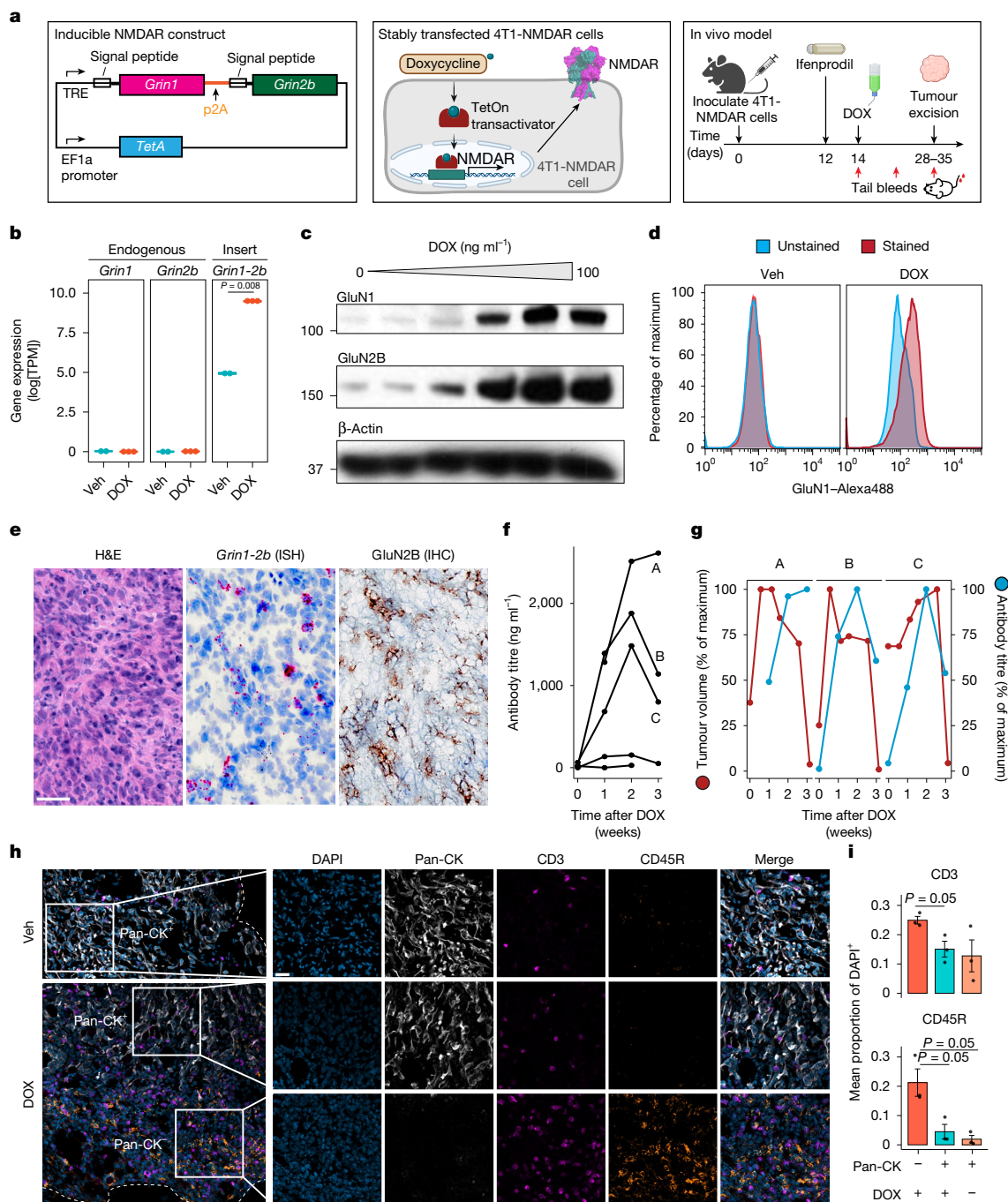
Fig. 2 | Inducible expression of GluN1–GluN2B causes humoral immunity in mouse TNBC. a, Schematic of the experimental design. A doxycycline (DOX)-inducible construct containing a *Grin1-2b* insert sequence was used to stably transfect mouse 4T1 TNBC cells, resulting in the derivation of a 4T1-NMDAR cell line. Mice were inoculated with 4T1-NMDAR cells, and receptor expression was induced by the addition of DOX to drinking water in the presence of ifenprodil. Tumour growth kinetics and plasma antibody titres were monitored longitudinally. The diagram was created using BioRender; Kleeman, S. https://BioRender.com/k95v418 (2026). **b**, RNA expression (RNA-seq) of endogenous *Grin1* and *Grin2b* in comparison to the exogenous *Grin1-2b* insert in 4T1-NMDAR cells treated in vitro with vehicle (veh) or DOX (10 ng ml⁻¹). Data are mean ± s.e.m. $n = 2$ (vehicle) and $n = 3$ (DOX). Statistical analysis was performed using unadjusted two-sided one-sample t-tests. **c**, Immunoblot analysis of protein expression of GluN1 and GluN2B relative to β-actin (sample processing control) in cell lysates derived from 4T1-NMDAR cells treated in vitro with 0–100 ng ml⁻¹ DOX. **d**, Flow cytometry histograms of 4T1-NMDAR cells treated in vitro with vehicle or 10 ng ml⁻¹ DOX and stained (red) with an Alexa488-conjugated

GluN1-specific antibody (003-102) or left unstained (blue). All analyses were performed after 48 h of DOX exposure. **e**, Aligned serial 4T1-NMDAR mouse tumour sections stained with H&E and for the *Grin1-2b* insert RNA and GluN2B. **f**, Longitudinal anti-NMDAR antibody titres in five mice inoculated with 4T1-NMDAR tumours after induction of NMDAR expression. **g**, Antibody titres (blue), as shown in **f**, superimposed with tumour volumes (red) over time. **h**, Representative IF staining for T (CD3), B (CD45R and B220) and epithelial (pan-CK) cells in pan-CK-positive and pan-CK-negative regions of the tumour margin in 4T1-NMDAR tumours sampled after DOX or vehicle treatment for 2 weeks. The tumour margin is indicated with a white dashed line. **i**, Quantification of T and B cells as the proportion of DAPI-positive cells in high-power fields (as shown in **h**) stratified by pan-CK expression and treatment group. Data are mean ± s.e.m. $n = 3$ mice per group (one ×20 high-power field per mouse). Statistical analysis was performed using unadjusted two-sided one-sample t-tests; *$P < 0.05$, **$P < 0.01$, ***$P < 0.001$. Scale bars, 50 μm (**e**) and 20 μm (**h**).
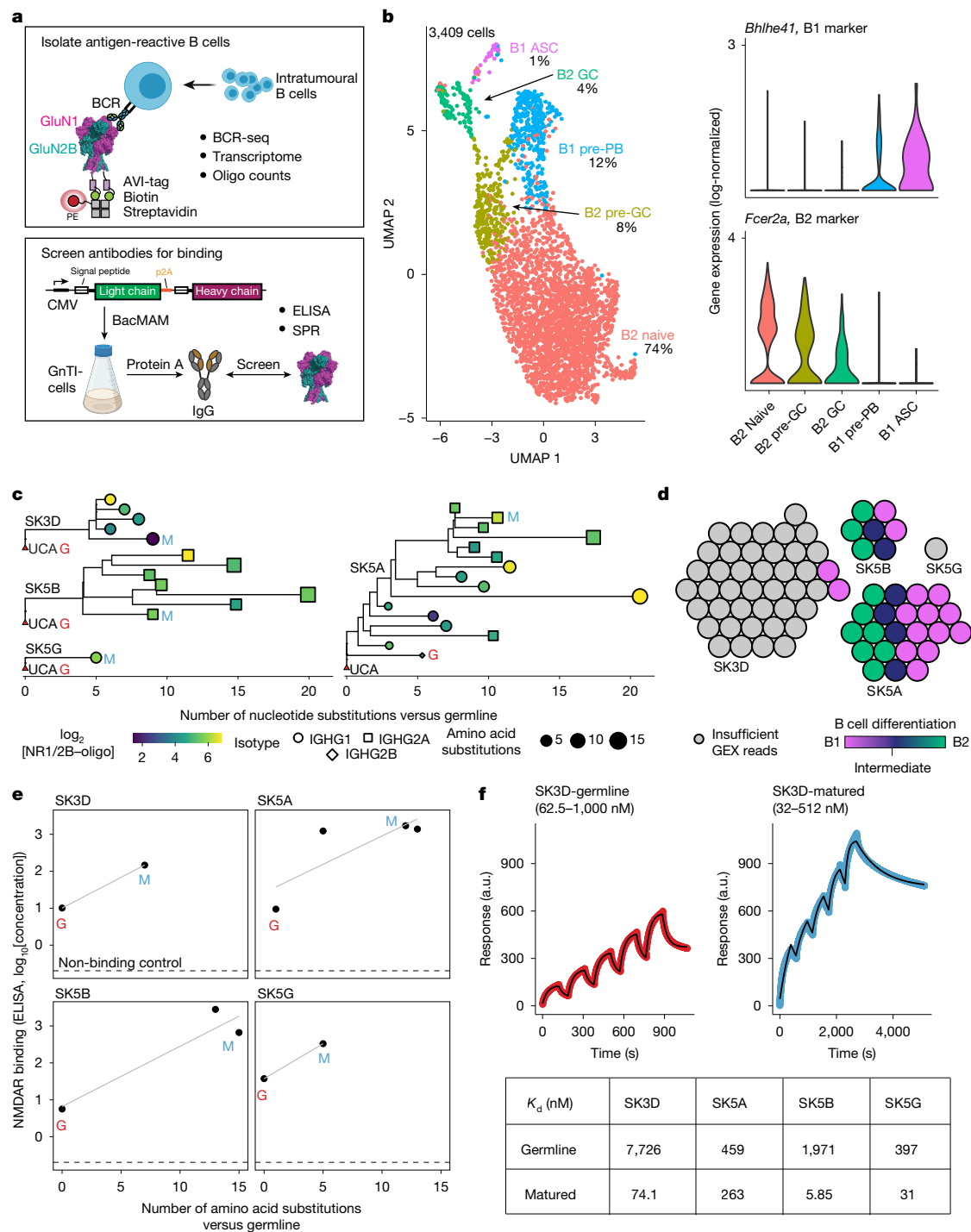
Fig. 3 | Intratumoural NMDAR affinity maturation traces to germline-encoded B cell receptors. a, Schematic of the experimental design. Intratumoural B cells were incubated with GluN1–GluN2B NMDARs labelled with Streptavidin-PE-Oligo conjugates before single-cell sequencing. B cell phylogenies (clonotypes) were reconstructed by multiple-sequence alignment. Recombinant monoclonal antibodies were screened for NMDAR binding by ELISA and SPR. The diagram was created using BioRender; Kleeman, S. https://BioRender.com/z44f766 (2026). **b**, UMAP projection of intratumoural B cells annotated with differentiation state (Extended Data Fig. 3e), as well as density of canonical B1 (*Bhlhe41*) and B2 (*Fcer2a*) marker gene expression. GC, germinal centre. **c**, Extended phylogenies (*n* = 4 clonotypes) of NMDAR-reactive B cells identified by single-cell B cell sequencing. Each B cell clone is signified by a tip on the tree, with the size, shape and colour reflecting the number of amino acid substitutions, antibody isotype and oligo counts (reflecting capture of NMDAR), respectively. The length of each branch signifies the number of nucleotide

substitutions versus the unmutated common ancestor (UCA). For each clonotype, a representative germline (G) and matured (M) sequence was selected for further characterization. **d**, B cell clones in each clonotype annotated with their transcriptional B1/B2 differentiation status, in cases in which sufficient transcriptional data were captured. 'Intermediate' refers to cells with features of B1 and B2 status. **e**, Correlation between the relative NMDAR-binding affinity (ELISA) and the number of amino acid substitutions in each clonotype, with germline and matured sequences indicated. The non-binding control (mGO53) threshold is shown. All antibodies were added at a concentration of 1,000 ng ml⁻¹. **f**, Representative SPR traces for single-cycle kinetic assays using twofold dilutions in the indicated concentration ranges (*n* = 1 cycle per antibody) for SK3D-germline and SK3D-matured (top). The fitted kinetic model is indicated in black. The table (bottom) shows the measured K_d (nM) for the representative germline and matured sequences in each B cell phylogeny.

Article

Amino acid substitutions correlated with NMDAR binding (Fig. 3e). To precisely measure binding kinetics and binding affinity (dissociation constant (K_d)), we performed SPR by single-cycle kinetics for the selected representative germline and matured antibodies in each clonotype (Fig. 3f). NMDAR was bound by all tested germline antibodies (K_d range, 397–7,726 nM) and matured antibodies (K_d range, 5.85–263 nM), confirming that antibody maturation correlated with significantly increased affinity (Fig. 3f, Extended Data Fig. 5a,b and Supplementary Table 3). These values are comparable to those measured for antibodies derived from patients with autoimmune disorders[13].

Given the high frequency of naive B cells in the TDLNs (Supplementary Fig. 3b) and evidence that intratumoural B cells can be seeded from TDLNs[41], we hypothesized that NMDAR-binding B cells in germline configuration could be preferentially isolated from TDLNs. Unsupervised clustering of 4,036 TDLN-derived B cells revealed multiple B cell differentiation states (Extended Data Fig. 4e,f) but an absence of *Prdm1*-high ASCs, consistent with TDLN flow cytometry (Supplementary Fig. 3b). In contrast to intratumoural B cells (Fig. 3b), TDLN-derived B cells with evidence of NMDAR–oligo capture were predominantly unmutated naive B cells (Extended Data Fig. 4g,h). To screen for putative NMDAR-reactive germline configuration antibodies, we selected 31 unmutated sequences from naive B cells with high NMDAR–oligo capture and confirmed binding for two unmutated antibodies (Extended Data Fig. 4i). Together, these findings demonstrate that NMDAR-reactive B cells arise from germline-configuration naive B cells that bind to NMDAR.

Cryo-EM reveals epitope convergence

To determine the landscape of NMDAR epitopes across the four tumour-derived NMDAR-binding clonotypes, we performed cryogenic electron microscopy (cryo-EM) analysis of the selected matured and germline anti-NMDAR antibodies (Supplementary Figs. 4 and 5) in a complex with GluN1–GluN2B (Fig. 4, Supplementary Figs. 6 and 7 and Supplementary Tables 4 and 5). The samples were prepared with in the presence of the agonists glycine and glutamate. For the matured antibodies, the overall resolution ranged from 3.09 to 4.10 Å, while the resolution of a local refinement of the ATD heterodimer–antibody complex ranged from 2.99 to 4.08 Å (Supplementary Table 4). For the germline antibodies, the overall resolution ranged from 3.68 to 4.52 Å, while the local refinement resolution ranged from 3.70 to 5.82 Å, consistent with lower-affinity binding interactions. Owing to conformational heterogeneity in the ATD-1 heteromer (chains C/D) for SK5A-matured, SK3D-germline and SK3D-matured, models were fit to local refinements of the ATD-2 heteromer. By fitting models using the higher-resolution matured refinements and using these as templates to model the germline refinements, we were able to accurately determine binding residues involved in antibody binding (Fig. 4c,f).

All antibodies exhibited binding to the NMDAR ATD, as has been previously reported for patient-derived antibodies[31,42]. Consistent with our unbiased antibody selection approach, we found that epitopes were evenly distributed between GluN1 and GluN2B, with two antibodies (SK3D and SK5A) binding to the GluN1–GluN2B ATD R1 lobe interface (Fig. 4a,b,d,e and Extended Data Fig. 6a–c). All clonotypes had distinct binding epitopes on NMDAR, but some residues, such as GluN2B Tyr322, were involved in binding to more than one antibody (SK3D and SK5A). Several antibodies showed evidence of binding to flexible loops that are poorly resolved in IgG-free NMDAR structures[43]. In general, we observed a greater number of residue–residue interactions for affinity-matured versus germline-encoded antibodies. In the SK3D clonotype, both germline and matured antibodies bound to an overlapping epitope in the GluN1–GluN2B ATD R1 lobe interface. Affinity maturation was correlated with local conformational rearrangements leading to improved coordination of GluN1 Gln73, GluN2B Tyr322 and heavy-chain Tyr54 (CDR2; Supplementary Fig. 4a), which would be expected to further

stabilize binding (Extended Data Fig. 6d). In the SK5A clonotype, both germline and matured antibodies bound to an overlapping epitope in the GluN1–GluN2B ATD R1 lobe interface. As a potential explanation for the increased affinity, we observed the coordination of GluN2B Arg84, GluN2B Asp87 and light-chain Tyr49 (CDR2, Supplementary Fig. 4b and Extended Data Fig. 6d). In the SK5B clonotype, we found non-overlapping epitopes and paratopes between the germline and matured sequences. We detected weak binding of the germline antibody to the GluN2B ATD R1 lobe, with a comparatively small interaction surface (Extended Data Fig. 6b), comprising an electrostatic interaction between GluN2B Glu326 and light-chain Arg65 (Supplementary Fig. 5a). By contrast, we detected clear binding of the SK5B-matured to the GluN1 ATD amino terminal end (Extended Data Fig. 6d). This epitope diversification (epitope spreading) represents intramolecular spreading that can cause autoimmune disease[44]. In the SK5G clonotype, both germline and matured antibodies bound to an overlapping epitope in the GluN2B R1 lobe. Increased coordination between heavy chain Tyr108 (CDR3; Supplementary Fig. 5b) and GluN2B Arg92 may partly explain the increased affinity (Extended Data Fig. 6d).

To investigate the translational relevance of our findings, we isolated seven related IgG1 B cells from a patient with ANRE (OX1). We selected one representative matured antibody from this group (OX1-matured) and its imputed germline precursor (OX1-germline) for further analysis (Supplementary Fig. 8a). The OX1-matured antibody, expressed as a Fab fragment, displayed strong binding to NMDAR with a K_d of 83.7 nM (Extended Data Fig. 5a). Cryo-EM analysis was conducted for both OX1-matured and OX1-germline antibodies in a complex with GluN1–GluN2B NMDAR proteins. The cryo-EM maps achieved overall/local resolutions of 4.20/3.42 Å for OX1-matured and 4.55/5.24 Å for OX1-germline (Supplementary Fig. 8b,c and, Supplementary Tables 4 and 5). Both antibodies bound specifically to an overlapping epitope in the R2 lobe of the GluN1 ATD (Extended Data Fig. 6f,g).

The structural comparison of NMDAR epitopes from both mouse and human antibody–NMDAR complexes, including previously reported structures[31,42] and those described in this Article, reveals clear epitope convergence to the NMDAR ATD (Extended Data Fig. 7a). First, the epitopes of the patient-derived antibodies OX1 and 003-102 (refs. 15,31) directly overlap, with both antibodies forming polar interactions with Arg260 (Extended Data Fig. 7b,c). Second, the epitope for SK5B-matured in the GluN1 ATD R1 lobe directly overlaps with three previously characterized patient-derived antibodies: 008-218[15,31], 007-168 (refs. 15,31) and 2G7 (ref. 42) (Extended Data Fig. 7d). Notably, GluN1 Lys51, which is highly exposed to the extracellular environment, sits within the epitope of each antibody and forms interactions with residues from all three (Extended Data Fig. 7e), suggesting that it constitutes part of an immunodominant epitope. Third, both SK5A and SK3D bind to the GluN1–GluN2B interface, consistent with evidence that, in select cases, patient-derived antibodies bind selectively to GluN1–GluN2B ATD heteromers but not to GluN1 ATD or GluN2B ATD alone[45]. In summary, we characterized the diversity of intraclonotype and interclonotype epitopes from tumour-derived antibodies and demonstrated cross-species convergence to the GluN1–GluN2B ATD epitope.

Anti-NMDAR antibodies differ functionally

Functional NMDAR transitions involve conformational changes[46]. Multiple closed-channel states exist: non-active (closed conformation)[43,46,47] and pre-active (primed for opening with compact ATD–ligand-binding domain (LBD) assembly)[43,46]. The transition from non-active to pre-active states reduces distances between GluN2B Arg184 and GluN1 Lys178 (α4′–α5) and GluN2B Leu425 and GluN1 Arg489 (L1′–L2) (Fig. 5a (left)). Allosteric NMDAR modulators, such as ifenprodil, are known to stabilize specific states[46–49]. We aimed to characterize the structural and functional consequences of antibody binding by measuring the α4′–α5 and L1′–L2 distances in antibody-bound structures.
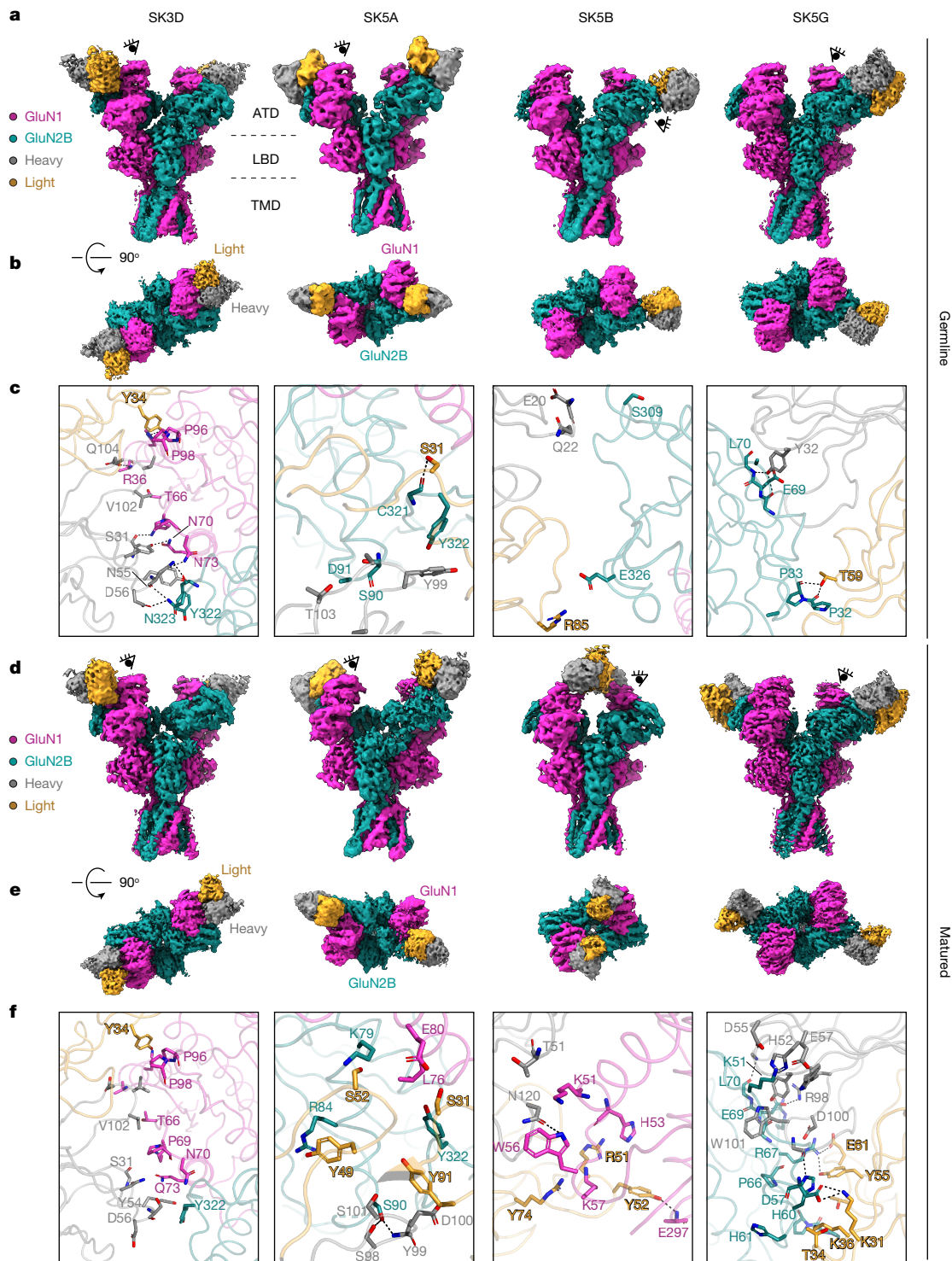
Fig. 4 | Cryo-EM structures of NMDARs in a complex with tumour-derived antibodies. a,b, Cryo-EM densities for four representative germline sequences from antibody clonotypes: SK3D (IgG), SK5A (Fab), SK5B (IgG) and SK5G (IgG) in a complex with GluN1–GluN2B NMDARs. Note that there was clear cryo-EM density only for the Fv regions of the Fabs. **c**, A focused view of the interaction interface between the GluN1–GluN2B NMDAR and the germline antibodies. **d,e**, Cryo-EM densities for four representative mature sequences from antibody clonotypes: SK3D (IgG), SK5A (IgG), SK5B (IgG) and SK5G (IgG) in a complex with GluN1–GluN2B NMDARs. **f**, A focused view of the interaction interface

between the GluN1–GluN2B NMDAR and the matured antibodies. For **a** and **d**, cryo-EM density is viewed from the side. For **b** and **e**, cryo-EM density is shown from the top of the extracellular domain. For **c** and **f**, structural models are shown for the residue-level interactions between IgG variable regions and NMDARs annotated with amino acid positions. These models were built using locally refined maps of the interaction interface. The constant regions of each IgG were not clearly visualized and were therefore omitted for clarity. The dashed lines indicate polar interactions. Eye symbols signify the position of the viewpoints shown in **c** and **f**.

SK3D-matured-bound (all) and SK5A-matured-bound (minor population, around 25%; Supplementary Fig. 9) receptors adopted a previously uncharacterized conformation (hereafter, pre-active2) for NMDARs

characterized by a reduced α4′–α5 distance in the ATD-1 heteromer only without shortening of the L1′–L2 distances in the LBD (Fig. 5b). Compared with the non-active state (Protein Data Bank (PDB): 9arg),
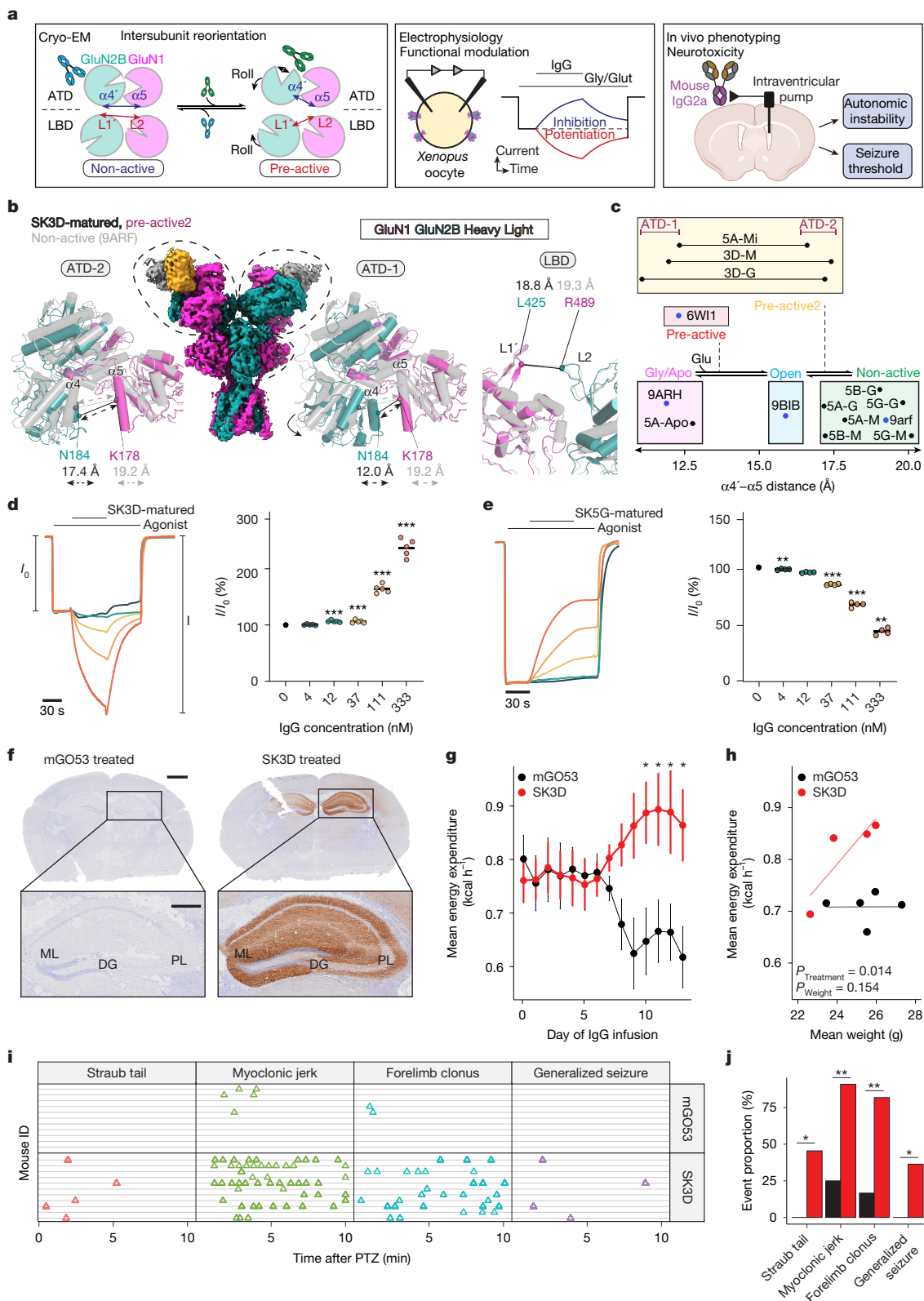
Fig. 5 | See next page for caption.

the pre-active2 state undergoes a conformational alteration in one of the two GluN1–GluN2B ATD dimers represented by reorientation of GluN2B ATD-1 relative to GluN1 ATD-1 (Fig. 5b, Extended Data Fig. 8a,b and Supplementary Video 1). This reorientation is associated with the opening (by around 14°) of the GluN2B ATD clamshell for both ATD-1 and ATD-2 (Extended Data Fig. 8c), which is known to be

coupled to intersubunit ATD rearrangement[47,50]. We envisage that the pre-active2 conformation might reflect an intermediate state between the open and non-active states. The pre-active2 conformation was also detected for the SK3D-germline-bound receptors (Extended Data Fig. 8d), but not the SK5A-germline-bound receptors. To investigate the prevalence of the pre-active2 state in the SK3D-germline dataset, we

Fig. 5 | Binding of tumour-derived antibodies modifies NMDAR structure and function. a, Schematic of the experimental design. Left, cryo-EM models revealed whether antibodies stabilized inhibitory (non-active) or activating (pre-active) NMDAR states. Transition to the pre-active state involves GluN2B ATD rolling down and LBD rolling up relative to GluN1, and the GluN2B ATD clamshell opening (black arrow). Middle, two-electrode voltage clamp (TEVC) analysis of GluN1–GluN2B-expressing *Xenopus laevis* oocytes was used to measure agonist-induced currents with or without tumour-derived recombinant IgG. Right, after intraventricular infusion of murinized IgG, autonomic instability (hyperthermia) and seizure activity were quantified. The diagram was created using BioRender; Kleeman, S. https://BioRender.com/y52i094(2026). **b**, Asymmetric conformational rearrangement (pre-active2) of GluN1 and GluN2B ATD subunits induced by SK3D-matured binding to the GluN1–GluN2B interface, showing the Asn184–Lys178 distance (α4′–α5; Supplementary Video 1). The LBD conformation (Leu425–Arg489 distance) versus the non-active conformation (PDB: 9arf; grey) is shown for comparison; the dashed lines indicate each measurement. **c**, The α4′–α5 distance (*x* axis) for each modelled antibody–receptor complex (black dots) versus previously published structures (blue dot, annotated with PDB IDs). Pre-active and pre-active2

represent intermediate states with increased channel activities. ATD-1 (chains C/D) and ATD-2 (chains A/B) measurements are shown for asymmetric pre-active2 models. Mi, minor population. **d,e**, Modulation of glycine/glutamate-induced currents (TEVC) after treatment with SK3D-matured (**d**) and SK5G-matured (**e**). Left, normalized TEVC traces (I_0, baseline; I, after IgG). Right, IgG-induced current changes (I/I_0; Extended Data Fig. 11a) at varying IgG concentrations. *P* values were calculated using two-sided one-sample *t*-tests, with the null hypothesis that the mean ratio is 1, with *n* = 5 biological replicates per concentration. **f**, Immunohistochemistry for the Flag tag in hippocampal sections. DG, dentate gyrus; ML, molecular layer; PL, pyramidal layer. Scale bars, 1 mm (top) and 400 μm (bottom). **g,h**, Energy expenditure as determined using indirect calorimetry (data are mean ± s.e.m., *n* = 5 (mGO53) and *n* = 4 (SK3D); unadjusted two-sided one-sample *t*-test) (**g**) and body weight correlation (analysis of covariance (ANCOVA) adjusted for body weight) (**h**) in SK3D- and mGO53-treated mice. **i,j**, Seizure recording (**i**) and quantification (**j**) during 10 min after PTZ injection (0.5 mg; dose optimized for minimal baseline seizures). *P* values were calculated using two-sided Fisher's exact tests. ****$P < 0.0001$.

---

performed low-resolution 3D classification to segregate receptors into 0-IgG-bound (46%), 1-IgG-bound (45%) or 2-IgG-bound (9%) classes (Extended Data Fig. 8e), which were then reconstructed at full resolution. On the basis of ATD model building and measurement of the ATD-1 α4′–α5 distance, only classes 4 (1-IgG-bound) and 7 (2-IgG-bound) adopted the pre-active2 conformation (Extended Data Fig. 8f). Notably, the IgG molecule in class 4 was bound to the rearranged ATD heteromer (ATD-1). Taken together, these findings would suggest that binding to ATD-1 (compare with ATD-2) is necessary but not sufficient for the pre-active2 conformational rearrangement and that binding of a second IgG molecule to the ATD-2 site may stabilize this state. In the presence of micromolar concentrations of SK3D-germline, only 21% of NMDARs adopted the pre-active2 conformation, demonstrating that affinity maturation correlates with receptor modulation.

To test whether IgG binding was agonist dependent, we performed single-particle cryo-EM analysis of SK5A-matured in a complex with GluN1–GluN2B, purified in the absence of agonists glycine and glutamate (SK5A-matured-apo; Extended Data Fig. 9a,b and Supplementary Fig. 7b). The structural analysis confirmed that the binding of SK5A-matured involves residues identical to those of the agonist-bound NMDAR–SK5A-matured complex (Extended Data Fig. 9c, compare with Fig. 4f), indicating that antibody binding is independent of functional and conformational state. This model resembled the glycine-bound gly/apo state (PDB: 9ARH)[43] with a closed GluN1 LBD and reduced L1′–L2 and α4′–α5 distances (Extended Data Fig. 9d,e). Consistent with this, we identified a glycine-binding pocket density (Extended Data Fig. 9f) that we attribute to retained glycine from expressing cells, which dissociates slowly from the closed GluN1 LBD clamshell[51], in comparison to glutamate. The gly/apo state has considerable physiological relevance as glycine or D-serine are constitutively present in synapses[52], while glutamate concentrations are tightly regulated outside of neurotransmission[26]. Taken together, these findings demonstrate that SK5A-matured binds to the prevalent gly/apo state, where it can stabilize the pre-active2 conformation on glutamate binding.

To characterize the conformational spectrum of NMDARs across our panel of antibody–NMDAR complexes (Fig. 4), we estimated α4′–α5 distances for each NMDAR-antibody complex in comparison to reference structures[43,46]. By leveraging the α4′–α5 distance as an objective read-out of the NMDAR ATD conformational state, we could classify NMDARs into four major conformations: gly/apo, pre-active, open, pre-active2 and non-active (Fig. 5c). In all complexes, NMDARs adopt a closed-channel state: key features required for channel gating—namely, outward tension in the GluN2B LBD–M3′ linker (measured by a GluN2B Gln662–Gln662 Cα distance exceeding 60 Å)[46,47]

and the interdomain rotation between the LBD and transmembrane domain (TMD)[43]—are absent, thereby stabilizing the closed channel pore (Extended Data Fig. 9g). To exclude the possibility of biases introduced by model fitting, α4′–α5 and L1′–L2 distances were verified by model alignment to local refinements of the ATDs and LBD (Extended Data Fig. 10a–f). While local density limitations in some structures introduced uncertainty in α4 helix positioning, the estimated distances provided sufficient resolution to distinguish between major conformational states. For SK5B and SK5G, only receptors with a non-active conformation could be identified, with no evidence of alternative conformations on 3D classification. For reference, in the presence of glycine and glutamate, around 80% of IgG-unbound GluN1–GluN2B receptors adopt the non-active conformation[46], and so SK5G and SK5B might shift the conformational equilibrium towards the non-active (inhibitory) state, as has been previously described for other antibodies[31,32].

On the basis of the conformational patterns identified above, we predicted that the binding of SK3D-matured or SK5A-matured would potentiate NMDAR channel activity, while the binding of SK5B-matured or SK5G-matured would be inhibitory or non-modulatory. We tested antibody effects by TEVC in cRNA-injected oocytes (Fig. 5a, middle). Incubations with SK3D-matured or SK5A-matured were associated with statistically significant, dose-dependent potentiation (defined per Extended Data Fig. 11a) of NMDAR currents (Fig. 5d and Extended Data Fig. 11b), exceeding 200% at 333 nM. SK5G-matured application caused dose-dependent channel inhibition (Fig. 5e), while SK5B-matured showed comparatively very weak potentiation of receptor currents—less than 20% at 333 nM (Extended Data Fig. 11c). Incubation with 333 nM of non-binding control IgG (mGO53) had no effect (Extended Data Fig. 11d).

Pharmacological modulators of NMDAR activity have been shown to have diverse effects in NMDAR-expressing tumour models[30,36]. To link these findings with our observations of antibody-associated tumour regression in the 4T1-NMDAR tumour model (Fig. 2), we hypothesized that NMDAR-potentiating antibodies would induce excitotoxic cell death in vitro, while NMDAR-inhibitory antibodies would be protective. SK3D and SK5G had opposing effects on viability (Extended Data Fig. 12a), with SK3D exhibiting dose-dependent cytotoxicity (half-maximum inhibitory concentration (IC_{50}) = 120 nM, 95% confidence interval (CI) = 109–131 nM; Extended Data Fig. 12b). To evaluate the in vivo relevance of the antibodies in the absence of a polyclonal response, we treated 4T1-NMDAR-tumour-bearing B-cell-deficient BALBc ($Ighj^{-/-}$) mice with DOX and either mGO53 or SK3D mIgG2a for 7 days. We verified antibody delivery by ELISA in end-point plasma samples, achieving levels equivalent to peak titres in wild-type mice

Article

(Extended Data Fig. 12c, compare with Fig. 2g). Consistent with the cytotoxicity observed in vitro, SK3D IgG treatment significantly augmented tumour regression after DOX induction (Extended Data Fig. 12d). While residual tumour tissue was detected in all mice, in 2 out of 4 SK3D-treated tumours, we observed a near-complete pathological response (pCR) with rare pan-CK-positive cells (Extended Data Fig. 12e). In SK3D-pCR tumours, epithelial-specific transcripts (including *Hmga2* and *Grin1-2b*) were minimally detected, while immune-related transcripts were significantly enriched compared with mGO53-treated tumours (Extended Data Fig. 12f). Taken together, these findings indicate that the anti-cancer effect of SK3D treatment is likely to reflect a combination of direct cytotoxicity and downstream immunological activation

Together, these results demonstrate that mouse tumour-derived anti-NMDAR antibodies can induce a full spectrum of functional modulation, ranging from strong inhibition (SK5G) to minimal effect (SK5B) to strong potentiation (SK3D, SK5A) of channel currents. Importantly, these functional effects can be accurately predicted from the α4′–α5 distance alone (Extended Data Fig. 11e, $r^2 = 0.98$, $P = 0.0059$), indicating the direct relevance of cryo-EM-enabled structural analysis in the study of autoantibody-mediated disease.

Antibody transfer recapitulates ANRE

If autoimmunity were a direct consequence of anti-tumour immunity, tumour-derived NMDAR-modulating antibodies should be sufficient to induce symptoms and signs of ANRE. We opted to use a passive-transfer system to uncouple the monoclonal antibody effect from the systemic effects of the tumour. Mice received intracerebroventricular antibody infusions through subcutaneous pumps in metabolic cages (Fig. 5a (right)). After 5 days of acclimatization with PBS infusion, mice received 40 μg per day of mGO53 or NMDAR-binding IgG (Flag-tagged mouse IgG2a) for 14 days. Anti-Flag staining in the hippocampus was used as a biomarker for on-target SK3D antibody delivery (Fig. 5f).

The most prevalent symptoms of ANRE are autonomic instability, primarily manifesting as hyperthermia, and epileptic seizures[4]. Epileptic seizures are caused by either activation of excitatory signalling or inhibition of inhibitory signalling[53]. In light of NMDARs' dominant role in excitatory signalling[54] and the role of NMDAR blockers in treating seizures[55], we hypothesized that current-potentiating antibodies, such as SK3D-matured, would be the most likely to recapitulate these two hallmarks of the clinical syndrome. Longitudinal energy expenditure monitoring by indirect calorimetry (5 mGO53, 4 SK3D) showed an increase in total energy expenditure in SK3D-treated mice from day 7, which was significant by day 10 (Fig. 5g), independent of body weight (Fig. 5h) or activity (Extended Data Fig. 13a). Mice generally gained weight during the study (Extended Data Fig. 13b, $P = 0.0087$, mixed-effects model), probably reflective of normal biology in mice receiving a standard laboratory diet, given that the rate of weight gain did not differ between groups ($P = 0.431$ for the interaction term in the mixed-effects model). Elevations in energy expenditure not explained by body weight, activity or environmental changes are most likely to reflect increased thermogenesis, which could precipitate hyperthermia; we observed hyperthermia after intraventricular SK3D administration, especially during the dark phase ($r^2 = 0.17$, $P = 9.58 \times 10^{-8}$; Extended Data Fig. 13c and Extended Data Fig. 13d). In an independent experiment, mice were infused with SK5G-matured ($n = 4$) or mGO53 ($n = 3$) to investigate the phenotypic consequences of current-inhibiting antibodies using metabolic cages. Mice treated with SK5G showed significantly increased locomotor activity (Extended Data Fig. 13e) and a trend toward higher energy expenditure, which correlated with their increased activity (Extended Data Fig. 13f,g). This locomotor phenotype was also observed when healthy female mice were given a single dose of the NMDAR channel blocker ketamine (Extended Data Fig. 13h) and is consistent with known effects of NMDAR channel inhibition[56].

To test whether SK3D antibody infusion would also recapitulate the reduced seizure threshold in vivo, 22 mice (11 mGO53, 11 SK3D) were given a single intraperitoneal dose of 20 mg per kg pentylenetetrazole (PTZ, a GABA receptor antagonist[57]) after 2 weeks of antibody infusion, as described above. This dose was deliberately chosen so as not to induce significant seizure activity in healthy female mice. We assessed four well-characterized seizure events in the 10 min after PTZ injection (Fig. 5i): tail dorsiflexion (Straub tail), myoclonic jerks, forelimb clonus and generalized tonic–clonic seizures. All four seizure events were significantly more prevalent and recurred more often in the SK3D-treated mice versus the mGO53-treated mice (Fig. 5i,j, $P < 0.05$, Fisher's exact test). All SK3D-treated mice exhibited evidence of seizure activity, often with multiple events recorded in a short period; in four mice, these events escalated to generalized seizures (Fig. 5i). In an independent experiment, we replicated significant seizure activity in SK3D-treated ($n = 3$) mice but observed no significant seizure activity in SK5G-treated ($n = 4$) or mGO53-treated ($n = 3$) mice (Extended Data Fig. 13i). Taken together, our results demonstrate that intracerebroventricular infusion of SK3D-matured, but not SK5G-matured, was sufficient to phenocopy the reduced seizure threshold and autonomic instability commonly observed in patients with ANRE. As SK3D is clonally related to a germline configuration B cell receptor that retains NMDAR binding (Fig. 3f), these findings directly connect germline-encoded antibodies with ANRE.

Anti-NMDAR antibodies in human TNBC

To determine the prevalence of anti-NMDAR humoral responses in TNBC, we analysed plasma from 53 female patients with TNBC (Fig. 6a; age range, 26–89 years). We found that 8 out of 53 (15%) patients had antibody titres above the 95% upper limit of normal (Fig. 6b). None of these antibody-high patients had disease progression over a median follow-up of 4.29 years (Fig. 6c). To link NMDAR expression with antibody titres, we detected epithelial GluN1–GluN2B expression using IF and flow cytometry in antibody-high tumours but not in no-antibody tumours (Fig. 6d,e). Flow cytometry revealed variable GluN1–GluN2B double-positive cell fractions across four patients with TNBC, with the highest fraction observed in an antibody-high tumour (patient N38; titre, 416 ng ml^{-1}) (Fig. 6f and Supplementary Fig. 10a–c). scRNA-seq analysis of 6,343 cells tumour cells from the same patient recapitulated the tumour microenvironment (Extended Data Fig. 14a,b). Within the T cell fraction, we observed cytotoxic CD8$^+$ cells and T follicular helper-like CD4$^+$ cells (*CXCL13$^+$IGFL2$^+$*), which have been previously associated with tertiary lymphoid structure formation and improved outcomes in TNBC. *GRIN1* and *GRIN2B* were most highly expressed in luminal–progenitor (*KIT$^+$KRT23$^+$*) and luminal–alveolar (*ELF5$^+$*) cancer cells[58], both lacking *ESR1* expression (Fig. 6g and Extended Data Fig. 14c,d). These findings reveal a strong correlation between tumour-intrinsic NMDAR expression and circulating anti-NMDAR antibodies, supporting a model in which anti-NMDAR immunity constrains TNBC tumour growth.

Discussion

Our results suggest that autoimmunity may be an unavoidable consequence of immune surveillance (Extended Data Fig. 15). We hypothesize that germline-encoded antibodies evolved to detect altered cellular states, including reactivation of developmental programs[59] seen in viral infections or cancer[60,61]. We detected NMDAR expression in human TNBC, as reported in other cancers[6,30,36], although precise prevalence remains to be established. The intratumoural recruitment of unmutated NMDAR-binding B cells indicates the adaptive immune system is not inherently tolerant to these NMDAR subunits. The absence of *GRIN1* and *GRIN2B* expression in the thymus, as has been suggested previously[62], is likely to explain the persistence of NMDAR-specific T helper cells,
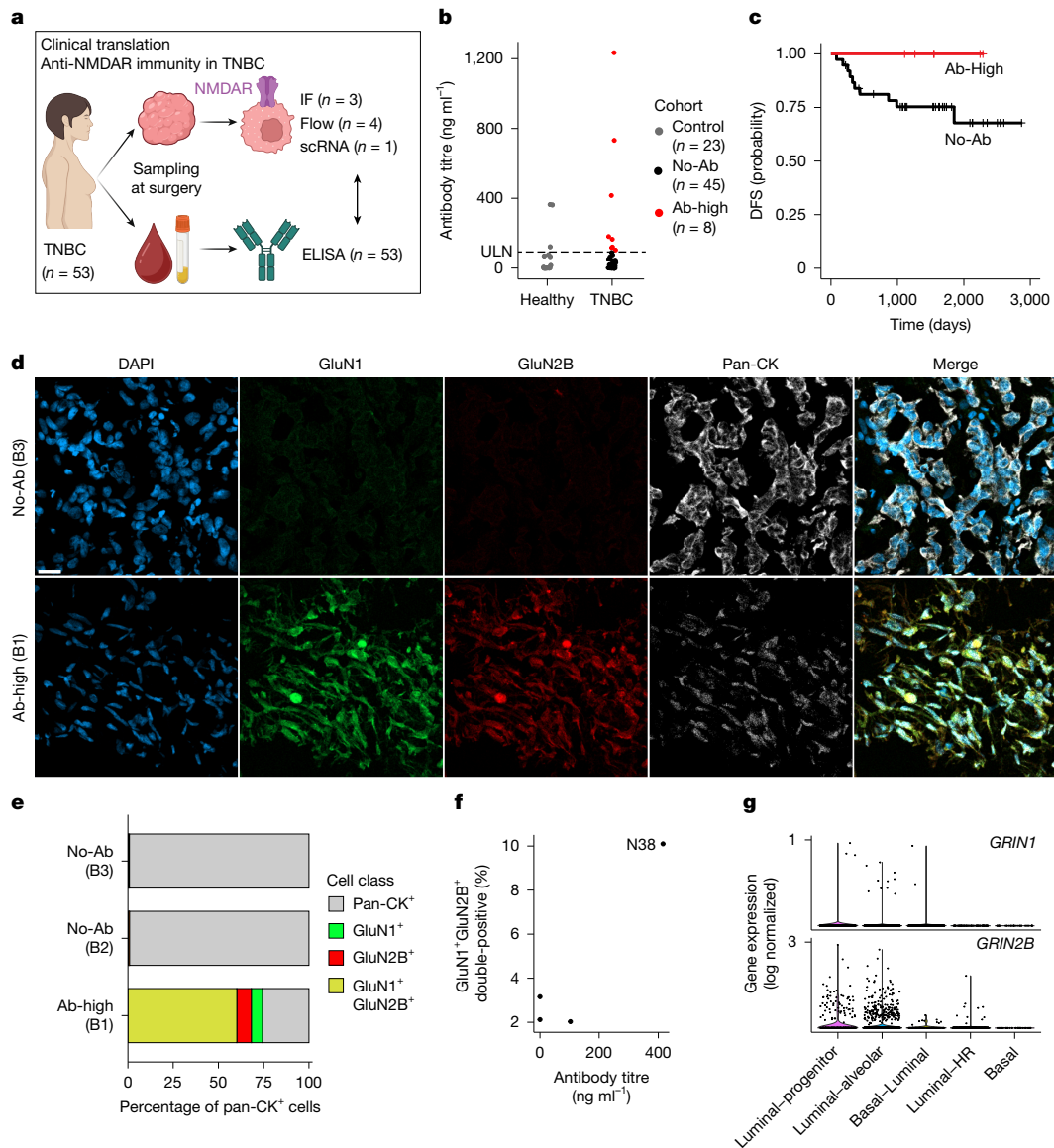
Fig. 6 | Patients with NMDAR-positive TNBC develop anti-NMDAR antibodies.
a, Schematic of the analysis workflow for patients with TNBC (*n* = 53). Blood samples were collected at surgery for ELISA-based antibody detection (*n* = 53), and tissue samples, where available, were analysed by IF using validated antibodies (*n* = 3), flow cytometry (*n* = 4) and scRNA-seq (*n* = 1). The diagram was created using BioRender; Janowitz, T. https://biorender.com/1hq8gbl (2026). **b**, Anti-NMDAR antibody (Ab) titres in the plasma from healthy control individuals (*n* = 23) and patients with TNBC (*n* = 53). On the basis of the results for the healthy control cohort, patients with TNBC were stratified into antibody-high (*n* = 8) and no-antibody (*n* = 45) groups, defined as having titres above or below the 95% upper limit of normal (ULN, 92 ng ml^{-1}, dashed line), respectively. Each result reflects the mean of at least two technical replicates with background subtraction. **c**, Disease-free survival (DFS) curves for antibody-high and no-antibody patients with available follow-up data. **d**, Representative IF

staining for GluN1 (using antibody 003-102), GluN2B (using antibody IgG2) and pan-CK in one antibody-high and one no-antibody TNBC tumour sample. High-power fields are representative of at least five separately imaged regions per slide. NMDAR staining validation data are provided in Supplementary Fig. 2. Scale bar, 20 μm. **e**, IF quantification of NMDAR subunit expression in pan-CK-positive epithelial cells in three individual patient samples (B1, B2 and B3), showing the proportion of cells expressing no NMDAR subunits (grey), GluN1 only (green), GluN2B only (red) or both subunits (GluN1$^+$GluN2B$^+$, yellow). **f**, Anti-NMDAR antibody titres and the percentage of GluN1$^+$GluN2B$^+$ double-positive non-immune (CD45$^-$) cells were measured using flow cytometry in tumour cell suspensions from four patients. **g**, Single-cell expression (scRNA-seq) of *GRIN1* and *GRIN2B* across epithelial cell populations from patient N38 tumour (cell type definitions are provided in Extended Data Fig. 14c,d).

which are required for class switching and affinity maturation. We further demonstrate that, in B-cell-deficient mice, SK3D was sufficient to drive tumour regression with concomitant immune activation, suggesting antibody binding licences broader immunological engagement.

The correlation between ANRE symptoms and cerebrospinal fluid, but not plasma, antibody titres[63] highlights the critical role of BBB breakdown in disease pathogenesis[64]. In our current study, we demonstrate that direct ventricular infusion of NMDAR-potentiating antibodies induced ANRE symptoms in vivo, while inhibitory antibodies

did not, underscoring functional heterogeneity. These distinctions may explain clinical heterogeneity of the condition and therapeutic strategies that retain antitumour efficacy while mitigating neurotoxicity. We acknowledge that this is a reductionist approach, considering that the clinical observations support a two-stage process leading to ANRE, requiring both immunogenic ectopic expression of NMDAR followed by BBB disruption. Concordantly, individuals with plasma anti-NMDAR antibodies are much more common than patients with ANRE[65], and we did not observe clinical encephalitis in the subset of

Article

TNBC patients with elevated antibody titres. Moreover, tumour-specific ANRE associations[5] may reflect the capacity for BBB disruption[66] or NMDAR expression levels[36].

The allosteric NMDAR modulation that we focus on in this Article could work in tandem with other mechanisms by which anti-NMDAR antibodies are known to alter receptor abundance[67], such as nanoscale receptor reorganization[68], antibody-mediated receptor internalization[31,42] and the recruitment of downstream immune effector cells[69]. The detection of circulating anti-NMDAR antibodies in patients with TNBC with favourable outcomes supports a paradigm in which anti-tumour immunity and autoimmunity share immunological origins. As the understanding of paraneoplastic neurological diseases such as ANRE advances, unitary disorders may be refined as spectrum disorders that reflect polyclonal antibody responses, in which monoclonal antibodies can exhibit both activating and inhibitory effects. Physicians and patients have highlighted the need to develop targeted approaches for the classification and treatment of neuropsychiatric disease[70]. Perhaps our results can contribute to a mechanistic framework to guide both diagnosis and mechanistic therapy for these conditions.

Online content

Any methods, additional references, Nature Portfolio reporting summaries, source data, extended data, supplementary information, acknowledgements, peer review information; details of author contributions and competing interests; and statements of data and code availability are available at https://doi.org/10.1038/s41586-026-10278-0.

1. Good, R. A. Relations between immunity and malignancy. *Proc. Natl Acad. Sci. USA* **69**, 1026–1032 (1972).
2. Kohanim, Y. K., Tendler, A., Mayo, A., Friedman, N. & Alon, U. Endocrine autoimmune disease as a fragility of immune surveillance against hypersecreting mutants. *Immunity* **52**, 872–884 (2020).
3. Dalmau, J. & Graus, F. Antibody-mediated encephalitis. *N. Engl. J. Med.* **378**, 840–851 (2018).
4. Dalmau, J. et al. Paraneoplastic anti-*N*-methyl-D-aspartate receptor encephalitis associated with ovarian teratoma. *Ann. Neurol.* **61**, 25–36 (2007).
5. Dalmau, J. et al. Anti-NMDA-receptor encephalitis: case series and analysis of the effects of antibodies. *Lancet Neurol.* **7**, 1091–1098 (2008).
6. Zeng, Q. et al. Synaptic proximity enables NMDAR signalling to promote brain metastasis. *Nature* **573**, 526–531 (2019).
7. Medzhitov, R. & Janeway, C. A. Jr. How does the immune system distinguish self from nonself? *Semin. Immunol.* **12**, 185–188 (2000).
8. Mackay, I. R., Rosen, F. S., Davidson, A. & Diamond, B. Autoimmune diseases. *N. Engl. J. Med.* **345**, 340–350 (2001).
9. Darnell, R. B. & Posner, J. B. Paraneoplastic syndromes involving the nervous system. *N. Engl. J. Med.* **349**, 1543–1554 (2003).
10. Medawar, P. B. Immunity to homologous grafted skin; the fate of skin homografts transplanted to the brain, to subcutaneous tissue, and to the anterior chamber of the eye. *Br. J. Exp. Pathol.* **29**, 58–69 (1948).
11. Darnell, R. B. Onconeural antigens and the paraneoplastic neurologic disorders: at the intersection of cancer, immunity, and the brain. *Proc. Natl Acad. Sci. USA* **93**, 4529–4536 (1996).
12. Avrameas, S. Natural autoantibodies: from 'horror autotoxicus' to 'gnothi seauton'. *Immunol. Today* **12**, 154–159 (1991).
13. Fichtner, M. L. et al. Affinity maturation is required for pathogenic monovalent IgG4 autoantibody development in myasthenia gravis. *J. Exp. Med.* **217**, e20200513 (2020).
14. Wenke, N. K. et al. *N*-methyl-D-aspartate receptor dysfunction by unmutated human antibodies against the NR1 subunit. *Ann. Neurol.* **85**, 771–776 (2019).
15. Kreye, J. et al. Human cerebrospinal fluid monoclonal *N*-methyl-D-aspartate receptor autoantibodies are sufficient for encephalitis pathogenicity. *Brain* **139**, 2641–2652 (2016).
16. Graus, F. et al. Anti-Hu antibodies in patients with small-cell lung cancer: association with complete response to therapy and improved survival. *J. Clin. Oncol.* **15**, 2866–2872 (1997).
17. Darnell, R. B. & DeAngelis, L. M. Regression of small-cell lung carcinoma in patients with paraneoplastic neuronal antibodies. *Lancet* **341**, 21–22 (1993).
18. Cabrita, R. et al. Tertiary lymphoid structures improve immunotherapy and survival in melanoma. *Nature* **577**, 561–565 (2020).
19. Velasco, R. et al. Encephalitis induced by immune checkpoint inhibitors. *JAMA Neurol.* **78**, 864–873 (2021).
20. Maher, V. E. et al. Analysis of the association between adverse events and outcome in patients receiving a programmed death protein 1 or programmed death ligand 1 antibody. *J. Clin. Oncol.* **37**, 2730–2737 (2019).
21. Schumacher, T. N. & Thommen, D. S. Tertiary lymphoid structures in cancer. *Science* **375**, eabf9419 (2022).
22. Makuch, M. et al. N-methyl-D-aspartate receptor antibody production from germinal center reactions: Therapeutic implications. *Ann. Neurol.* **83**, 553–561 (2018).
23. Li, L. Y., Keles, A., Homeyer, M. A. & Prüss, H. Antibodies in neurological diseases: established, emerging, explorative. *Immunol. Rev.* https://doi.org/10.1111/imr.13405 (2024).
24. Paoletti, P., Bellone, C. & Zhou, Q. NMDA receptor subunit diversity: impact on receptor properties, synaptic plasticity and disease. *Nat. Rev. Neurosci.* **14**, 383–400 (2013).
25. Furukawa, H., Singh, S. K., Mancusso, R. & Gouaux, E. Subunit arrangement and function in NMDA receptors. *Nature* **438**, 185–192 (2005).
26. Hansen, K. B. et al. Structure, function, and allosteric modulation of NMDA receptors. *J. Gen. Physiol.* **150**, 1081–1105 (2018).
27. Martinez-Hernandez, E. et al. Analysis of complement and plasma cells in the brain of patients with anti-NMDA receptor encephalitis. *Neurology* **77**, 589–593 (2011).
28. Gegenhuber, B., Wu, M. V., Bronstein, R. & Tollkuhn, J. Gene regulation by gonadal hormone receptors underlies brain sex differences. *Nature* **606**, 153–159 (2022).
29. Hogan-Cann, A. D., Lu, P. & Anderson, C. M. Endothelial NMDA receptors mediate activity-dependent brain hemodynamic responses in mice. *Proc. Natl Acad. Sci. USA* **116**, 10229–10231 (2019).
30. Li, L. et al. GKAP acts as a genetic modulator of NMDAR signaling to govern invasive tumor growth. *Cancer Cell* **33**, 736–751 (2018).
31. Michalski, K. et al. Structural and functional mechanisms of anti-NMDAR autoimmune encephalitis. *Nat. Struct. Mol. Biol.* **31**, 1975–1986 (2024).
32. Tajima, N. et al. Development and characterization of functional antibodies targeting NMDA receptors. *Nat. Commun.* **13**, 923 (2022).
33. Yayon, N. et al. A spatial human thymus cell atlas mapped to a continuous tissue axis. *Nature* **635**, 708–718 (2024).
34. Michelson, D. A., Hase, K., Kaisho, T., Benoist, C. & Mathis, D. Thymic epithelial cells co-opt lineage-defining transcription factors to eliminate autoreactive T cells. *Cell* **185**, 2542–2558 (2022).
35. Schrörs, B. et al. Multi-omics characterization of the 4T1 murine mammary gland tumor model. *Front. Oncol.* **10**, 1195 (2020).
36. Li, L. & Hanahan, D. Hijacking the neuronal NMDAR signaling circuit to promote tumor growth and invasion. *Cell* **153**, 86–100 (2013).
37. Nabeyama, A. et al. xCT deficiency accelerates chemically induced tumorigenesis. *Proc. Natl Acad. Sci. USA* **107**, 6436–6441 (2010).
38. Graf, R. et al. BCR-dependent lineage plasticity in mature B cells. *Science* **363**, 748–753 (2019).
39. Kreslavsky, T. et al. Essential role for the transcription factor Bhlhe41 in regulating the development, self-renewal and BCR repertoire of B-1a cells. *Nat. Immunol.* **18**, 442–455 (2017).
40. Wardemann, H. et al. Predominant autoantibody production by early human B cell precursors. *Science* **301**, 1374–1377 (2003).
41. Krasik, S. V. et al. Systematic evaluation of intratumoral and peripheral BCR repertoires in three cancers. *eLife* **13**, RP89506 (2025).
42. Wang, H. et al. Structural basis for antibody-mediated NMDA receptor clustering and endocytosis in autoimmune encephalitis. *Nat. Struct. Mol. Biol.* https://doi.org/10.1038/s41594-024-01387-3 (2024).
43. Chou, T.-H. et al. Molecular mechanism of ligand gating and opening of NMDA receptor. *Nature* **632**, 209–217 (2024).
44. Vanderlugt, C. L. & Miller, S. D. Epitope spreading in immune-mediated diseases: implications for immunotherapy. *Nat. Rev. Immunol.* **2**, 85–95 (2002).
45. Reincke, S. M. et al. Chimeric autoantibody receptor T cells deplete NMDA receptor-specific B cells. *Cell* **186**, 5084–5097 (2023).
46. Chou, T.-H., Tajima, N., Romero-Hernandez, A. & Furukawa, H. Structural basis of functional transitions in mammalian NMDA receptors. *Cell* **182**, 357–371 (2020).
47. Tajima, N. et al. Activation of NMDA receptors and the mechanism of inhibition by ifenprodil. *Nature* **534**, 63–68 (2016).
48. Karakas, E. & Furukawa, H. Crystal structure of a heterotetrameric NMDA receptor ion channel. *Science* **344**, 992–997 (2014).
49. Lee, C. H. et al. NMDA receptor structures reveal subunit arrangement and pore architecture. *Nature* **511**, 191–197 (2014).
50. Karakas, E., Simorowski, N. & Furukawa, H. Subunit arrangement and phenylethanolamine binding in GluN1/GluN2B NMDA receptors. *Nature* **475**, 249–253 (2011).
51. Furukawa, H. & Gouaux, E. Mechanisms of activation, inhibition and specificity: crystal structures of the NMDA receptor NR1 ligand-binding core. *EMBO J.* **22**, 2873–2885 (2003).
52. Berger, A. J., Dieudonné, S. & Ascher, P. Glycine uptake governs glycine site occupancy at NMDA receptors of excitatory synapses. *J. Neurophysiol.* **80**, 3336–3340 (1998).
53. Staley, K. Molecular mechanisms of epilepsy. *Nat. Neurosci.* **18**, 367–372 (2015)
54. Cotman, C. W. & Iversen, L. L. Excitatory amino acids in the brain—focus on NMDA receptors. *Trends Neurosci.* **10**, 263–265 (1987).
55. Fang, Y. & Wang, X. Ketamine for the treatment of refractory status epilepticus. *Seizure* **30**, 14–20 (2015).
56. Liljequist, S., Ossowska, K., Grabowska-Andén, M. & Andén, N.-E. Effect of the NMDA receptor antagonist, MK-801, on locomotor activity and on the metabolism of dopamine in various brain areas of mice. *Eur. J. Pharmacol.* **195**, 55–61 (1991).
57. Squires, R. F., Saederup, E., Crawley, J. N., Skolnick, P. & Paul, S. M. Convulsant potencies of tetrazoles are highly correlated with actions on GABA/benzodiazepine/picrotoxin receptor complexes in brain. *Life Sci.* **35**, 1439–1444 (1984).
58. Kumar, T. et al. A spatially resolved single-cell genomic atlas of the adult human breast. *Nature* **620**, 181–191 (2023).
59. Ben-Porath, I. et al. An embryonic stem cell-like gene expression signature in poorly differentiated aggressive human tumors. *Nat. Genet.* **40**, 499–507 (2008).
60. Elkon, K. & Casali, P. Nature and functions of autoantibodies. *Nat. Clin. Pract. Rheumatol.* **4**, 491–498 (2008).
61. DeSena, A., Graves, D., Warnack, W. & Greenberg, B. M. Herpes simplex encephalitis as a potential cause of anti-*N*-methyl-D-aspartate receptor antibody encephalitis: report of 2 cases. *JAMA Neurol.* **71**, 344–346 (2014).
62. Handel, A. E., Irani, S. R. & Holländer, G. A. The role of thymic tolerance in CNS autoimmune disease. *Nat. Rev. Neurol.* **14**, 723–734 (2018).

63. Gresa-Arribas, N. et al. Antibody titres at diagnosis and during follow-up of anti-NMDA receptor encephalitis: a retrospective study. *Lancet Neurol.* **13**, 167–177 (2014).

64. Ji, S.-H. et al. Dynamic contrast-enhanced mri quantification of altered vascular permeability in autoimmune encephalitis. *Radiology* **310**, e230701 (2024).

65. Steiner, J. et al. Prevalence of *N*-methyl-D-aspartate receptor autoantibodies in the peripheral blood: healthy control samples revisited. *JAMA Psychiatry* **71**, 838–839 (2014).

66. Arvanitis, C. D., Ferraro, G. B. & Jain, R. K. The blood–brain barrier and blood–tumour barrier in brain tumours and metastases. *Nat. Rev. Cancer* **20**, 26–41 (2020).

67. Prüss, H. Autoantibodies in neurological disease. *Nat. Rev. Immunol.* **21**, 798–813 (2021).

68. Jézéquel, J. et al. Dynamic disorganization of synaptic NMDA receptors triggered by autoantibodies from psychotic patients. *Nat. Commun.* **8**, 1791 (2017).

69. Rahman, K. A. et al. Microglia actively remove NR1 autoantibody-bound NMDA receptors and associated post-synaptic proteins in neuron microglia co-cultures. *Glia* **71**, 1804–1829 (2023).

70. Scangos, K. W., State, M. W., Miller, A. H., Baker, J. T. & Williams, L. M. New and emerging approaches to treat psychiatric disorders. *Nat. Med.* **29**, 317–333 (2023).

Article

Methods

Sex as a biological variable

In consideration of the clinical context, in which TNBC[71], ANRE[72,73] and their co-occurrence[73,74] are predominantly observed in female patients, we have proactively chosen to model the underlying biology in female mice to maximize translational relevance. Furthermore, there are considerable differences in symptom frequency and severity between male and female patients with ANRE[75,76]. This sexual dimorphism may be partly explained by sex hormone activity, as ER signalling directly modulates NMDAR expression[28,77] in the brain.

Ethical oversight

Human-participant oversight was provided by the Northwell Health Institutional Review Board (IRB 20-0150) for the prospective TNBC cohort and the South Central-Oxford A Research Ethics Committee (REC16/YH/0013) for the ANRE study. Vendor-procured specimens received IRB approvals from their respective institutions, as was verified by each vendor. The authors affirm that all human research was performed in accordance with the relevant guidelines and regulations, and that informed consent was obtained. Human samples included in this study are summarized in Supplementary Table 6.

Animals

All animal experiments were performed in strict accordance with the Cold Spring Harbor Laboratory (CSHL) Institutional Animal Care and Use Committee (IACUC) and the National Institutes of Health Guide for the Care and Use of Laboratory Animals. Mice were kept in specific-pathogen-free conditions under a 24 h 12 h–12 h light–dark cycle. Food and water were provided ad libitum, and the temperature and humidity were maintained at 21–23 °C and 40–60% relative humidity. Mice were allowed to acclimatize for at least 1 week after their arrival to the Cold Spring Harbor Laboratory animal facility. Adult female mice between 9 and 14 weeks of age were used. All mice were randomly assigned to experimental groups, and the sample size was predetermined according to the type of experiment, on the basis of common practice. For the majority of experiments, the investigators were not blinded to group allocation as they performed both the experiment and analysis, making blinding not possible. For tumour experiments, 8-week-old female wild-type BALB/c mice were obtained from Jackson Laboratory. As per our IACUC-approved protocol, a tumour size of greater than 20 mm was defined as a humane end point and this limit was never exceeded in any of the experiments. For antibody infusion experiments, 8-week-old female wild-type C57BL/6 mice were obtained from Jackson Laboratory. Outbred wild-type adult female *X. laevis* frogs (aged 2–4 years) were ordered from Xenopus 1.

Patient samples

Tumour and matched plasma specimens were obtained from three cohorts of individuals with stage I–III TNBC who received surgical resection as part of standard clinical management. All studies were approved by Institutional Review Boards, and written informed consent was obtained from all of the participants. All specimens were fully de-identified before analysis. The Northwell Health cohort ($n = 48$) was established through an academic partnership under IRB protocol 20-0150. Peripheral blood samples were collected either before or after surgery on the day of surgical resection. Tumour tissue was available for a subset of patients, depending on the availability of excess clinical material. Tumour specimens were viably preserved by mincing fresh tissue and storing in cryopreservation medium at −80 °C. The vendor-supplied cohort ($n = 5$) comprised paired plasma and tumour specimens obtained from Biochain Institute under IRB-approved protocols with the participants' informed consent. Tumour sections were preserved as cold acetone-fixed frozen tissue and stored at −80 °C. A third cohort consisted of a single frozen tumour section obtained from Origene (patient ID: FR001D525), collected under IRB-approved protocols with the participant's informed consent. This sample was used for Visium HD spatial transcriptomic profiling. TNBC status was confirmed in all cases by immunohistochemistry according to standard clinical criteria: ER and progesterone receptor (PR) expression each <1% of tumour nuclei, and HER2 scored as 0–1+ by immunohistochemistry or 2+ with negative fluorescence in situ hybridization. Plasma samples from all cohorts were processed using standardized protocols and stored at −80 °C until analysis. For the Northwell cohort, DFS data were abstracted by manual review of electronic health records by the Northwell biorepository team. DFS was defined as the interval from surgery to first recurrence or death, with censoring at the most recent clinical follow-up. To assess the normal range of anti-NMDAR antibody titres, a panel of plasma samples from healthy women 18–30 years of age ($n = 23$) was obtained from BioIVT under IRB-approved protocols with the participants' informed consent. All of the patient samples in this study served as a discovery set, and no formal power calculation was performed.

B cell isolation and antibody cloning

The OX1 antibody was isolated from one patient with a confirmed diagnosis of anti-NMDAR encephalitis (ANRE), on the basis of cerebrospinal fluid antibody testing, with written informed consent as part of a research study approved by the University of Oxford with ethical approval REC16/YH/0013. Peripheral blood mononuclear cells (PBMCs) were isolated from patient blood samples and, after thawing, PBMCs were labelled using fluorophore-conjugated biotinylated GluN1-ATD baits along with B cell surface marker antibodies (CD19, CD20, IgG) for 30 min at 4 °C. GluN1-ATD-binding B cells were enriched by fluorescence-activated cell sorting and sorted into 96-well plates containing single-cell culture medium. After 10–14 days of culture, the cell culture supernatant was prescreened for NMDAR reactivity using GluN1-transfected HEK293 cells by IF microscopy. Positive wells were identified, and antibody sequences were determined using the RNA extraction using the RNeasy kit (Qiagen), followed by reverse transcription and amplification of heavy- and light-chain immunoglobulin variable regions using primers specific for human IgG, followed by Sanger sequencing.

Cell culture

Sf9 insect cells (Thermo Fisher Scientific, 11496015) were maintained in a non-humidified shaker (125 rpm) at 27 °C in CCM3 medium (Cytiva). HEK293S GnTI- cells (American Type Culture Collection, CRL-3022) were maintained in a humidified shaker (115 rpm) at 37 °C and 8% CO_2 in FreeStyle 293 expression medium (Thermo Fisher Scientific) supplemented with 2% FBS. 4T1-NMDAR cells were maintained in a humidified incubator at 37 °C and 5% CO_2 in RPMI 1640 media with L-glutamine, supplemented with 10% tetracycline-free FBS (Takara Bio) and 100 U ml^{-1} penicillin–streptomycin. All of the cell lines were routinely tested for *Mycoplasma* contamination with consistently negative results.

Purification of NMDARs

Human GluN1a–GluN2B NMDA receptor (NMDAR) proteins were expressed in Sf9 cells as described previously[78]. In brief, Sf9 cells were grown to a density of 6×10^6 cells per ml before infection with 30 ml per 1 l cells of freshly collected P1 virus. Cells were collected 48 h after infection by centrifugation at 3,000g for 20 min at 4 °C and frozen as cell pellets. Cells were thawed and resuspended in HEPES-buffered saline (HBS) with glycine/glutamate (HBSG) buffer (20 mM HEPES, 150 mM NaCl, pH 7.5, 1 mM glycine and 1 mM glutamate) in the presence of 1 mM phenylmethylsulfonyl fluoride (PMSF) and lysed by two passes through an Avestin cell disruptor operating at 10,000 psi. Membrane fraction was collected by ultracentrifugation at 185,511g for 30 min at 4 °C in the Ti-45 rotor (Beckman Coulter). The pelleted membrane was solubilized in HBSG with 0.5% lauryl maltose neopentyl glycol (LMNG)

at a ratio of 10 ml buffer per 1 g of membrane, with gentle stirring for 30 min. The insoluble fraction was removed by ultracentrifugation and the supernatant was passed through a 5 ml Strep-Tactin Sepharose column (IBA Lifesciences) by gravity flow. The column was washed sequentially with wash buffer 1 (HBSG with 0.002% LMNG), wash buffer 2 (HBSG with 3 mM Mg-ATP), and then wash buffer 1. NMDAR protein was eluted using wash buffer with 3 mM desthiobiotin. For the SK5A-matured-apo structural analysis, NMDAR was initially purified using HBS buffer in the absence of glycine and glutamate. Eluted proteins were concentrated to 500 µl and separated by size-exclusion chromatography using the Superose 6 10/300 column (Cytiva) in a HBSG with 0.002% LMNG running buffer. To generate biotinylated NMDAR, Sf9 cells were infected with a baculovirus construct engineered with an AviTag at the C terminus of GluN1. Biotinylation was performed by incubating concentrated NMDAR protein overnight with 10 mM $MgCl_2$, 4 mM ATP, 0.3 mM D-biotin and 10 µM His-tagged BirA. BirA was removed by passing the reaction mixture over a Co-NTA column, and biotinylated NMDAR proteins were dialysed against HBSG with 0.002% LMNG to remove excess biotin.

Purification of IgG and Fab

Recombinant IgG and Fab proteins were expressed using the BacMam expression system, using a plasmid comprising codon-optimized heavy- and light-chain sequences assembled with a P2A sequence under the control of the cytomegalovirus promoter (Fig. 3a). The amino acid sequence for 003-102 (ref. 15) IgG was obtained from the ABCD database[79] (identifier ABCD_AU745), while the sequence for mGO53 (ref. 40) was provided by H. Wardemann. GnTI- cells were grown to a density of $2-3 \times 10^6$ cells per ml before infection with 40 ml per 1 l cells of freshly collected P1 virus. Sodium butyrate was added to a final concentration of 5 mM at the time of infection. After 4–5 days, the cell supernatant was collected by centrifugation at 3,000 g for 10 min and dialysed against 200 mM NaCl and 20 mM boric acid, pH 9.0 (for IgG) or 200 mM NaCl and 20 mM Tris, pH 8 (TBS) with 20 mM imidazole (for Fab). IgG2 protein[32] was purified from hybridoma supernatant. For IgG purification, the dialysed supernatant was passed through a rProtein A column (Cytiva, 17549801; or Genscript, L00464), washed with 1 M NaCl, 50 mM boric acid, pH 9.0, 1 M NaCl and 50 mM Tris, pH 8.0, and eluted with 200 mM NaCl and 50 mM citric acid, pH 3.0. The elution fractions were immediately neutralized with 1 M Tris. For Fab purification, the dialysed supernatant was passed through a metal chelating Sepharose column (Cytiva) charged with cobalt, washed with TBS containing 20 mM imidazole, TBS containing 40 mM imidazole and eluted with TBS containing 250 mM imidazole For structural studies, eluted proteins were dialysed into HBSG with 0.002% LMNG. For mouse phenotyping studies, eluted proteins were dialysed into an excess of PBS (137 mM NaCl, 2.7 mM KCl, 8 mM Na_2HPO_4 and 2 mM KH_2PO_4, pH 7.4) and were sterile filtered using a 0.22 µm filter under aseptic conditions. For structural characterization, IgG and Fab proteins were expressed with human constant domains. For mouse phenotyping studies, SK3D and mGO53 (non-binding control) were expressed as mouse IgG2a with a C-terminal Flag tag to verify delivery. IgG2a was selected, as it is the murine equivalent of IgG1 (ref. 80), which predominates in human ANRE[15].

ELISA analysis

EvenCoat Streptavidin Coated Plates (R&D Systems, CP004) were incubated overnight at 4 °C with 1.5 µg ml⁻¹ biotinylated GluN1–GluN2B NMDAR protein diluted in wash buffer (HBSG with 0.002% LMNG). NMDAR-immobilized wells were blocked with incubation buffer (wash buffer supplemented with 1% BSA). Monoclonal antibodies (human or mouse Fc) and mouse plasma samples were added to wells in duplicate to a final volume of 50 µl. A standard curve was constructed using 003-102 (ref. 15) engineered with either a mouse (IgG2a) or human (IgG1) Fc at a maximum concentration of 450 ng ml⁻¹. After multiple

washes with wash buffer, NMDAR-specific IgG binding was detected using horseradish peroxidase (HRP)-conjugated anti-human (Thermo Fisher Scientific, 31413, 1:8,000 dilution) and anti-mouse (Thermo Fisher Scientific, 62-6520, 1:4,000 dilution) IgG. Monoclonal antibodies, plasma samples (1:20), and secondary antibodies were all diluted in incubation buffer to reduce non-specific signals. To visualize the signal, 100 µl of TMB buffer (R&D Systems, DY999B) was added for 20 min, after which time the reaction was stopped with 50 µl of stop solution (R&D Systems, DY994). Absorbance at 450 nm (relative to 540 nm) was detected using the BioTek Synergy Neo2 Reader (Agilent Technologies). Interpolated concentrations relative to the 003-102 standard curve (Fig. 2f) were determined using the GainData ELISA Calculator (Arigo Biolaboratories).

To assess antibody polyreactivity, Maxisorp plates (Thermo Fisher Scientific, 439454) were coated with dsDNA (10 µg ml⁻¹), LPS (10 µg ml⁻¹) or insulin (5 µg ml⁻¹) in PBS pH 7.4, blocked with 1% BSA in PBS-Tween (0.05%), and developed using protein G-HRP with antibodies diluted in blocking buffer using established protocols[81]. To test for BSA cross-reactivity, Maxisorp plates were coated with BSA (10 µg ml⁻¹) in PBS pH 7.4, washed with HBSG containing 0.01% LMNG and blocked with 3% non-fat dry milk in the same buffer. Antibodies were diluted in incubation buffer containing 0.5% non-fat dry milk, and detection was performed using cross-adsorbed secondary antibodies.

For the analysis of human patient samples, we modified our indirect anti-NMDAR ELISA to mitigate against the potential for assay interference from non-specific antibody binding. In brief, for each sample, we subtracted the background optical density (OD) value for wells without immobilized NMDAR[82], the wash buffer was modified to contain 0.01% LMNG, the blocking buffer was modified to contain 2% BSA and the sample dilution buffer was modified to contain 10 µg ml⁻¹ polyclonal goat IgG (Southern Biotech, 0109-01). Finally, detection was performed using (Fab)2 goat anti-human HRP (Jackson Immunoresearch, 109-036-098, 1:12,000 dilution) to mitigate against heterophile antibody binding.

SPR analysis

Biotinylated NMDAR proteins diluted in HBSG with 0.002% LMNG at a concentration of 10 µg ml⁻¹ were immobilized onto streptavidin-coated sensor chips (Cytiva, BR100398/X100 or 29104992/T200) for 180 s at a flow rate of 5 µl min⁻¹. The running buffer was HBSG with 0.002% LMNG, with a flow rate of 30 µl min⁻¹. IgG proteins were dialysed against an excess of running buffer and then serially twofold diluted to generate five diluted samples per assay. For each antibody, the appropriate concentration range was estimated from ELISA data. IgG samples were injected sequentially from lowest to highest concentration for 400 seconds at a flow rate of 10 µl min⁻¹ according to the Biacore single-cycle kinetics protocol. The final dissociation period was 2,400 s. For all antibodies except for SK3D-matured and OX1-matured, data were collected using the Biacore T200 system; SK3D-matured and OX1-matured data were collected using the Biacore X100 system. A new sensor chip was used for each IgG to avoid interference from residual bound IgG. The experimental data were analysed by fitting a kinetic binding model in the anabel[83] R package using the default parameters (no decay or drift).

Single-particle cryo-EM

For all antibodies except for SK5B-germline, purified and concentrated NMDAR and antibody proteins were combined at a 4:1 molar ratio, with target final concentrations of 4 mg ml⁻¹ and 5.5 mg ml⁻¹, respectively, and incubated on ice for 30 min. For structural characterization of SK5B-germline, SK5B-germline IgG was combined with NMDAR (purified in the absence of glycine) at a 1:1 molar ratio, with a final NMDAR concentration of 0.2 mg ml⁻¹ and incubated on ice for 30 min. Amine-to-amine cross-linking was achieved during a 2 h incubation with 2 mM BS3 (Thermo Fisher Scientific, 21580), followed by reaction quenching with 20 mM Tris. The reaction mixture was concentrated

Article

20-fold to achieve a target final NMDAR concentration of 4 mg ml^{-1}. Before blotting, glyco-diosgenin was added to IgG-NMDAR mixtures at a final concentration of 0.1%. Glow discharging was performed using the PELCO easiGlow glow discharge cleaning system (Ted Pella) for 35 s under 15 mA. The grids were blotted with 3.5 µl of sample and plunge-frozen into liquid ethane using the FEI Vitrobot Mark IV system (Thermo Fisher Scientific) at 20 °C with 80% humidity, with a blot time of 4.5 s and under level 7 blot force. Holey carbon grids (Quantifoil R 2/1, R1.2/1.3 and R 0.6/1) and holey gold grids (UltrAuFoil R1.2/1.3) were used for blotting. Data were collected as described previously[31,43]. In brief, micrographs were acquired on the Titan Krios system operating at 300 keV using the Gatan K3 Summit direct electron detector coupled with the Gatan Imaging Filter quantum energy filter with a magnification of ×105,000 (0.827–861 Å px^{-1}). EPU software (Thermo Fisher Scientific) was used for image acquisition, with a defocus range of −0.8 to −2.2 µm, an exposure time of 2–4 s and a total dose ranging from 49 to 71.7 e^{-} Å^{-1} over 30 frames. Single-particle cryo-EM data processing was performed using WARP[84], Relion[85] and cryoSPARC[86] (v.3.2.0 to v.4.6.0). The precise data-processing steps for each dataset ($n = 9$) are summarized in Supplementary Figs. 6–8 and Supplementary Note 1. Models for GluN1 and GluN2B were built from Protein Data Bank (PDB) entry 7saa (ref. 87). Models for antibody Fab domains were built using homologous PDB entries[88] or ModelAngelo[89] where map resolution was sufficient. Antibody constant domains were not modelled as they could not be consistently visualized. Masked local refinements of the ATD heteromer–antibody interface were used to model the interaction interface. Models were built using UCSF ChimeraX[90] and WinCoot[91], with real-space refinement performed in PHENIX[92] (non-bonded weight set to 500). Models built from locally refined maps were used to characterize residue-level paratope-epitope interactions in antibody-NMDAR complexes. A summary of data collection and refinement statistics is shown in Supplementary Tables 4 and 5.

TEVC

Antibody-dependent receptor modulation was tested by TEVC using *X. laevis* oocytes. *Xenopus* oocytes were collected from the frogs raised in the animal facilities of Cold Spring Harbor Laboratory and defolliculated before use. Complementary RNAs (cRNAs) for the GluN1 and GluN2B subunits were injected into defolliculated oocytes. Subsequently, the oocytes were incubated in recovery medium (50% L-15 medium (Hyclone) buffered by 15 mM Na-HEPES at a final pH of 7.4) supplemented with 100 µg ml^{-1} streptomycin and 100 U ml^{-1} penicillin at 18 °C for 24–48 h. The TEVC recording was performed at room temperature in TEVC buffer (5 mM HEPES, 100 mM NaCl, 0.3 mM BaCl$_2$, 10 mM Tricine, at a final pH of 7.4). The agonist solutions were freshly prepared on the day of measurement from 1 M stock solutions of glycine and glutamate, and final concentrations of 100 µM for each of the agonists were obtained. The antibody solutions were dialysed against excess agonist-containing TEVC buffer before serial dilutions. For each antibody, a total of five serial dilutions was obtained by threefold dilutions of the 333 nM solution, with each antibody concentration ranging from 4–333 nM. Current resulting from NMDA receptor activation was measured using agarose-tipped microelectrodes (0.4–0.9 MΩ) at a holding potential of −60 mV. Data were acquired using the PatchMaster program (HEKA) and analysed by Origin (OriginLab). The relative effect of antibody treatment was calculated as described in Extended Data Fig. 11a.

In vitro transfection experiments

The *Grin1-2b* expression construct (Fig. 2a; sequence deposited at GenBank PX651955) was generated from the PB-TRE-dCas9-VPR plasmid[93] (a gift from G. Church, Addgene, 63800). The insert between NheI and PmeI was replaced with a codon-optimized insert comprising the canonical mouse GluN1 (UniProt, P35438, GluN1a variant) and GluN2B (UniProt, Q01097) amino acid sequences with a P2A linker.

No fluorophore was included to minimize immunogenicity[94]. Stably transfected 4T1-NMDAR cells were generated by co-transfecting parental 4T1 cells (a gift from M. Egeblad, with identity confirmed by genome sequencing) with the *Grin1-2b* expression construct and the piggyBac transposase vector (System Biosciences, PB210PA-1) using Lipofectamine 3000 according to the manufacturer's instructions. Stably transfected cells were selected by hygromycin (250 µg ml^{-1}) antibiotic treatment for 14 days, before selecting single-cell clones by limiting dilution. *Grin1-2b* transcript induction was determined by performing full-length mRNA sequencing on two vehicle-treated and three 10 ng ml^{-1} DOX-treated (Sigma-Aldrich, D9891) cell aliquots after 48 h of treatment. Raw RNA-seq reads were aligned and quantified using the nf-core/rnaseq[95] pipeline with a custom GRCm38 reference containing the *Grin1-2b* construct, and differential expression analysis was performed using the edgeR package for R[96]. NMDAR protein induction was determined using immunoblots for GluN1 and GluN2B on cell lysates (permeabilized with 1% Triton X-100) after incubating cells with 0–100 ng ml^{-1} DOX for 48 h. To minimize potential cytotoxicity from NMDAR expression, MK801 was added to the medium to a final concentration of 20 µM during DOX induction.

4T1-NMDAR insertion sequencing

To sequence the insert region in stably transfected 4T1-NMDAR clones, we designed a custom 396-probe sequencing panel (Twist Biosciences) targeting the 12 kb insert with significant overlap. Genomic DNA was extracted from 4T1-NMDAR clones ($n = 5$) using the Qiagen DNeasy kit and sequenced on the NextSeq 500 platform. Reads were aligned to the mouse reference genome (GRCm39), and insertion sites (breakend variants) were identified using Manta[97] and manually annotated.

Cytotoxicity assay

4T1-NMDAR cells were seeded into each well of a 48-well plate at a density of 2,500 cells per well in complete growth medium as described above. After 24 h, the medium was replaced with medium containing DOX at 10 ng ml^{-1} and 1 µM MK-801. After an additional 48 h, the medium was replaced with medium containing 47 nM MK-801, as well as IgG (mGO53, SK3D or SK5G) at 33 nM or vehicle (PBS). For dose–response evaluation, cells were incubated with 0–200 nM SK3D IgG. After a final 24 h of antibody incubation, cell viability was measured by sulforhodamine B (SRB) assay (Thermo Fisher Scientific, A14769-06) according to the manufacturer's protocol.

In vivo tumour experiments

For wild-type BALB/c experiments, a total of 50,000 4T1-NMDAR cells suspended in 20 µl of 1:1 PBS and Cultrex (R&D Systems, 3433-005-01) was injected into the left inguinal mammary fat pad of female BALB/cJ mice (aged 8–10 weeks). For *Ighj*-knockout BALB/c mouse experiments, female homozygote mice were obtained from Cyagen (C001345). In total, 100,000 4T1-NMDAR cells suspended in 40 µl of 1:1 PBS and Cultrex (R&D Systems, 3433-005-01) were injected into the left inguinal mammary fat pad of female BALB/c *Ighj*-knockout mice (aged 8 weeks). Once tumours reached a volume of 100mm^3 (approximately 12 days after injection), an osmotic pump (Alzet, 1004) containing 75 mg ml^{-1} filter-sterilized ifenprodil (dissolved in 40% DMSO, 40% water and 20% Cremaphor EL) was implanted subcutaneously. After 48 h, filter-sterilized DOX was added to the drinking water at a final concentration of 0.25 mg ml^{-1}. Mice were monitored regularly until palpable tumours formed, after which the diameter of each tumour was measured every 3–4 days using callipers. Tumour samples were obtained by dissection of mice after euthanasia by cervical dislocation after 14–21 days of DOX treatment for wild-type experiments and 7 days for *Ighi*-knockout experiments. Tumour samples were separated into fractions for cryo-embedding in optimal cutting temperature compound (OCT) and single-cell suspensions, which were immediately stored in prechilled MACS Tissue Solution (Miltenyi Biotec, 130-100-008)

before dissociation. In one experimental sequence, paired tumour and TDLNs were dissected separately are used to prepare tumour suspensions. Blood samples were obtained from tail bleeds and terminal cardiac bleeds and collected in heparin-coated capillary tubes, which were kept on ice before centrifugation at 14,000g for 5 min at 4 °C. The supernatant (plasma) was stored at −80 °C.

Tumour dissociation

Dissected mouse tumours and TDLNs were processed into single-cell suspensions using the mouse Tumour Dissociation Kit (Miltenyi Biotec, 130-096-730) and the gentleMACS Dissociator (Miltenyi Biotec) according to the manufacturer's protocol. Viably frozen human tumours (minced tissue frozen in cryopreservation medium) were processed into single-cell suspensions using the human Tumour Dissociation Kit (Miltenyi Biotec, 130-095-929) and the gentleMACS Dissociator (Miltenyi Biotec) according to the manufacturer's protocol. After red blood cell lysis, cell suspensions were cryopreserved in medium containing 10% DMSO, 50% FBS (tetracycline free) and 40% RPMI 1640.

Bulk RNA-seq analysis

For all bulk RNA-seq, total RNA was extracted using the RNeasy Lipid Tissue Mini Kit (Qiagen, 74804) according to the manufacturer's protocol. RNA was then submitted for full-length paired-end (2 × 150 bp) mRNA-seq with poly(A) pull-down. For mouse tumour profiling, raw RNA-seq reads were aligned and quantified using the nf-core/rnaseq[95] pipeline with a custom GRCm38 reference containing the *Grin1-2b* construct, and differential expression analysis was performed using the edgeR package for R[96]. Relative proportions of immune cell types for imputed using the mMCP-counter package for R[98].

Flow cytometry

To prepare adherent cells for flow cytometry, they were trypsinized and then the trypsin was neutralized with serum-containing medium before cells were resuspended in flow cytometry buffer (PBS with 2% FBS). Cell surface NMDAR protein induction was determined by staining 4T1-NMDAR cells with Alexa-Fluor-488-conjugated 003-102 IgG and measuring the fluorescence signal using the Guava easyCyte system; unstained cells were used as controls. For analysis of cell surface NMDAR expression, cryopreserved tumour suspensions were thawed and stained with LIVE/DEAD Violet (Thermo Fisher Scientific, L23105) before staining with an antibody cocktail containing anti-CD45 (S18009F, PE/Fire 810), anti-GluN1 (003-102, conjugated to Alexa Fluor 488) and anti-GluN2B (IgG2, conjugated to PerCP-Cy5.5). For analysis of mouse intratumoural B cell populations, cryopreserved tumour suspensions were thawed and stained with LIVE/DEAD Violet (Thermo Fisher Scientific, L23105) before staining with an antibody cocktail containing anti-CD45 (S18009F, PE/Fire 810), anti-CD19 (1D3, APC-Cy7), anti-CD138 (Brilliant Violet 711), anti-IgD (11-26 c.2a, Alexa Fluor 488), anti-CD3 (17A2, PE-Cy5) and anti-CD86 (GL1, Brilliant Ultraviolet 737). Staining buffer (PBS with 2% tetracycline-free FBS) included mouse FcR blocking reagent (Miletnyi Biotec, 130-092-575) or human FcR blocking reagent (BioLegend, 422301) as appropriate, as well as Brilliant Stain Buffer (Thermo Fisher Scientific, 00-4409-42). For tumour suspension flow cytometry, cells were analysed using the Dual Fortessa Cell Analyzer (Becton Dickinson). Flow cytometry data were analysed in FlowJo (BD Biosciences). Antibody conjugation was performed using the Lightning-Link kit (Abcam, ab236553) for 003-102 and IgG2.

Western blot

Cells were lysed in TBS containing 1% Triton X-100 and 1 mM PMSF (60 min, 4 °C), and lysates were clarified by centrifugation (21,000g, 60 min, 4 °C). Proteins were separated by SDS−PAGE (8% polyacrylamide), transferred to nitrocellulose and blocked in 5% milk. Membranes were probed with anti-GluN1 (Cell Signaling, 5704, 1:1,000) or anti-GluN2B (Cell Signaling, 4207, 1:1,000) antibodies, followed by HRP-conjugated secondary antibodies. Signals were detected using ECL Prime reagent (Amersham).

scRNA-seq analysis

On the day of sequencing, mouse tumour cell suspensions were thawed and stained with LIVE/DEAD Violet (Thermo Fisher Scientific, L23105) before an antibody cocktail containing anti-CD3 (17A2, PE-Cy5), anti-CD19 (1D3, PE/AF700) and anti-CD45 (S18009F, PE/Fire 810). Staining buffer (PBS with 2% tetracycline-free PBS) included mouse FcR blocking reagent (Miletnyi Biotec, 130-092-575). Cells were then combined with biotinylated NMDAR protein conjugated with Streptavidin-PE-Oligo complexes (10x Genomics, BEAM-Ab conjugates) according to the manufacturer's protocol (10 Genomics, CG000595). When pooling samples from multiple mice, each suspension was incubated with anti-mouse hashing antibodies (BioLegend, TotalSeq-C). For pilot experiments before the public release of the 10x Genomics BEAM-Ab conjugates, we conjugated NMDARs to TotalSeq-C Streptavidin-PE-Oligo (5:1 molar ratio) and quenched the reaction with 200 nM biotin. Cells were sorted using a SH800 Cell Sorter (Sony); representative compensated gating plots to enrich for NMDAR-binding B cells are shown in Supplementary Fig. 3d. To profile cancer cells, the B cell fraction was mixed with CD45− cells before library preparation. To profile TNBC cryopreserved tumour suspensions, cells were thawed, washed and immediately loaded onto the 10x Chromium chip without sorting or additional processing.

Sorted cells were counted using the Countess II FL automated cell counter using 1:1 acridine orange/propidium iodide (AO/PI) stain (Revvity CS2-0106) before loading the 10× Chromium chips according to the manufacturer's recommendations. Single-cell gene expression, B cell receptor (BCR), antigen capture (BEAM) and feature barcoding (used for cell hashing) libraries were prepared using the Single Cell 5′ Gene Expression v2 kit with the feature barcoding library prep kit (10× Genomics, 1000263 and 1000541). For pilot experiments before the release of the 10x Genomics BEAM-Ab conjugates, single-cell gene expression and BCR libraries were prepared using the Single Cell 5′ Gene Expression kit v1.1 (10× Genomics, 1000165). TotalSeq-C libraries were generated by spiking in 1 µl of 0.5 µM Totalseq-C cDNA primer (CGGAGATGTGTATAAGAGACAG) to the cDNA amplification step and performing a 2× solid-phase reversible immobilization (SPRI) cleanup on the supernatant of the cDNA SPRI cleanup. Final TotalSeq-C libraries were generated by amplifying cDNA with the AATGATAC GGCGACCACCGAGATCTACACTCTTTCCCTACACGACGCTCTTCCG and CAAGCAGAAGACGGCATACGAGATCTCAAGTCGTCTCGTGGGCTCGG AGATGTGTATAAG primers. Libraries were sequenced using the Illumina NextSeq 2000 system. Sequencing data were processed using the Cell Ranger v.7.2.0 multi pipeline (10x Genomics) for BEAM datasets. A custom reference genome was generated to include the *Grin1-2b* construct. Transcriptional data were analysed using Seurat[99] (v.5.1.0) for R. B cell receptor sequencing data were analysed using Loupe VDJ Browser (10x Genomics) and enclone[100] (10x Genomics). Germline inference was performed using the partis software library[101] using a BALB/c-specific VDJ reference. Mitochondrial mutations were detected using the VarTrix software library (10x Genomics, https://github.com/10XGenomics/vartrix). For downstream analyses, 4T1 cancer cells were defined by inclusion within the transcriptional cluster with high *Hmga2* expression and an alt/alt genotype call for the chrM:1576-T-C variant. TNBC cancer cells were defined by copy-number variation profiling implemented in the inferCNV package for R[102].

Bioinformatic prioritization of antibody sequences

To prioritize B cell clones most likely to produce NMDAR-specific antibodies, we manually integrated multiple bioinformatic parameters, including B cell differentiation status, immunoglobulin class switching events, clonal expansion patterns and antigen specificity scores. B cells were classified by their differentiation state and whether

they had undergone class switching to IgG, indicating a more mature, antigen-experienced phenotype. Clonal relationships were determined by identifying B cells that shared common ancestral sequences within expanded phylogenetic groups (clonotypes), as implemented in enclone[100] (10x Genomics). For each B cell, we calculated an antigen specificity score calculated from NMDAR–oligo and albumin–oligo counts[103], which quantifies the probability of NMDAR binding versus non-specific albumin binding. These integrated parameters enabled us to rank and prioritize B cell clones on the basis of their likelihood of producing high-affinity, NMDAR-specific antibodies, which were then further validated functionally through recombinant expression.

Validation of mouse-derived antibody sequences
To screen either tumour- or TDLN-derived sequences for binding, expression plasmids were cloned containing variable regions for each antibody sequence (Twist Biosciences) on an IgG1 framework (Fig. 3a). For tumour-derived sequences, antibodies were expressed recombinantly and purified by protein A affinity chromatography as described above, before screening by NMDAR-specific ELISA. For TDLN-derived sequences, given the higher number of sequences, screening was performed by transient transfection. In brief, HEK293 GnTi- cells grown in serum-free Freestyle 293 medium were seeded into 24-well plates at a density of 500,000 cells per well, before transfection using TransIT-2020 (Mirus Bio, MIR5404) according to the manufacturer's protocol, with the inclusion of untransfected controls and a strong binder (003-102) positive control. Transfection efficiency was verified by GFP fluorescence. After 72 h of transfection, the cell culture supernatant for each well was collected. Specific NMDAR binding was screened by ELISA using serially diluted supernatant starting at 1:2. For TDLN-derived sequences, a positive result was defined as OD > 0.1 with twofold dilution.

In vivo intracerebroventricular antibody infusion experiments
Mice were allowed to acclimatize for at least 1 week after their arrival at the Cold Spring Harbor Laboratory animal facility. We performed stereotaxic brain surgery on isoflurane-anaesthetized mice to implant a sterile stainless-steel cannula (Alzet, 0004760) into the right lateral ventricle. This intracerebroventricular cannula was connected to a subcutaneous programmable and refillable pump (Alzet, iPRECIO SMP-310R) loaded with sterile PBS and set at an infusion rate of 0.5 µl h^{-1}. Post-operatively, mice were allowed to recover for at least 5 days before enrolment in the study, at which point, the contents of the pump reservoir were removed and replaced with either mGO53, SK3D or SK5G (mice selected at random). Seizures were induced with a single intraperitoneal dose of 20 mg per kg filter-sterilized PTZ (Selleck Chemicals, S4587) diluted in PBS. Mice were euthanized if a seizure extended for more than 5 min. Seizure activity in the 10 min after intraperitoneal injection was monitored by filming mice and was scored according to established criteria[104]. Mice were infused with either mGO53, SK3D or SK5G for 14 days, with the pumps refilled once after 7 days. At the end of the study, mice were perfused with 0.9% saline before dissecting brains, which were cryo-embedded in OCT.

Metabolic cage profiling
Mice were singly housed in cages as part of the Comprehensive Lab Animal Monitoring System (CLAMS) from Columbus Instruments. This platform allows precise monitoring of food and water intake, activity and energy expenditure (by open circuit calorimetry). Data were extracted into tabular format using Oxymax for Windows (v.5.71) and analysed using custom R scripts. Energy expenditure was computed using measured concentrations of oxygen and carbon dioxide, as described previously[105]. Data entries that generated negative values for VO$_2$/VCO$_2$ or outlier respiratory exchange ratio values (<0.3 or >1.6) were removed. Total activity was computed using CalR (v.2)[106]. Energy expenditure data were adjusted for relevant covariates using

ANCOVA analyses implemented using the glm function in R, according to established guidance in the field[107,108]. For each ANCOVA analysis, we confirmed that the treatment–covariate interaction term was not significant. In a separate experiment, healthy female C57BL/6 mice received a single intraperitoneal dose of 0.5 mg ketamine after acclimatizing to metabolic cages for 1 week.

Bioinformatic analysis of human data
Molecular Taxonomy of Breast Cancer International Consortium (METABRIC) RNA profiling (microarray) data were downloaded from cBioPortal, while The Cancer Genome Atlas (TCGA)-BRCA RNA-seq data were downloaded from UCSC Xena Browser. TCGA reverse-phase protein array data from TCGA-BRCA were downloaded from cBioPortal. TNBC annotations for METABRIC and TCGA were extracted from a published study[109]. For each dataset, tumours were stratified by ER, PR and HER2 status, and *GRIN1*/*GRIN2B* expression levels were compared using Wilcoxon rank-sum tests. Human thymus scRNA-seq data[33] were downloaded from https://cellxgene.cziscience.com/e/63b0a978-5820-4c3a-96a8-af098c1b0166.cxg/ and processed using Seurat[99] (v.5.1.0) for R.

Spatial RNA profiling
Vendor-supplied slides (Origene, patient ID: FR001D525) were fixed in 4% paraformaldehyde (PFA) in PBS for 30 min at room temperature then washed in 1× PBS for 1 min before proceeding to step 3.2 (H&E staining) to 3.7 (decrosslinking) of the Visium FFPE Handbook (10x Genomics, protocol ID CG000684). Slides were imaged using an Olympus VS200. The Human Visium HD Spatial Gene Expression assay (10x Genomics, PN:1000675) was performed according to the manufacturer's instructions (10x Genomics CG000495), and libraries were sequenced on the Illumina NextSeq 2000 system to target 900 million reads per capture area. Sequenced reads were mapped to the Visium Human Transcriptome Probe Set v.2.0 and aligned to their spots in the paired H&E images using Space Ranger v.3.0.0 (10x Genomics). White-space regions were manually removed using Loupe Browser v.8.0.0 (10x Genomics) before downstream analysis using Seurat[99] (v.5.1.0) for R. Visium analysis in Seurat was performed according to the authors' documentation (https://satijalab.org/seurat/articles/visiumhd_analysis_vignette).

Immunohistochemistry
Immunohistochemical slides were stained on a DISCOVERY ULTRA Research Staining System (Roche) according to the manufacturer's protocol. Acetone fixation was used for all immunohistochemical stains, without an additional permeabilization step. After fixation and quenching of endogenous peroxidases, the slides were incubated with primary antibodies at 37 °C for 1 h. The Discovery multimer detection system (Discovery OmniMap HRP and/or Discovery DAB, Roche) was used to amplify and/or detect immunosignals. The primary antibodies used were anti-DYKDDDDK (Flag) tag (Cell Signaling Technology, 14793, 1:500) and HRP-conjugated anti-GluN2B (IgG2 (ref. 32), 1:250). Slides were scanned using the Olympus VS200 scanner. Scanned images were analysed using QuPath[110] (v.0.5.1)

In situ hybridization (RNAscope)
RNAscope was performed using RNAscope 2.5 HD Detection Reagent Red (322360, Advanced Cell Diagnostics) according to the manufacturer's protocol. Mouse tissue sections were hybridized with a custom RNAscope probe that was designed to bind specifically to the *Grin1-2b* insert.

IF analysis
Sections from fresh-frozen TNBC tissue (Origene) were fixed in 4% PFA for 15 min at room temperature and washed in PBS. Sections from fresh frozen mouse 4T1 tumours were fixed in either 4% PFA (for immune cell

marker antibodies) at room temperature or acetone (for anti-NMDAR antibodies) at 4 °C for 10 min and washed in PBS. PFA-fixed tissue sections were then permeabilized with 0.2% Triton X-100 in PBS and washed in PBS. All of the tissue sections were blocked with 10% donkey serum in PBS with Tween detergent (PBST, 0.05% Tween-20) and incubated with fluorophore-conjugated primary antibodies diluted in PBST + 3% donkey serum at 4 °C overnight. After incubation, the sections were washed twice in PBST and once in PBS, each for 5 min, incubated with DAPI solution (1 µg ml^{-1}), and mounted in ProLong Glass Antifade Mountant (P36980, Thermo Fisher Scientific). The images in Fig. 1f were taken using the Zeiss LSM710 Confocal Microscope, and images in Figs. 2h and 6d, Supplementary Fig. 2 and Extended Data Figs. 3c and 12e were taken using the Zeiss LSM 980 Confocal Laser Scanning Microscope (Carl Zeiss Microscopy), with a Plan-Apochromat ×20/0.8 NA air objective lens, and a 32-channel gallium arsenide phosphide (GaAsP) detector. Low-power full views of tumour sections were obtained through tile scanning and stitched using Zeiss ZEN Blue v.3.8.2. Raw images were processed using Fiji/ImageJ[111], using functions for background subtraction (25 px) and despeckling. Cell classification and quantification were done using QuPath[110]. For Fig. 1f, the NMDAR antibodies used were 003-102 conjugated to Alexa Fluor 488 and IgG2 conjugated to PerCP-Cy5.5, with conjugation performed using the Lightning-Link kit (Abcam). For Fig. 6d and Supplementary Fig. 2, the NMDAR antibodies were 003-102 conjugated to Alexa Fluor 488 and IgG2 conjugated to Alexa Fluor 594, both used at 1:150 dilution. For all other images, the antibodies used were CoraLite Plus 555 anti-Mouse CD45R (CL555-65139, Proteintech), 1:100 dilution; Alexa Fluor 647 anti-mouse CD3 (100209, BioLegend), 1:100 dilution; and Alexa Fluor 750 anti-pan-cytokeratin (NBP1-48348-AF750, Novus Biologicals), 1:200 dilution.

Quantification and statistical analysis
Data are expressed as the mean ± s.e.m. unless otherwise stated in figure legends. Statistical tests refer to unpaired two-tailed Student's t-tests unless otherwise stated in figure legends. Wilcoxon rank-sum tests adjusted for multiple comparisons were used for gene expression comparisons between gene expression clusters. All measurements were taken from distinct samples unless otherwise stated in figure legends. Analyses were performed in R (v.4.4.0).

Material availability
On reasonable request, 4T1-NMDAR cells will be available under a material transfer agreement with CSHL. *Ighj*-knockout mice can be obtained from Cyagen.

Reporting summary
Further information on research design is available in the Nature Portfolio Reporting Summary linked to this article.

Data availability
New datasets generated were as follows. Cryo-EM maps and structural models (containing antibody amino acid sequences) have been deposited at the Electron Microscopy Data Bank (EMDB) and PDB, under accession codes 1OFE, 1OEV, 1OEN, 1OEY, 1OFF, 1OFD, 1OEX, 1OEZ, 1OFL, 1OFN and 1OFO. The plasmid sequence for the PB-TRE-Grin construct was deposited at GenBank under accession number PX651955. Raw bulk RNA-seq data have been deposited in NCBI Sequence Read Archive (SRA) under project ID PRJNA1370999. Raw mouse-derived scRNA-seq data have been deposited in NCBI SRA under project ID PRJNA1371359. Raw human-derived scRNA-seq and Visium HD data have been deposited in the European Genome-phenome Archive (EGA) under accession numbers EGAD50000002266 and EGAD50000002284. These data are stored with restricted access to protect patient privacy. Mouse- and human-derived 10x Genomics output data directories without read

alignments (scRNA-seq, Visium HD), corresponding processed Seurat matrices and configuration files for cellranger multi have been deposited at Mendeley Data (https://doi.org/10.17632/mgb9r3tgz8.1). Processed count matrices have been deposited at Mendeley Data (https://doi.org/10.17632/5tyv4xggpc.1). Publicly available datasets used in this study were as follows. Processed scRNA-seq data from published human thymus samples is available from CELLxGENE (https://cellxgene.cziscience.com/collections/fc19ae6c-d7c1-4dce-b703-62c5d52061b4), while raw data is available from the European Nucleotide Archive under study accession PRJEB77091. Breast cancer clinicopathological, protein array (where available) and processed RNA-seq data are available from cBioPortal for TCGA-BRCA (https://www.cbioportal.org/study/summary?id=brca_tcga_pan_can_atlas_2018) and METABRIC (https://www.cbioportal.org/study/summary?id=brca_metabric). Count-level bulk RNA-seq data for TCGA-BRCA are available from UCSC Xena (https://xenabrowser.net/datapages/?cohort=GDC%20TCGA%20Breast%20Cancer%20(BRCA)&removeHub=https%3A%2F%2Fxena.treehouse.gi.ucsc.edu%3A443). Published cryo-EM models referenced in this paper are available from PDB with accession codes 6wi0, 7SAA, 9ARF, 8VUV, 8VUN, 8VUY, 8VUS, 8JJ1 and 8JIZ.

Code availability
Code notebooks comprising R scripts and resource files required to reproduce RNA-seq, single-cell and Visium HD analyses are available from Github (https://github.com/Janowitz-Lab/nmdar) and have been deposited in Mendeley Data (https://doi.org/10.17632/3d7wfzbg2t.1).

71. Gucalp, A. et al. Male breast cancer: a disease distinct from female breast cancer. *Breast Cancer Res. Treat.* **173**, 37–48 (2019).
72. Dalmau, J. et al. An update on anti-NMDA receptor encephalitis for neurologists and psychiatrists: mechanisms and models. *Lancet Neurol.* **18**, 1045–1057 (2019).
73. Titulaer, M. J. et al. Treatment and prognostic factors for long-term outcome in patients with anti-NMDA receptor encephalitis: an observational cohort study. *Lancet Neurol.* **12**, 157–165 (2013).
74. Will, A. & Akalin, M. Paraneoplastic limbic encephalitis with NMDA receptor (NR1) antibodies in breast cancer. *Neurology* **78**, S08.007 (2012).
75. Viaccoz, A. et al. Clinical specificities of adult male patients with NMDA receptor antibodies encephalitis. *Neurology* **82**, 556–563 (2014).
76. Miao, A. et al. Analysis of relation between electroclinical features and cerebrospinal fluid antibody titers in patients with anti-NMDAR encephalitis. *Clin. EEG Neurosci.* **50**, 56–62 (2018).
77. Cyr, M. et al. Ovarian steroids and selective estrogen receptor modulators activity on rat brain NMDA and AMPA receptors. *Brain Res. Rev.* **37**, 153–161 (2001).
78. Furukawa, H., Simorowski, N. & Michalski, K. Effective production of oligomeric membrane proteins by EarlyBac-insect cell system. *Methods Enzymol.* **653**, 3–19 (2021).
79. Lima, W. C. et al. The ABCD database: a repository for chemically defined antibodies. *Nucleic Acids Res.* **48**, D261–D264 (2019).
80. Lo, M. et al. Effector-attenuating substitutions that maintain antibody stability and reduce toxicity in mice. *J. Biol. Chem.* **292**, 3900–3908 (2017).
81. Nussenzweig, M. C. et al. Polyreactivity ELISA. *Caltech Information Management Systems and Services* https://www.its.caltech.edu/%7Ebjorker/Polyreactivity%20ELISA_Bjorklab012013.pdf (2013).
82. Moritz, C. P., Tholance, Y., Lassablière, F., Camdessanché, J.-P. & Antoine, J.-C. Reducing the risk of misdiagnosis of indirect ELISA by normalizing serum-specific background noise: the example of detecting anti-FGFR3 autoantibodies. *J. Immunol. Methods* **466**, 52–56 (2019).
83. Krämer, S. D., Wöhrle, J., Rath, C. & Roth, G. Anabel: an online tool for the real-time kinetic analysis of binding events. *Bioinform. Biol. Insights* **13**, 1177932218821383 (2019).
84. Tegunov, D. & Cramer, P. Real-time cryo-electron microscopy data preprocessing with Warp. *Nat. Methods* **16**, 1146–1152 (2019).
85. Scheres, S. H. W. RELION: implementation of a Bayesian approach to cryo-EM structure determination. *J. Struct. Biol.* **180**, 519–530 (2012).
86. Punjani, A., Rubinstein, J. L., Fleet, D. J. & Brubaker, M., A. cryoSPARC: algorithms for rapid unsupervised cryo-EM structure determination. *Nat. Methods* **14**, 290–296 (2017).
87. Chou, T.-H. et al. Structural insights into binding of therapeutic channel blockers in NMDA receptors. *Nat. Struct. Mol. Biol.* **29**, 507–518 (2022).
88. Dunbar, J. et al. SAbDab: the structural antibody database. *Nucleic Acids Res.* **42**, D1140–D1146 (2014).
89. Jamali, K. et al. Automated model building and protein identification in cryo-EM maps. *Nature* **628**, 450–457 (2024).
90. Meng, E. C. et al. UCSF ChimeraX: tools for structure building and analysis. *Protein Sci.* **32**, e4792 (2023).
91. Emsley, P., Lohkamp, B., Scott, W. G. & Cowtan, K. Features and development of Coot. *Acta Crystallogr. D* **66**, 486–501 (2010).
92. Adams, P. D. et al. PHENIX: a comprehensive Python-based system for macromolecular structure solution. *Acta Crystallogr. D* **66**, 213–221 (2010).

Article

93. Chavez, A. et al. Highly efficient Cas9-mediated transcriptional programming. *Nat. Methods* **12**, 326–328 (2015).
94. Grzelak, C. A. et al. Elimination of fluorescent protein immunogenicity permits modeling of metastasis in immune-competent settings. *Cancer Cell* **40**, 1–2 (2022).
95. Ewels, P. A. et al. The nf-core framework for community-curated bioinformatics pipelines. *Nat. Biotechnol.* **38**, 276–278 (2020).
96. Robinson, M. D., McCarthy, D. J. & Smyth, G. K. edgeR: a Bioconductor package for differential expression analysis of digital gene expression data. *Bioinformatics* **26**, 139–140 (2009).
97. Chen, X. et al. Manta: rapid detection of structural variants and indels for germline and cancer sequencing applications. *Bioinformatics* **32**, 1220–1222 (2015).
98. Petitprez, F. et al. The murine Microenvironment Cell Population counter method to estimate abundance of tissue-infiltrating immune and stromal cell populations in murine samples using gene expression. *Genome Med.* **12**, 86 (2020).
99. Satija, R., Farrell, J. A., Gennert, D., Schier, A. F. & Regev, A. Spatial reconstruction of single-cell gene expression data. *Nat. Biotechnol.* **33**, 495–502 (2015).
100. Jaffe, D. B. et al. enclone: precision clonotyping and analysis of immune receptors. Preprint at *bioRxiv* https://doi.org/10.1101/2022.04.21.489084 (2022).
101. Ralph, D. K. & Matsen, F. A. Per-sample immunoglobulin germline inference from B cell receptor deep sequencing data. *PLoS Comput. Biol.* **15**, e1007133 (2019).
102. Patel, A. P. et al. Single-cell RNA-seq highlights intratumoral heterogeneity in primary glioblastoma. *Science* **344**, 1396–1401 (2014).
103. 10x Genomics. Cell Ranger's antigen capture (BEAM) algorithm. https://www.10xgenomics.com/support/software/cell-ranger/latest/algorithms-overview/cr-5p-antigen-algorithm (accessed 26 February 2026).
104. Erum, J. V., Dam, D. V. & Deyn, P. P. D. PTZ-induced seizures in mice require a revised Racine scale. *Epilepsy Behav.* **95**, 51–55 (2019).
105. Nie, Y., Gavin, T. P. & Kuang, S. Measurement of resting energy metabolism in mice using Oxymax open circuit indirect calorimeter. *Bio Protoc.* **5**, e1602 (2015).
106. Mina, A. I. et al. CalR: a web-based analysis tool for indirect calorimetry experiments. *Cell Metab.* **28**, 656–666 (2018).
107. Tschöp, M. H. et al. A guide to analysis of mouse energy metabolism. *Nat. Methods* **9**, 57–63 (2012).
108. Müller, T. D., Klingenspor, M. & Tschöp, M. H. Revisiting energy expenditure: how to correct mouse metabolic rate for body mass. *Nat. Metab.* **3**, 1134–1136 (2021).
109. Lehmann, B. D. et al. Multi-omics analysis identifies therapeutic vulnerabilities in triple-negative breast cancer subtypes. *Nat. Commun.* **12**, 6276 (2021).
110. Bankhead, P. et al. QuPath: open source software for digital pathology image analysis. *Sci Rep.* **7**, 16878 (2017).
111. Schindelin, J. et al. Fiji: an open-source platform for biological-image analysis. *Nat. Methods* **9**, 676–682 (2012).

Additional information
Supplementary information The online version contains supplementary material available at https://doi.org/10.1038/s41586-026-10278-0.
Correspondence and requests for materials should be addressed to Hiro Furukawa or Tobias Janowitz.
**Peer review information** *Nature* thanks Ziv Shulman and the other, anonymous, reviewer(s) for their contribution to the peer review of this work. Peer reviewer reports are available.
Reprints and permissions information is available at http://www.nature.com/reprints.
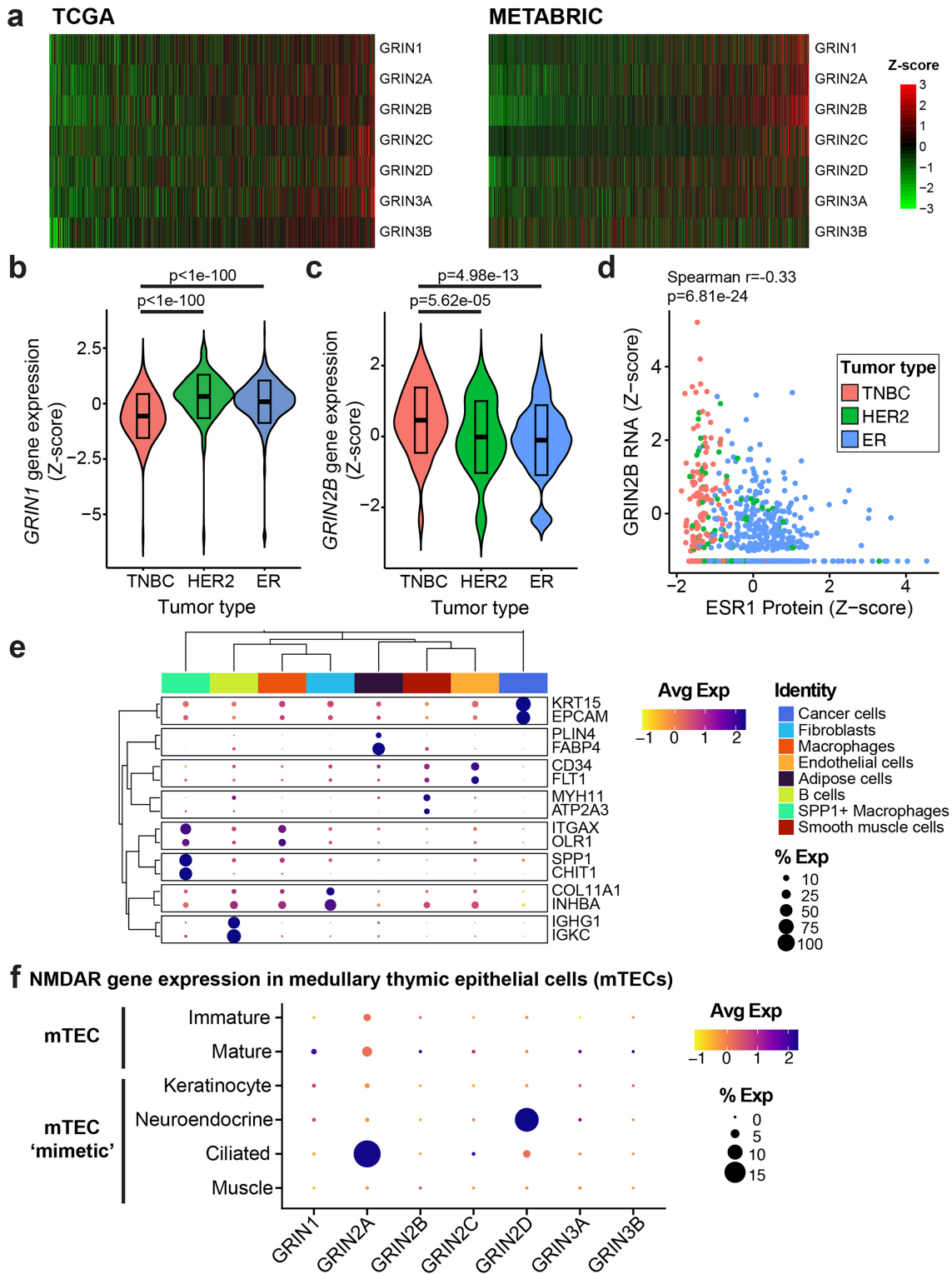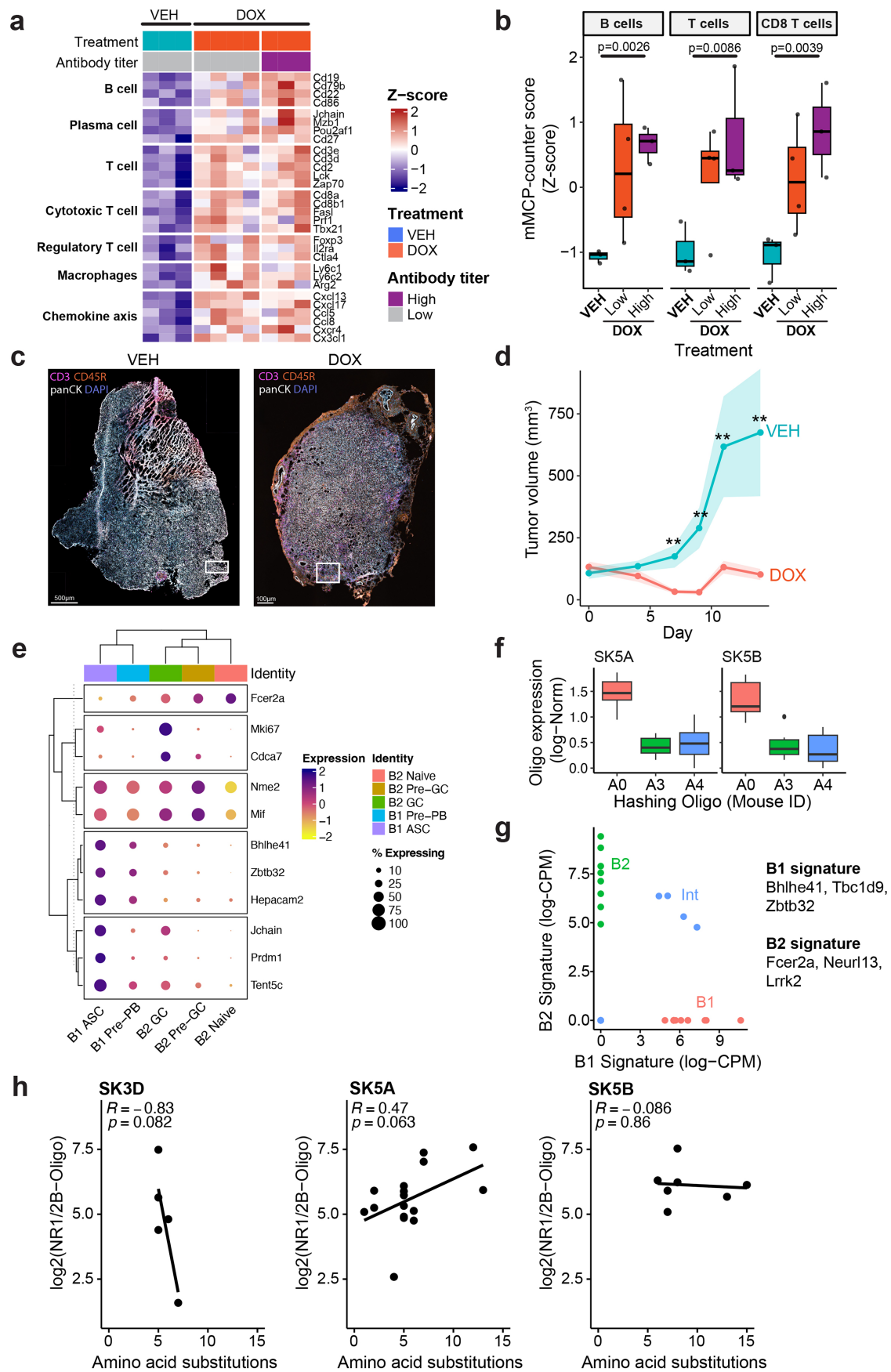
Extended Data Fig. 1 | related to Fig. 1: NMDAR sub-unit expression in human samples. a-b, Heatmap showing the RNA expression of NMDAR genes in each breast cancer tumour annotated in the TCGA **(left)** and METABRIC **(right)** cohorts. **b-c,** Z-scored *GRIN1* **(b)** and *GRIN2B* **(c)** gene expression in the TCGA cohort, stratified by tumour molecular subtype. **d,** Scatter plot of Z-scored *GRIN2B* gene expression as a function of Z-scored oestrogen receptor (ESR1) protein expression, annotated with the Spearman correlation coefficient and p-value. The colour of each point reflects the tumour molecular subtype.

e, Dot plot showing differentially expressed canonical marker gene expression in each spatial RNA profiling bin cluster, annotated with the percentage of bins expressing each gene (point size) and the scaled gene expression (point colour). **f,** Dot plot showing expression of NMDAR genes in a published atlas of medullary thymic epithelial cells (TECs) including mature (*CCL21*^{+}MHCII[lo]*AIRE*[−]), immature (*AIRE*[+]MHCII[hi]) and 'mimetic' mTEC populations. 'Mimetic' populations included those resembling keratinocytes (*IVL*[+]*KRT10*^{+}), neuroendocrine (*NEUROD1*^{+}), muscle (*MYOG*[+]), and ciliated cells (*FOXJ1*^{+}).

a

Grin1-2b insert

b

c

d

e

Correlation with Grin1-2b insert

f

Slc7a11
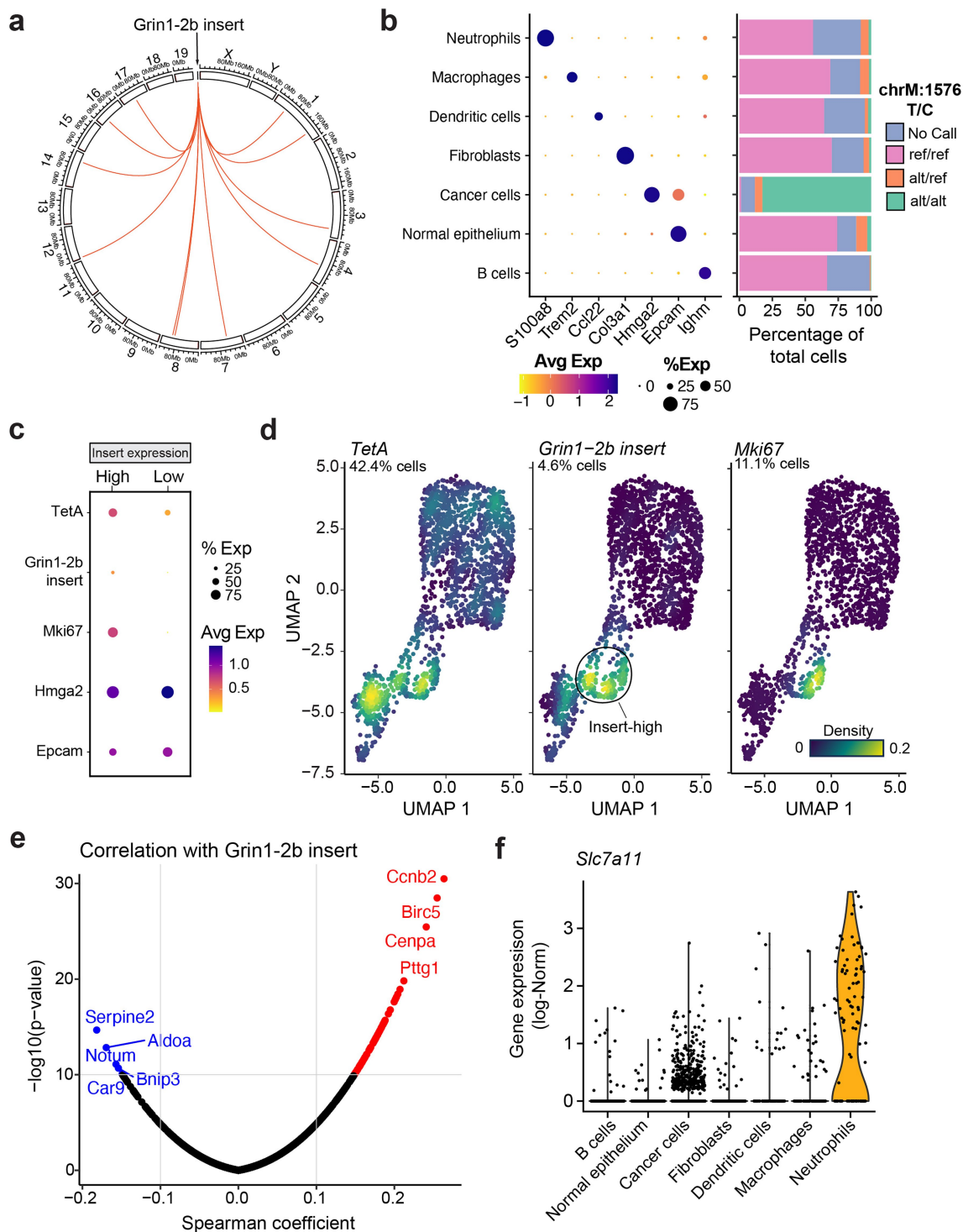
Extended Data Fig. 2 | related to Fig. 2: Characterization of the 4T1-NMDAR tumour model. a, Circos plot showing the genomic integration sites for the *Grin1-2b* insert, determined by overlapping targeted sequencing of the insert. **b**, Dot plot of marker gene expression used to define cell cluster identity in scRNA-seq of 4T1-NMDAR tumours, annotated with the scaled gene expression and the percentage of cells expressing each gene (left panel). *Hmga2* is a known marker gene for 4T1 cells. This dot plot is annotated with the relative frequency of 4T1-specific mtDNA mutation in each intratumoral cell cluster (right panel). Only cancer cells with alt/alt genotypes were used for downstream cancer cell-specific analyses. **c**, Dot plot showing expression of *TetA*, *Grin1-2b insert* and *Mki67* in comparison to cancer cell markers (*Hmga2* and *Epcam*) in *Grin1-2b*

insert-high and low cancer cell clusters. **d**, Feature plot showing UMAP projection of 4T1-NMDAR tumour-derived cancer cells, annotated with density of tetracycline-controlled transactivator (*TetA*), *Grin1-2b insert*, and *Mki67* expression. Each figure is annotated with the percentage of non-zero expressing cells. The *Grin1-2b insert*-high cluster is highlighted (black oval), within this cluster 65% and 22% of cells express *TetA* and *Grin1-2b insert*, respectively. **e**, Volcano plot showing pairwise correlation between the *Grin1-2b insert* and each detected gene, plotted against the -log10(p-value) for the association. Significantly positively associated genes (red) are known to be associated with the G2/M cell cycle transition. **f**, Violin plot showing expressing of Slc7a11 in each intratumoral population (all cells).
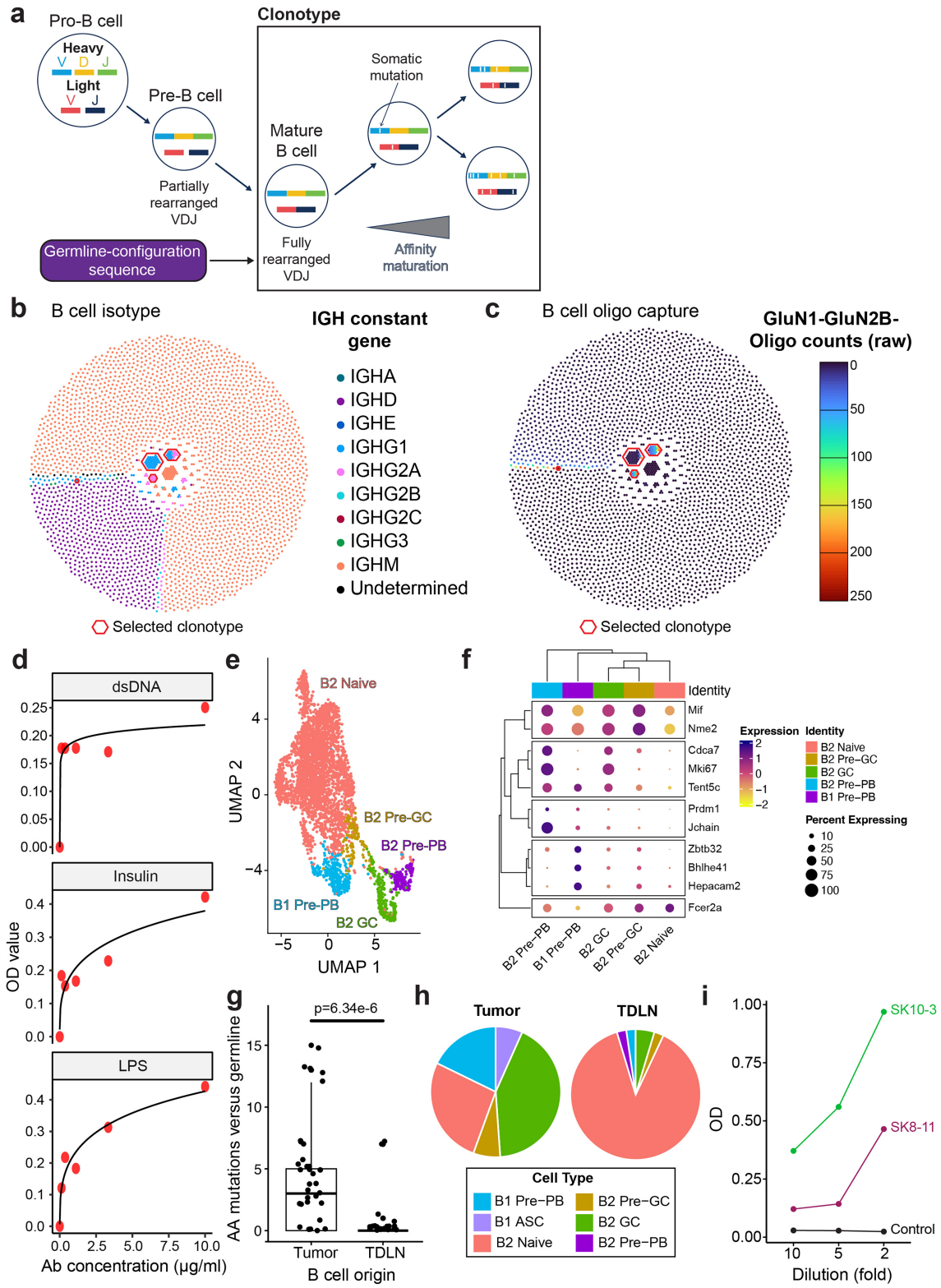
Extended Data Fig. 3 | See next page for caption.

Article

Extended Data Fig. 3 | related to Figs. 2, 3: Immune profiling and B cell populations in 4T1-NMDAR tumours. a, Heatmap showing relative expression (Z-scored) of immune cell marker genes determined by bulk RNA-seq in 4T1-NMDAR tumours from mice treated with vehicle (VEH) or doxycycline (DOX). Mice are stratified by plasma anti-NMDAR antibody titres: high (>500 ng/ml) or low (<500 ng/ml). All genes were differentially expressed between VEH- and DOX-treated tumours at FDR < 0.05. **b**, Estimated relative proportions of B cells, T cells and CD8 T cells determined by RNA-seq deconvolution in 4T1-NMDAR tumours treated with VEH or DOX, stratified by plasma antibody levels. **c**, Representative immunofluorescence staining for CD3 (T cells), CD45R (B cells), and panCK (tumour cells) in VEH- and DOX-treated tumours. White boxes indicate the tumour margin regions shown at higher magnification in Fig. 2h. **d**, Tumour growth curves comparing VEH- versus DOX-treated 4T1 tumours over time. Lines show mean tumour volume; shaded areas represent SEM. **e**, Differentially expressed canonical marker gene expression in each B cell population, annotated with the percentage of cells expressing each gene. *Bhlhe41* and *Fcer2a* were used to identify B1 and B2 cells, respectively. *Nme2* and *Mki67* were used to identify pre-germinal centre (GC) and GC B cells, respectively. High *Jchain* and *Prdm1* expression was used to discriminate between antibody-secreting cell (ASC) and pre-plasmablast (PB) states. **f**, Boxplot showing log-normalized expression of 3 hashing oligos (reflecting cell origin from a single mouse) for SK5A and SK5B clonotypes. The solid black line signifies the median and the grey-outlined box signifies the interquartile range. **g**, Scatter plot showing log-normalized expression of B2 versus B1 B cell gene expression signatures. The genes making up each signature are annotated. **h**, Scatter plot showing, in each expanded clonotype, the log-normalized B cell capture of the NMDAR-tagged oligo as a function of the degree of affinity maturation, defined as the number of amino acid substitutions compared to the germline configuration sequence. **, p < 0.01.

a Pro-B cell

Heavy V D J
Light V J

Pre-B cell

Partially rearranged VDJ

Germline-configuration sequence

Clonotype

Mature B cell

Fully rearranged VDJ

Somatic mutation

Affinity maturation

b B cell isotype

IGH constant gene

- IGHA
- IGHD
- IGHE
- IGHG1
- IGHG2A
- IGHG2B
- IGHG2C
- IGHG3
- IGHM
- Undetermined

⬡ Selected clonotype

c B cell oligo capture

GluN1-GluN2B-Oligo counts (raw)

0 — 50 — 100 — 150 — 200 — 250

⬡ Selected clonotype

d

dsDNA

Insulin

LPS

OD value

Ab concentration (µg/ml)

e

B2 Naive

B2 Pre-GC

B2 Pre-PB

B1 Pre-PB

B2 GC

UMAP 2

UMAP 1

f

Identity

Mif
Nme2
Cdca7
Mki67
Tent5c
Prdm1
Jchain
Zbtb32
Bhlhe41
Hepacam2
Fcer2a

B2 Pre-PB
B1 Pre-PB
B2 GC
B2 Pre-GC
B2 Naive

Expression
2
1
0
-1
-2

Identity
- B2 Naive
- B2 Pre-GC
- B2 GC
- B2 Pre-PB
- B1 Pre-PB

Percent Expressing
- 10
- 25
- 50
- 75
- 100

g

p=6.34e-6

AA mutations versus germline

Tumor   TDLN

B cell origin

h

Tumor   TDLN

Cell Type
- B1 Pre-PB
- B1 ASC
- B2 Naive
- B2 Pre-GC
- B2 GC
- B2 Pre-PB

i

SK10-3

SK8-11

Control

OD

Dilution (fold)

10   5   2

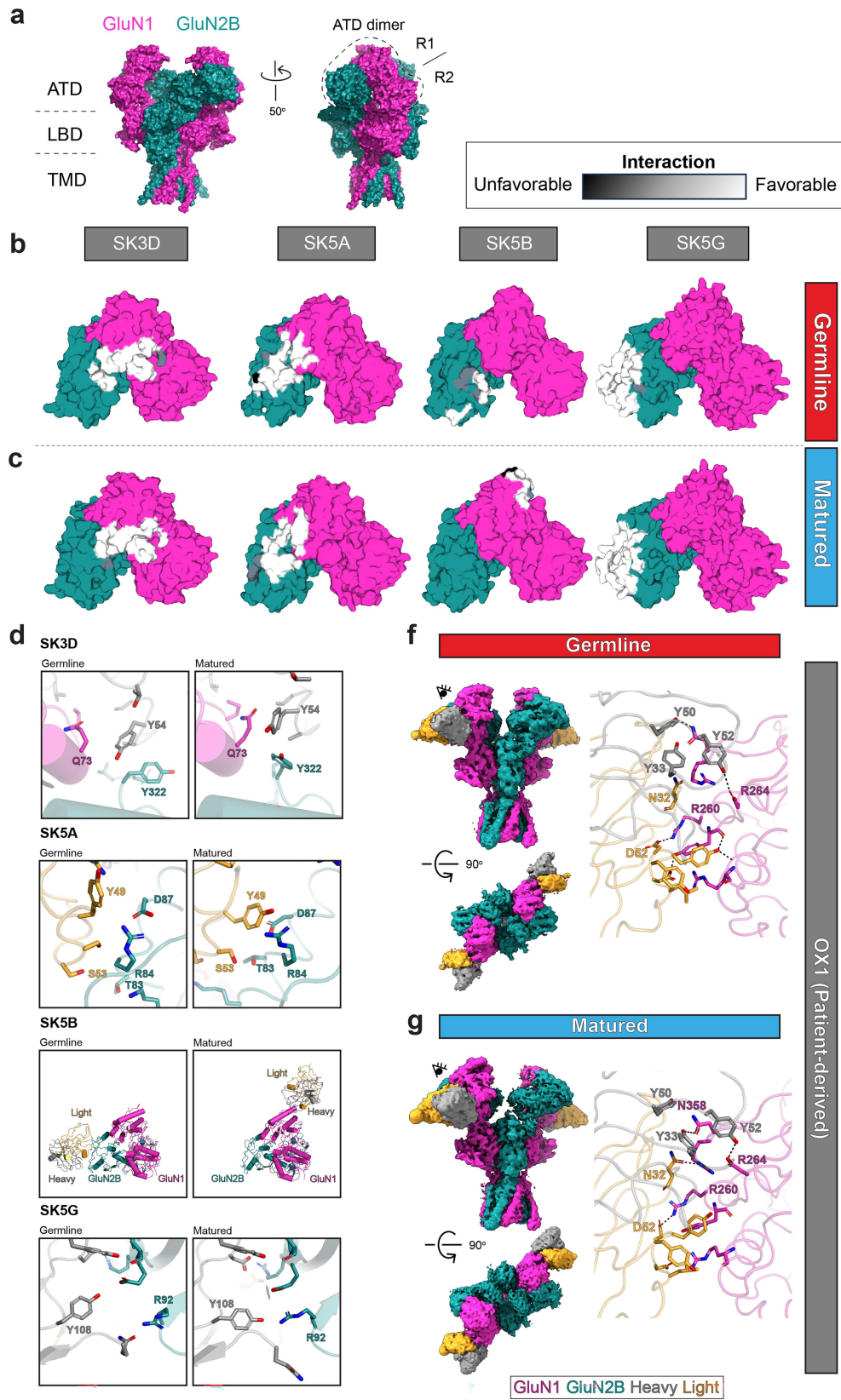**Extended Data Fig. 4** | See next page for caption.

Article

Extended Data Fig. 4 | related to Fig. 3: Identification and validation of NMDAR-reactive B cell clonotypes. a, Schematic representation of the VDJ recombination process. The B cells derived from a B cell with a fully rearranged VDJ region are referred to as a clonotype. The fully rearranged VDJ is often referred to as the unmutated common ancestor (UCA) or the germline-configuration sequence, as this is the direct product of VDJ recombination without any somatic mutations that would normally arise as part of B cell activation and affinity maturation. Figure modified from https://10xgenomics.github.io/enclone/. **b-c**, Honeycomb plot showing all 3,180 B cells isolated as part of this study, annotated with their heavy chain constant region **(b)** and NMDAR-tagged oligo capture **(c)**. The four clonotypes selected for further characterization in this study are highlighted with a red polygon. From largest to smallest, the annotated clonotypes are: SK3D, SK5A, SK5B, and SK5G. **(d)** Dose-response curves for positive control antibody G11 binding to polyspecific targets (dsDNA, insulin, LPS) by ELISA. Black lines represent four-parameter logistic (4PL) regression fits. All values represent the mean of technical duplicates with background and blank subtraction. **e**, UMAP projection of tumour-draining lymph node (TDLN)-derived B cells annotated with B cell identity cluster. **f**, Dot plot showing differentially expressed canonical marker gene expression in each B cell population, annotated with the percentage of cells expressing each gene, compare to Fig. S6b. **g**, Scatterplot showing number of amino acid (AA) substitutions versus the imputed germline reference sequence for individual tumour- and TDLN-derived putative NMDAR-binding B cell clones (antigen specificity score >50%). **h**, Pie charts showing the distribution of B cell differentiation states in tumour- and TDLN-derived putative NMDAR-binding B cell clones (antigen specificity score >50%). **i**, ELISA results showing optical density (OD) values at serial dilutions for cell culture supernatant from HEK293S GnTI- cells transfected with expression plasmids encoding representative antibody sequences (SK10-3 and SK8-11). Control refers to supernatant from untransfected cells.
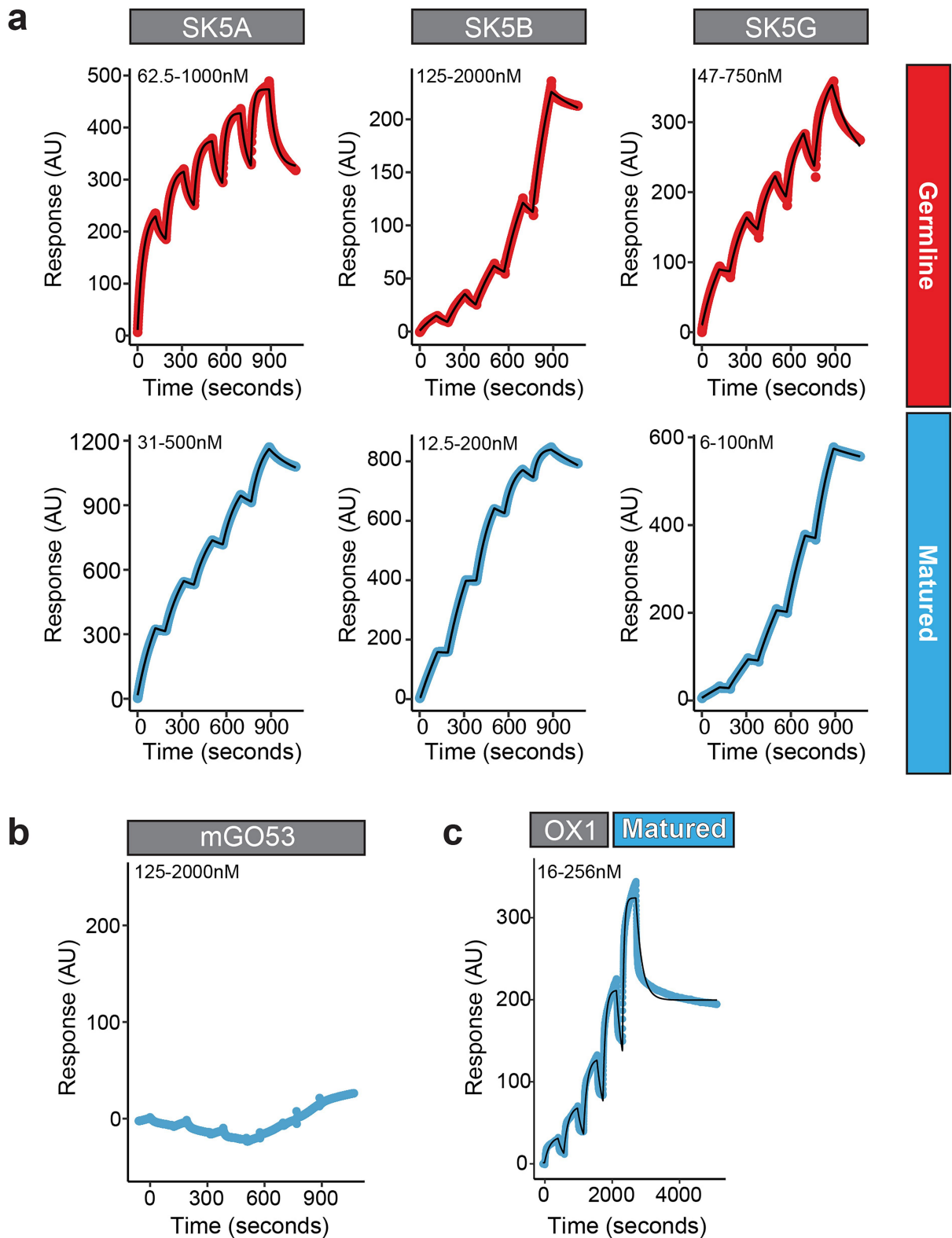
Extended Data Fig. 5 | related to Fig. 3: Binding kinetics of germline and matured anti-NMDAR antibodies. a-c, Single-cycle kinetics (SCK) surface plasmon resonance (SPR) traces for SK5A, SK5B, and SK5G germline and matured antibody sequences **(a)**, non-binding control mGO53 **(b)** and patient-derived antibody OX1-Matured **(c)**, annotated with the range of concentrations (reflecting two-fold serial dilutions) used in each assay. Model fit parameters are detailed in Table S2.

Extended Data Fig. 6 | See next page for caption.

Extended Data Fig. 6 | related to Fig. 4: Structural basis of antibody-NMDAR interactions. a, Schematic of GluN1-GluN2B NMDAR (PDB code 9arg) annotated with the ATD heteromer used for visualizations in the lower panel. R1 and R2 refer to the upper and lower lobes of the ATD, respectively. ATD, amino-terminal domain; LBD, ligand-binding domain; TMD, transmembrane domain. **b-c**, GluN1-GluN2B ATD heteromers annotated with the interaction surface for each germline **(b)** and matured **(c)** antibody as computed using the Surfaces package for Python. The interaction surface is coloured from black to white to indicate unfavourable to favourable amino acid interactions. **d**, Structural evidence of l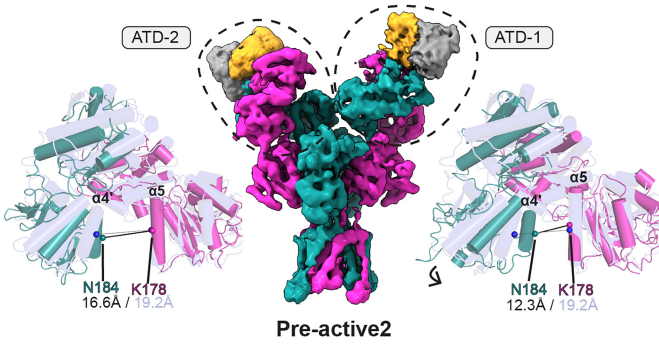ocal conformational changes that are correlated with affinity maturation in SK3D, SK5A, SK5B and SK5G clonotypes. Interacting residues are highlighted. For SK5B, the change in epitope from the GluN2B R2 lobe to the GluN1 R1 lobe during affinity maturation is shown. **f-g**, Left: Cryo-EM densities for OX1-Germline IgG **(e)** and OX1-Matured Fab **(f)** in complex with GluN1-GluN2B NMDARs. Note that there was clear cryo-EM density only for the Fab, but not Fc regions. ATD, amino-terminal domain; LBD, ligand-binding domain; TMD, transmembrane domain. Right: A focused view of the interaction interface between the GluN1-GluN2B NMDAR and each antibody. These models were built using locally refined maps of the interaction interface. Dashed lines indicate polar interactions.
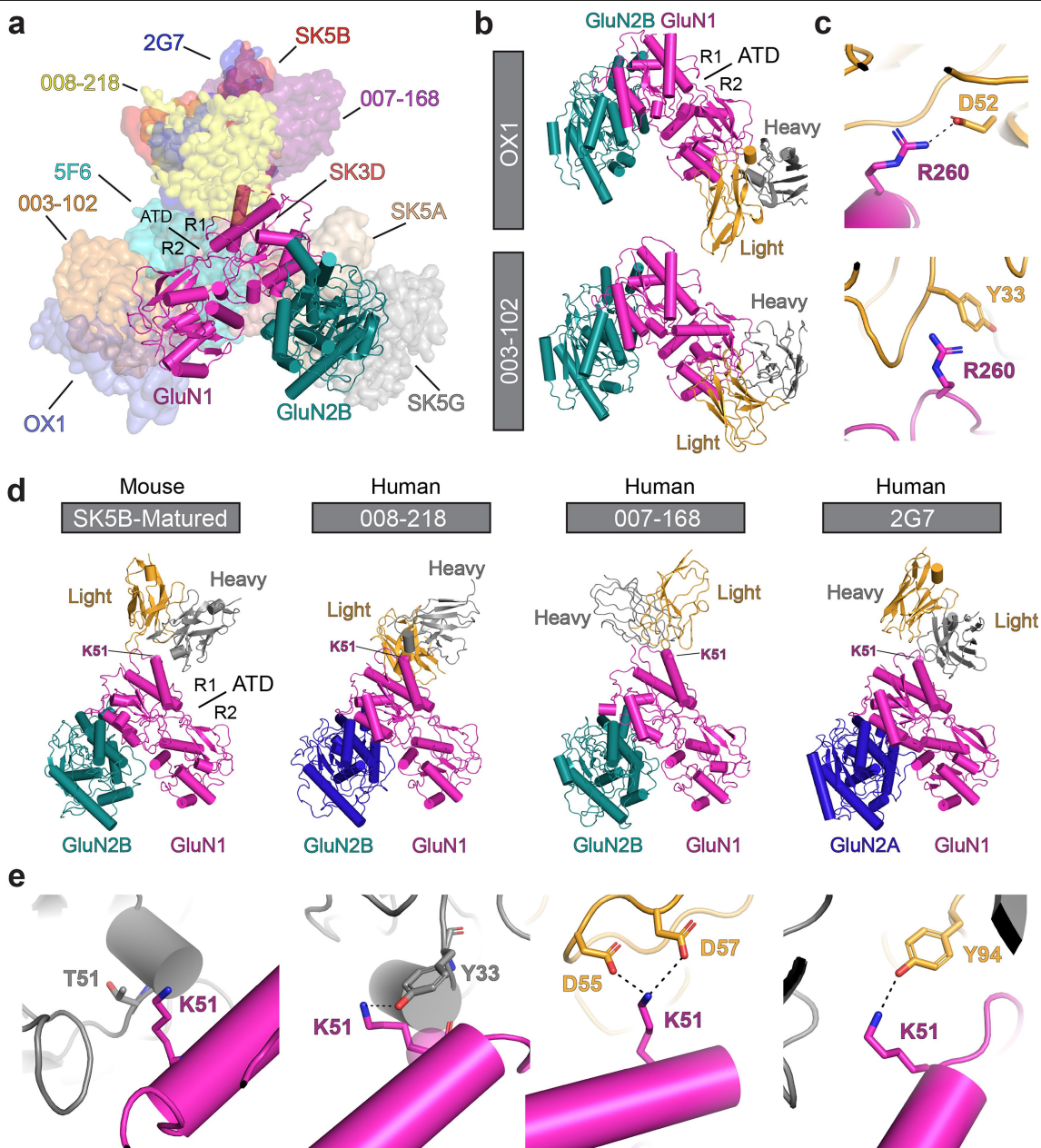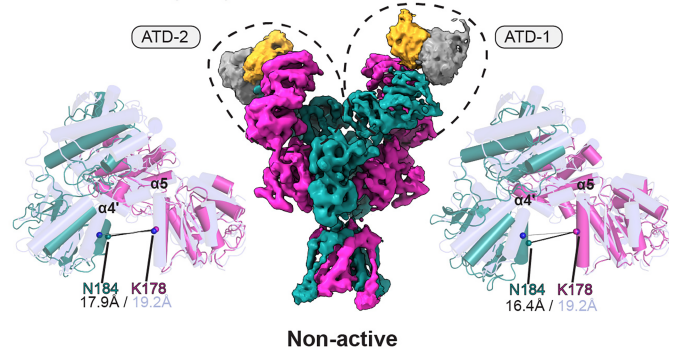
Extended Data Fig. 7 | related to Fig. 4: Epitope convergence across mouse- and patient-derived anti-NMDAR antibodies. a, Summary of all described NMDAR-antibody complexes. Each Fab region is displayed as a volume bound to GluN1 and/or GluN2B ATDs. Previously reported structures: 008-218 (8vun), 003-102 (8vuy), 007-168 (8vus), 2G7 (8jj1) and 5F6 (8jiz). **b-c**, Common epitopes observed for two patient-derived antibodies: OX1 (this study) and 003-102 (8vuy) binding to the GluN1-ATD R2 lobe. Both an overall view **(b)** and a focused view of the interaction interface centred on GluN1 R260 **(c)** are shown. **d-e**, Common epitopes observed for SK5B-Matured (mouse, this study) and three patient-isolated antibodies: 007-168 (8vuv, bound to GluN1-GluN2B), 008-218 (8vun, bound to GluN1-GluN2A) and 2G7 (8jj1, bound to GluN1-GluN2A) to the GluN1-ATD R1 lobe. Both an overall view **(a)** and a focused view of the interaction interface centred on GluN1 K51 **(b)** are shown. Interacting residues are highlighted, and polar interactions are indicated with dashed lines.
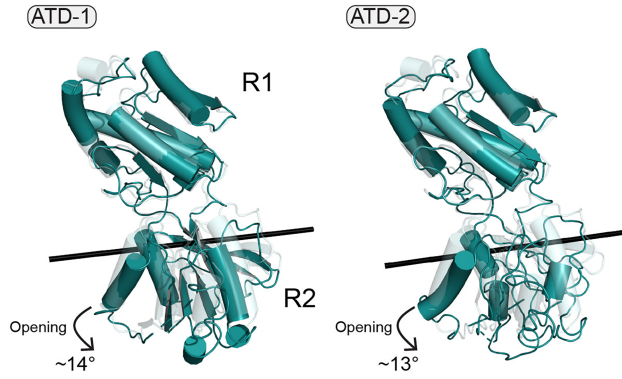
a **SK5A-Matured (Gly/Glut) - Minor**
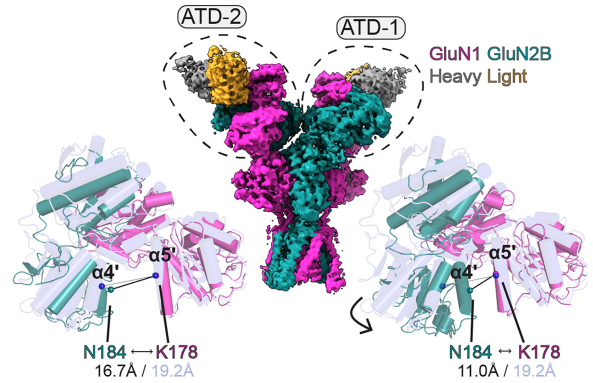Non-active (9arf)

ATD-2   ATD-1

α4'   α5   α4'   α5

N184   K178   N184   K178
16.6Å / 19.2Å   12.3Å / 19.2Å

Pre-active2

b **SK5A-Matured (Gly/Glut) - Major**
Non-active (9arf)

ATD-2   ATD-1

α4'   α5   α4'   α5

N184   K178   N184   K178
17.9Å / 19.2Å   16.4Å / 19.2Å

Non-active

c GluN2B: SK3D-Matured
GluN2B: L689/glu (6wi0)

ATD-1   ATD-2

R1

R2

Opening   Opening
~14°   ~13°

d SK3D-Germline
Non-active (9arf)

ATD-2   ATD-1

GluN1 GluN2B
Heavy Light

α4'   α5'   α4'   α5'

N184 ⟷ K178   N184 ↔ K178
16.7Å / 19.2Å   11.0Å / 19.2Å

e **SK3D-Germline (Gly/Glut)** - modified classification approach

10 classes (filter 25Å)

D1

3.16Å

| Class 1 | Class 6 |
| 15.5% | 9.3% |

| Class 3 | Class 9 |
| 10.0% | 11.2% |

0-bound
46%

| Class 0 | Class 5 | Class 8 |
| 8.3% | 8.0% | 7.9% |

| Class 2 | Class 4 | |
| 8.9% | 12.3% | |

1-bound
45.4%

Class 7
8.7%

2-bound
8.7%
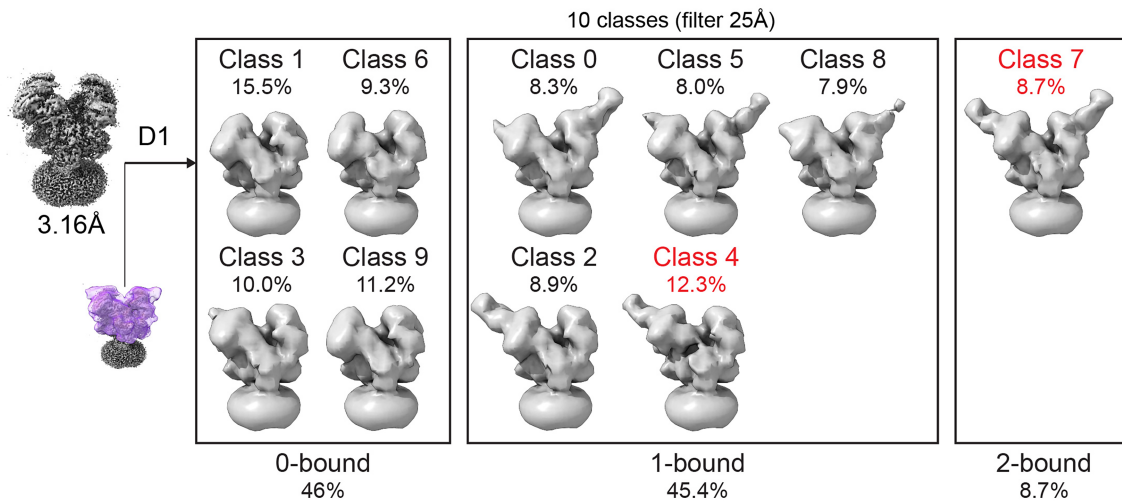
f **3D classes --> ATD-1 α4'–α5 distances**

Non-active

Pre-active2

α4'–α5 distance

Number of IgG molecules bound
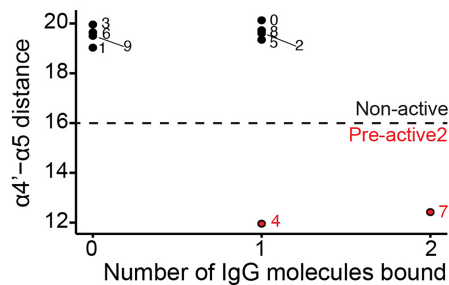
Extended Data Fig. 8 | See next page for caption.

Article

Extended Data Fig. 8 | related to Fig. 5: Antibody-induced conformational changes in NMDAR amino-terminal domains. a, SK5A-Matured Minor class: Asymmetric conformational rearrangement (pre-active2) of GluN1 and GluN2B amino-terminal domain (ATD) sub-units induced by binding of SK5A-Matured in the presence of agonists, annotated with the distance between GluN2B N184 (α4′) and GluN1 K178 (α5). b, SK5A-Matured Major class: No evidence of conformational rearrangement in either ATD heteromer versus the non-active state (PDB code 9arf) with binding of SK5A-Matured in the presence of agonists.

c, Visualization of GluN2B ATD-1 and ATD-2 clamshell conformations for SK3D-Matured (IgG) in complex with GluN1-GluN2B, as compared to the closed-clamshell conformation (PDB: 6wi0). d, Asymmetric conformational rearrangement (pre-active2) induced by binding of SK3D-Germline, annotated with the distance between GluN2B N184 (α4′) and GluN1 K178 (α5). e-f, Schematic summarizing the 3D classification of SK3D-Germline (e) and the resulting α4′- α5 distances for a model built using an ATD-1-focused refinement of each class (f).
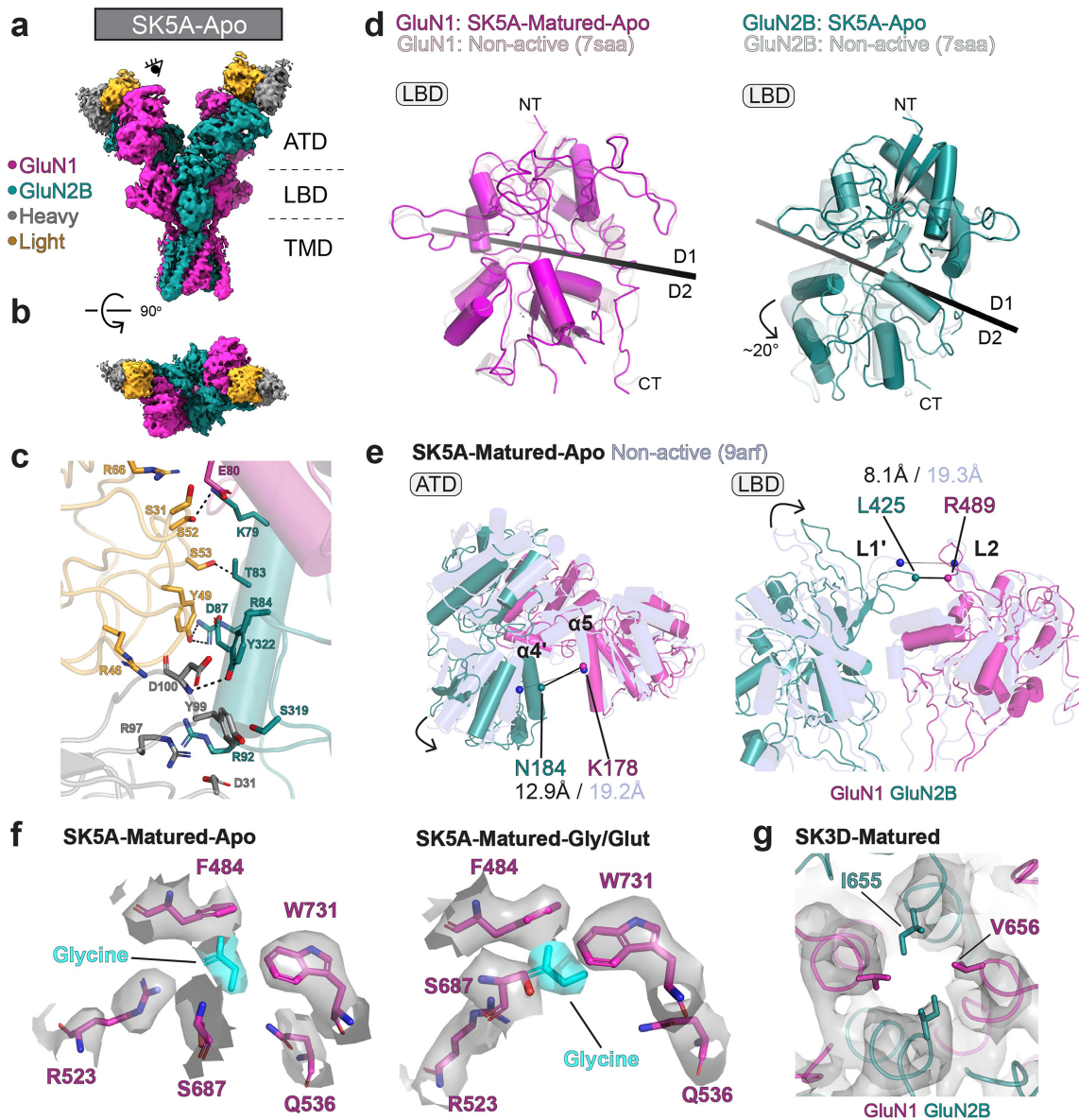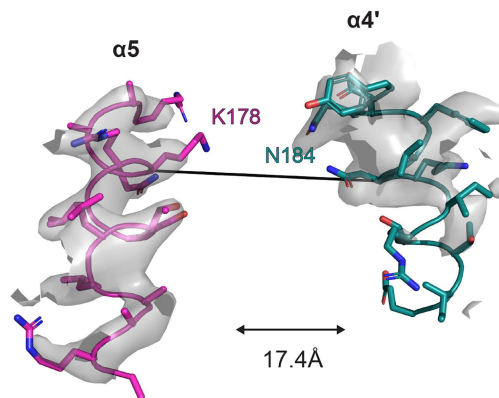
Extended Data Fig. 9 | related to Fig. 5: Cryo-EM structure of SK5A bound to NMDARs in the apo state. a-b, Cryo-EM densities for SK5A (IgG) in complex with GluN1-GluN2B NMDARs, in the absence of glycine and glutamate. Note that there was clear cryo-EM density only for the Fab, but not Fc regions. ATD, amino-terminal domain; LBD, ligand-binding domain; TMD, transmembrane domain. **c**, A focused view of the interaction interface between the GluN1-GluN2B NMDAR and SK5A, showing residue-level interactions between IgG variable regions and NMDARs annotated with amino acid positions. The constant regions of each IgG were not clearly visualized and so were omitted for clarity. Dashed lines indicate polar interactions. **d**, Visualization of the GluN1 and GluN2B LBD clamshell conformations for SK5A-Matured (IgG) in complex with

GluN1-GluN2B, in the absence of glycine and glutamate, as compared to the non-active conformation (PDB: 7saa). **e**, Conformational state of the ligand-binding domain (LBD) for SK5A-Matured (in the absence of glycine and glutamate) in complex with NMDARs annotated with GluN2B L425 (L1') – GluN1 R489 (L2) distances as compared to the non-active conformation (PDB code 9arf). **f**, Representative views of cryo-EM density annotated with interacting amino acids at the GluN1 glycine binding site for SK5A with and without agonists. Cryo-EM density is derived from local refinements (C2) focused on the LBD. Contour level shown is 0.15. **g**, Representative view of SK3D-Matured cryo-EM density annotated with a top-view model of the closed channel gate (9arf) with hydrophobic gate residues indicated. Contour level shown is 0.08.
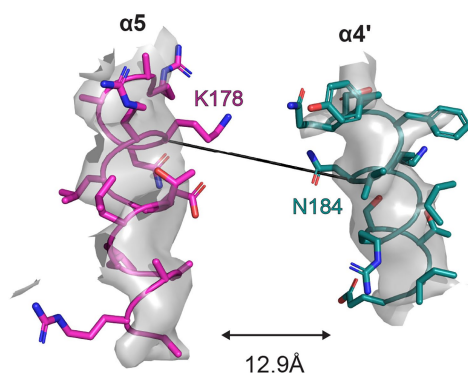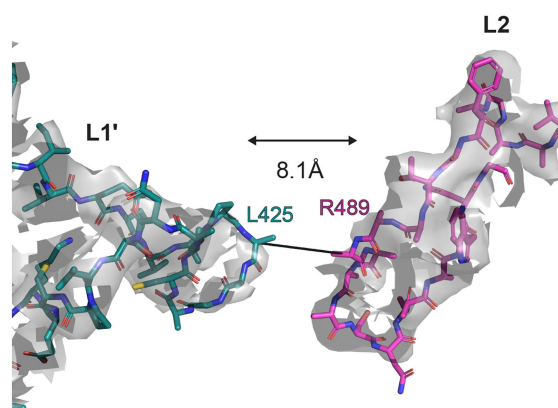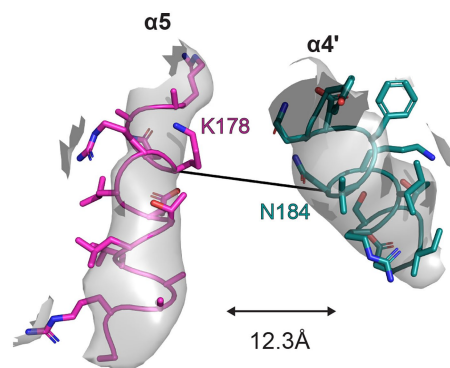
a SK3D-Matured: ATD-1
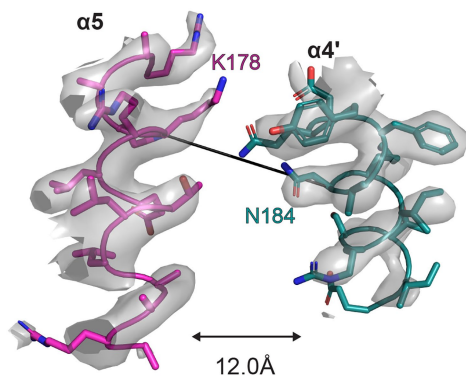
b SK3D-Matured: ATD-2
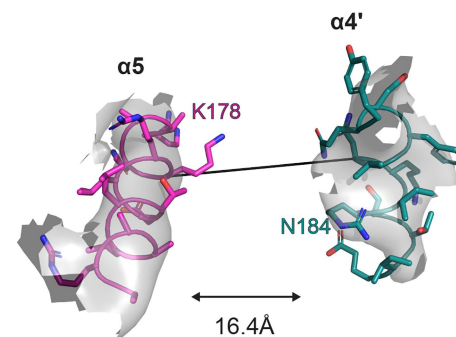
c SK5A-Matured-Apo: ATD

d SK5A-Matured-Apo: LBD

e SK5A-Matured: Minor/ATD-1

f SK5A-Matured: Major/ATD-1

Extended Data Fig. 10 | related to Fig. 5: Cryo-EM density validation of structural measurements. a-f, Representative views of the labelled cryo-EM density annotated with the underlying model in the regions where α4′- α5 and L1′-L2 distances were measured. **(a)** SK3D-Matured ATD-1. Contour level was 0.15 (GluN1) and 0.11 (GluN2B). **(b)** SK3D-Matured ATD-2. Contour levels were 0.15 (GluN1) and 0.09 (GluN2B). **(c)** SK5A-Matured -Apo ATD. Contour levels were 0.09. **(d)** SK5A-Matured-Apo LBD. Contour levels were 0.07. **(e)** SK5A-Matured ATD-1 Minor. Contour levels were 0.14 (GluN1) and 0.13 (GluN2B). **(f)** SK5A-Matured ATD-1 Major. Contour levels were 0.14 (GluN1) and 0.13 (GluN2B). Variable local density in α4 helix regions reflects structural flexibility and introduces a degree of measurement uncertainty in distance calculations.

a

IgG

Agonist

I_b

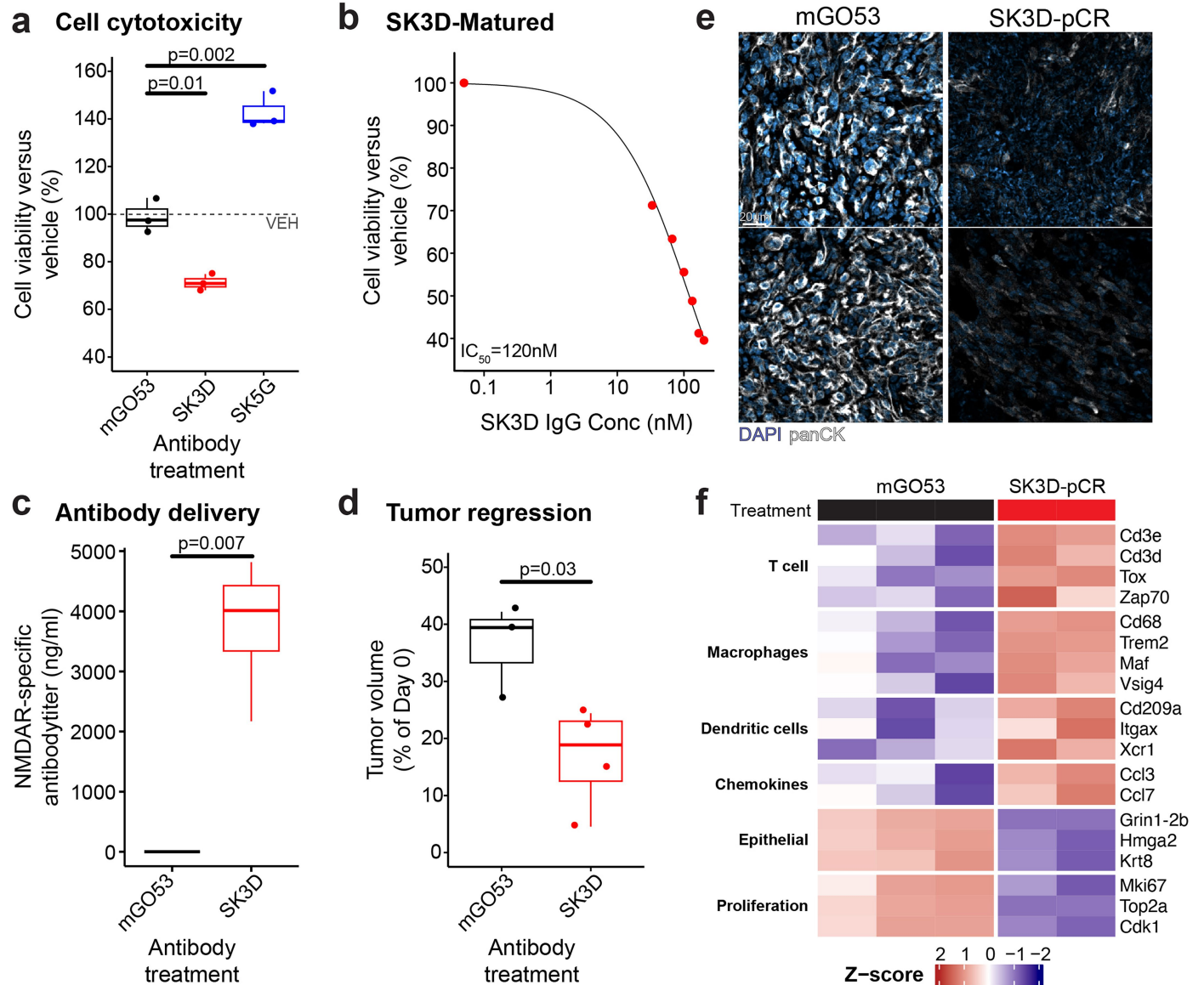I_0

$$\text{Effect (\%)} = \frac{I - I_b}{I_0 - I_b} \times 100$$

Current

Time

I

b SK5A-Matured

SK5A-Matured

Agonist

30s

I/I_0 (%)

300

200

100

*

***

***

0   4   12   37   111   333

IgG Conc (nM)

c SK5B-Matured

SK5B-Matured

Agonist

I/I_0 (%)

300

200

100

0   4   12   37   111   333

IgG Conc (nM)

d mGO53 - control

mGO53

Agonist

30s

e

I/I_0 (%)

300

200

100

0

SK5A

SK3D

SK5B

SK5G

r^2=0.98

p=0.0059

10.0 12.5 15.0 17.5 20.0 22.5

α4'−α5 distance (Å)
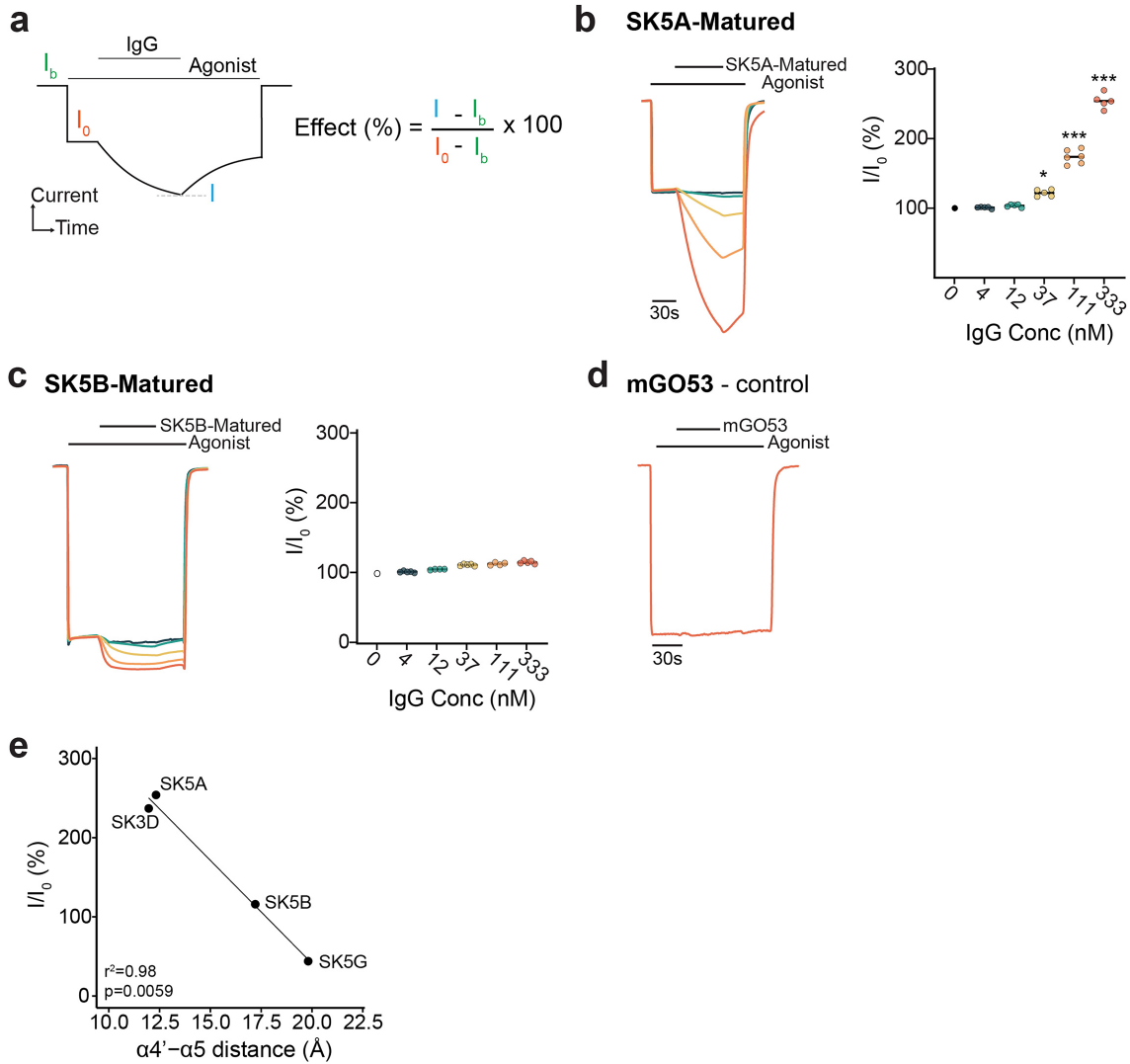
Extended Data Fig. 11 | related to Fig. 5: Electrophysiological characterization of antibody-induced NMDAR modulation. a, Schematic summarizing estimation of antibody effect, as a function of the baseline holding current before agonist addition (I_b), the current after agonist addition (I_0), and the current after one minute of IgG treatment in the presence of agonists (I). **b-d**, Modulation of glycine/glutamate-induced currents measured by TEVC following treatment with SK5A-Matured **(b)**, SK5B-Matured **(c)**, and 333 nM of non-binding control mGO53 **(d)**. Left panel – representative TEVC traces normalized to baseline current amplitude. Right panel – IgG-induced percentage change in current amplitude (I/I_0) (see Fig. S17a) at different IgG concentrations. Oocytes were pre-treated with an isotype control antibody (mGO53) to minimize any non-specific effects of IgG binding. P-values refer to one-sample t-tests with the null hypothesis that the mean ratio is 1. **e**, Scatter plot of IgG-induced percentage change in current amplitude (I/I_0) as a function of the α4'- α5 in each matured antibody model, annotated with the correlation coefficient. For antibodies inducing the pre-active2 conformation (SK3D and SK5A), the lowest α4'- α5 distance was selected. *, p < 0.05; ***,p < 0.001.

a Cell cytotoxicity

b SK3D-Matured

c Antibody delivery

d Tumor regression

e mGO53 / SK3D-pCR

f

Extended Data Fig. 12 | related to Fig. 5: Therapeutic efficacy of anti-NMDAR antibodies in vivo. a, Cell viability of DOX-treated 4T1-NMDAR cells incubated with 33 nM mGO53, SK3D or SK5G IgG for 24 h, relative to VEH. Data reflect biological triplicates. **b**, Dose-response curve for SK3D-induced cytotoxicity, annotated with the calculated IC_{50} value. **c**, Plasma NMDAR-specific antibody titres in B-cell deficient BALBc (IghJ-/-) mice treated with mGO53 or SK3D mIgG2a for 7 days, as measured by ELISA. **d**, Relative tumour volume change in B-cell deficient BALBc (IghJ-/-) mice treated with mGO53 or

SK3D mIgG2a for 7 days. **e**, Representative immunofluorescence (IF) for panCK in mGO53-treated mice (left column) and SK3D-treated mice showing pathological complete response (pCR). **f**, Heatmap showing relative expression (Z-scored) of immune cell and epithelial marker genes determined by bulk RNA-seq in mGO53-treated tumours versus SK3D-treated tumours with pathological complete response (pCR). All genes were differentially expressed between groups at FDR < 0.05.
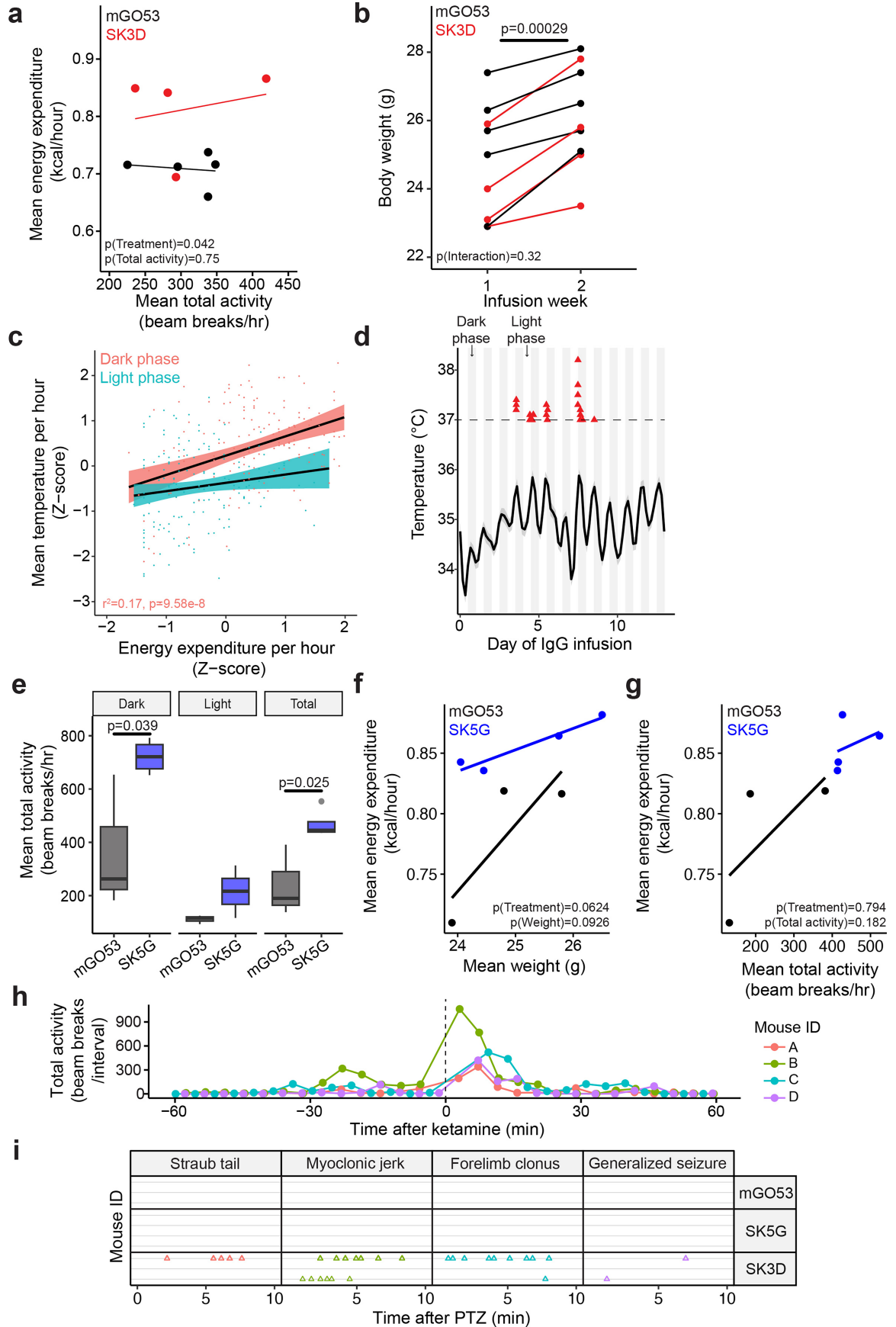
Extended Data Fig. 13 | See next page for caption.

Extended Data Fig. 13 | related to Fig. 5: Physiological and behavioural monitoring of mice during anti-NMDAR antibody treatment. a, Scatter plot of mean energy expenditure per hour during the SK3D study as a function of the mean activity per hour, annotated with the results of ANCOVA modelling. **b**, Paired plot showing the body weight of each mouse during the SK3D study. P-value refers to paired t-test. **c**, Scatter plot showing the mean hourly temperature (Z-scored) measured by a subcutaneous probe in one mouse as a function of the energy expenditure per hour (Z-scored). **d**, Continuous temperature tracing as measured by a subcutaneous probe in one mouse during SK3D IgG infusion, annotated with temperature spikes above 37 °C, as well as the dark and light phases (dark and light shading). **e**, Box plots showing the distribution of mean total activity (beam breaks) per hour in mGO53- and SK5G-treated mice, stratified by dark and light phases. **f-g**, Scatter plots of mean energy expenditure per hour during the study as a function of mean body weight **(f)** or mean total activity (beam breaks) per hour **(g)**, annotated with the results of ANCOVA modelling. **h**, Time course showing the effect of a single 0.5 mg intraperitoneal (IP) dose of ketamine, administered at time 0 (indicated by dashed vertical line), on the recorded number of beam breaks per 4-minute interval in four healthy female mice in metabolic cages. Individual mice are colour-coded. **i**, Timeline showing specific seizure events (independent cohort vs. Fig. 6) during the first 10 min after mice were intraperitoneally injected with 0.5 mg of pentylenetetrazole (PTZ, GABA receptor antagonist). Each triangle represents an observed seizure event.
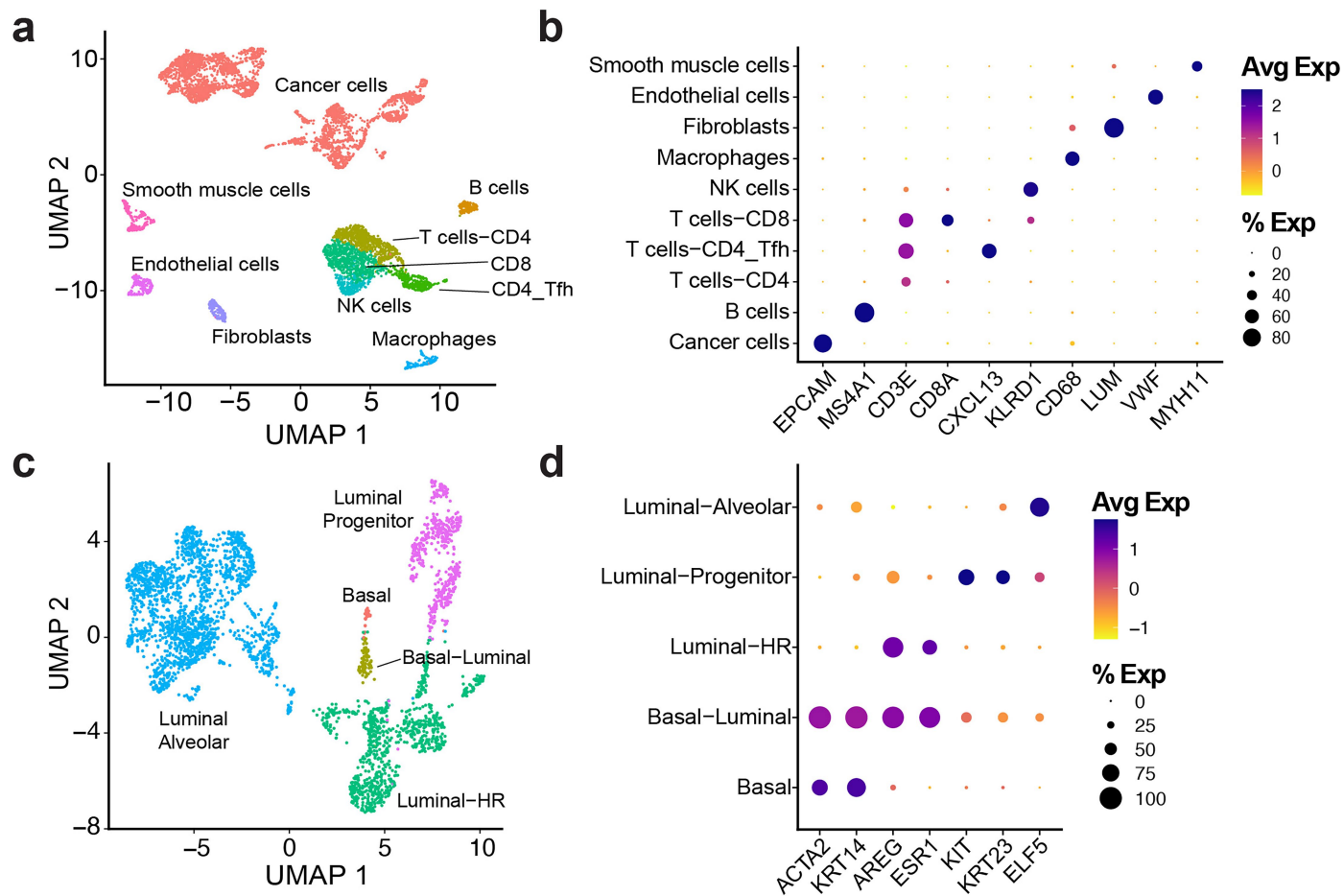
Extended Data Fig. 14 | related to Fig. 5: Single-cell profiling of NMDAR expression in human breast cancer. a, UMAP projection of scRNA-seq data from 6,343 cells isolated from patient N38 tumour, annotated by cell type. **b**, Dot plot showing the scaled gene expression (point colour) and percentage of expressing cells (point size) for canonical marker genes across cell types identified in panel d. **c**, UMAP projection of *EPCAM*-positive cancer cell clusters from panel d, annotated by distinct breast cancer epithelial cell differentiation states, including basal (*ACTA2* + *KRT14* +), luminal-HR (*ESR1* + *AREG* +), luminal-alveolar (*ELF5* +), luminal-progenitor (*KIT* + *KRT23* +), and basal-luminal intermediate (*ACTA2* + *ESR1* +) states. **d**, Dot plot showing the scaled gene expression (point colour) and percentage of expressing cells (point size) for NMDAR subunit genes (GRIN1, GRIN2B) alongside canonical markers of the epithelial differentiation states defined in panel f.
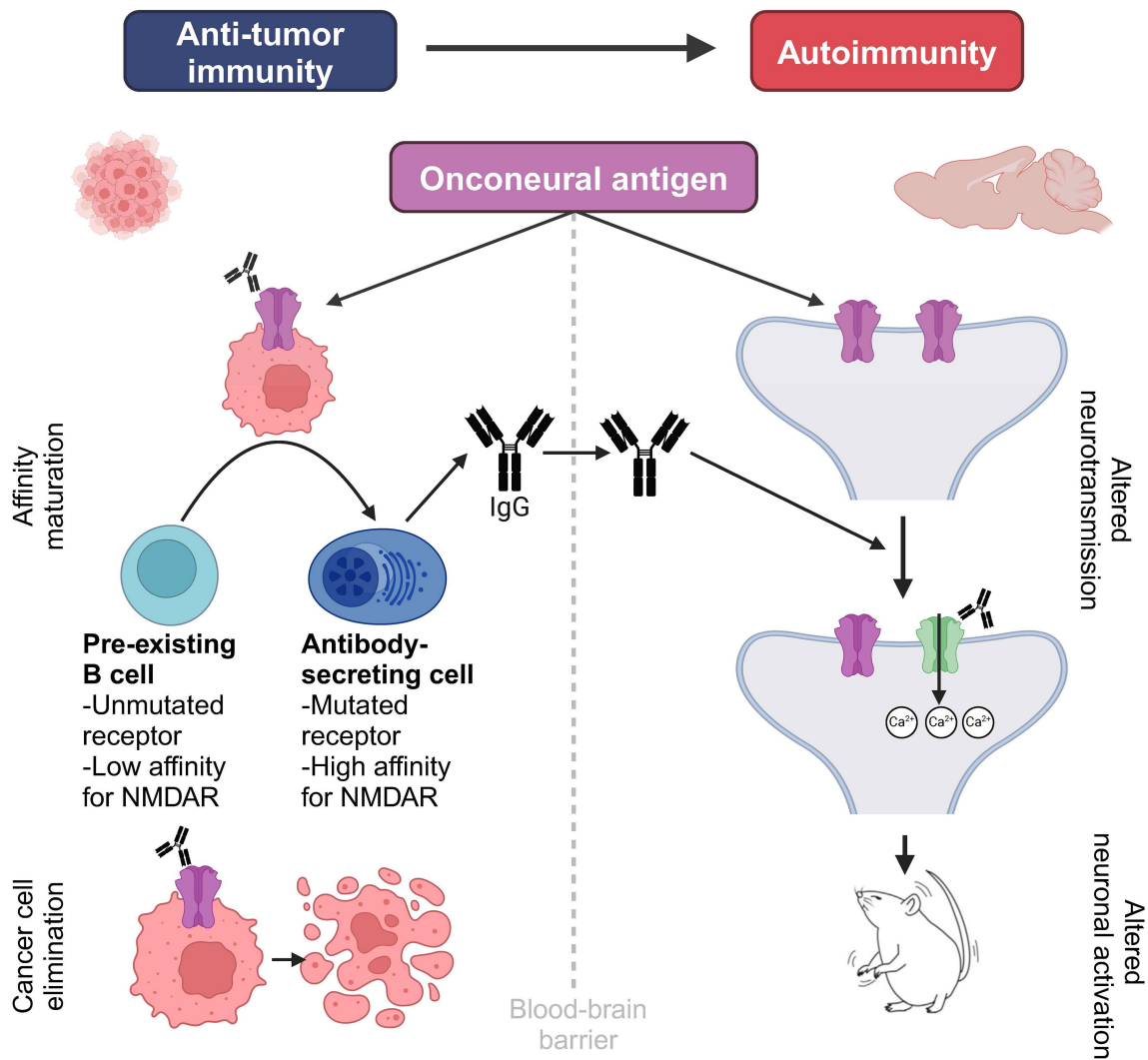
Extended Data Fig. 15 | Graphical abstract. Aberrant intratumoral expression of proteins normally restricted to the central nervous system (onconeural antigens), such as NMDARs, is sufficient to recruit and induce maturation of pre-existing B cells with unmutated germline-configuration receptors that have low baseline NMDAR affinity. Affinity maturation results in the production of high-affinity NMDAR-binding antibodies, which constrain tumour growth but, on crossing the blood-brain barrier, modulate NMDAR function on binding. Antibody-induced receptor modulation leads to disordered neuronal activation, manifesting as a reduced seizure threshold in mice. The diagram was created using BioRender.

nature portfolio

Corresponding author(s): Tobias Janowitz and Hiro Furukawa

Last updated by author(s): 09/10/2025

Reporting Summary

Nature Portfolio wishes to improve the reproducibility of the work that we publish. This form provides structure for consistency and transparency in reporting. For further information on Nature Portfolio policies, see our Editorial Policies and the Editorial Policy Checklist.

Statistics

For all statistical analyses, confirm that the following items are present in the figure legend, table legend, main text, or Methods section.

n/a	Confirmed	
☐	☒	The exact sample size (*n*) for each experimental group/condition, given as a discrete number and unit of measurement
☐	☒	A statement on whether measurements were taken from distinct samples or whether the same sample was measured repeatedly
☐	☒	The statistical test(s) used AND whether they are one- or two-sided *Only common tests should be described solely by name; describe more complex techniques in the Methods section.*
☐	☒	A description of all covariates tested
☐	☒	A description of any assumptions or corrections, such as tests of normality and adjustment for multiple comparisons
☐	☒	A full description of the statistical parameters including central tendency (e.g. means) or other basic estimates (e.g. regression coefficient) AND variation (e.g. standard deviation) or associated estimates of uncertainty (e.g. confidence intervals)
☐	☒	For null hypothesis testing, the test statistic (e.g. *F*, *t*, *r*) with confidence intervals, effect sizes, degrees of freedom and *P* value noted *Give P values as exact values whenever suitable.*
☒	☐	For Bayesian analysis, information on the choice of priors and Markov chain Monte Carlo settings
☒	☐	For hierarchical and complex designs, identification of the appropriate level for tests and full reporting of outcomes
☐	☒	Estimates of effect sizes (e.g. Cohen's *d*, Pearson's *r*), indicating how they were calculated

Our web collection on statistics for biologists contains articles on many of the points above.

Software and code

Policy information about availability of computer code

Data collection	Electrophysiological data for NMDAR currents were acquired using PatchMaster (HEKA). Cryo-EM data was collected using Thermo Fisher Scientific EPU software (version 2.10.0.5). Surface plasmon resonance data was acquired using the Cytiva Biacore Evaluation Software. Metabolic cage data was recorded using Oxymax for Windows (version 5.71). Flow cytometry data was acquired using Sony Cell Sorter, BD FACSDiva and Guava inCyte software.
Data analysis	For flow cytometry data, FlowJo (v10) was used for gating and analysis. Scanned histological sections were analyzed using ImageJ (v1.51) and QuPath (v0.5.1). Cryo-EM data was processed using WARP (v2), Relion (v4), and cryoSPARC (v3.2 to 4.6, reflecting release of updated versions during the study). Final structural models were generated in WinCoot (v0.9.8) and refined in PHENIX (v1.20.1), and figures were created using UCSF ChimeraX (v1.4) and PyMOL (v2.5.5). B-cell receptor (BCR) phylogenetic reconstructions were performed using enclone (v0.5). Electrophysiology data was analyzed using Origin (v8, OriginLab Corp). Downstream data analysis was performed using R (v4.4.0). In particular, SPR data was analyzed using the anabel package (v3.0.1) for R. Gene expression data was analyzed using the edgeR (v4) package for R. Code notebooks comprising R scripts and resource files required to reproduce RNA-seq, single-cell and Visium HD analyses are available from Github and have been deposited in Mendeley Data (10.17632/3d7wfzbg2t.1).

For manuscripts utilizing custom algorithms or software that are central to the research but not yet described in published literature, software must be made available to editors and reviewers. We strongly encourage code deposition in a community repository (e.g. GitHub). See the Nature Portfolio guidelines for submitting code & software for further information.

Data

All manuscripts must include a [data availability statement](#). This statement should provide the following information, where applicable:

- Accession codes, unique identifiers, or web links for publicly available datasets
- A description of any restrictions on data availability
- For clinical datasets or third party data, please ensure that the statement adheres to our [policy](#)

New datasets generated: Cryo-EM maps and structural models (containing antibody amino acid sequences) will be deposited in the Electron Microscopy Data Bank (EMDB) and Protein Data Bank (PDB), respectively, prior to publication. The plasmid sequence for the PB-TRE-Grin construct was deposited at GenBank under accession number XXXX. Raw bulk RNA sequencing data have been deposited in NCBI Sequence Read Archive (SRA) under project ID PRJNA1370999. Raw mouse-derived single-cell RNA sequencing data have been deposited in NCBI SRA under project ID PRJNA1371359. Raw human-derived single-cell RNA sequencing data have been deposited in the European Genome-phenome Archive (EGA) under accession number XXXX – this data is stored under restricted access to protect patient privacy. Mouse- and human-derived 10X Genomics output data directories (single-cell RNA sequencing, Visium HD), corresponding processed Seurat matrices and configuration files for 'cellranger multi' have been deposited at Mendeley Data (10.17632/mgb9r3tgz8.1). Processed count matrices have been deposited at Mendeley Data (10.17632/5tyv4xggpc.1).

Publicly available datasets: Processed scRNA-seq data from published human thymus samples is available from CELLxGENE, while raw data is available from ENA with study accession PRJEB77091. Breast cancer clinicopathological, protein array (where available) and processed RNA sequencing data is available from cBioPortal for TCGA-BRCA and METABRIC. Count-level bulk RNA sequencing data for TCGA-BRCA is available from UCSC Xena. Published cryo-EM models referenced in this paper are available from PDB with accession codes 6wi0, 7saa, 9arf, 8vuv, 8vun, 8vuy, 8vus, 8jj1, 8jiz.

Research involving human participants, their data, or biological material

Reporting on sex and gender	All patients recruited for this study were assigned female sex at birth, reflecting the epidemiology of TNBC and anti-NMDAR encephalitis. Gender identity was not recorded separately and was not a variable in study design or analysis.
Reporting on race, ethnicity, or other socially relevant groupings	Race and ethnicity were not reported for the Northwell cohort and were unavailable for vendor-supplied specimens. No analyses requiring social groupings were performed.
Population characteristics	The primary TNBC discovery cohort consisted of forty-eight women treated at Northwell Health with an age range of 26-89. Peripheral blood was drawn intra-operatively and processed within two hours. Fresh tumour was available for a subset of cases when excess clinical tissue permitted, minced, and viably cryopreserved at −80 °C. Five additional matched plasma–tumour pairs were purchased from BioChain (age range 36-70), and one frozen tumour section (patient FR001D525) was obtained from Origene for Visium HD spatial transcriptomics. To define the physiological range of anti-NMDAR antibody titres, plasma from twenty-three healthy women aged 18–30 years was procured from BioIVT under its IRB protocol as controls to benchmark antibody titers observed in the patient cohorts. Finally, PBMCs for B-cell cloning were collected from a 28-year-old woman with confirmed ANRE who had consented to research participation at the University of Oxford. All TNBC tumors satisfied standard immunohistochemical definitions of triple-negative disease (estrogen-receptor and progesterone-receptor expression each < 1 % of tumor nuclei; HER2 score 0–1 + or 2 + with negative fluorescence in situ hybridization).
Recruitment	Northwell patients were recruited during surgical scheduling visits and enrolled if they were ≥ 18 years old, had stage I–III TNBC, and could provide informed consent. No exclusions were made on the basis of race, ethnicity, socioeconomic status, or comorbidity. Cases were selected based on available sample material, with investigators blinded to most clinicopathological and demographic information at selection, minimizing selection bias. Potential self-selection bias exists as participation required attendance at surgical visits and consent; however, this is unlikely to substantially impact results given the blinded selection process and absence of other exclusion criteria. Vendor cohorts were recruited independently by BioChain and Origene under broad-consent protocols that permit anonymized research use of residual biospecimens; the authors played no role in that recruitment. Healthy control plasma donors were enrolled by BioIVT through its established volunteer program. The ANRE participant was identified on the basis of a confirmed diagnosis of anti-NMDAR encephalitis through a UK observational study of autoimmune encephalitis and contributed a one-time blood sample.
Ethics oversight	Human-subject oversight was provided by the Northwell Health Institutional Review Board (IRB 20-0150) for the prospective TNBC cohort and the South Central-Oxford A Research Ethics Committee (REC16/YH/0013) for the ANRE study. Vendor-procured specimens received IRB approvals from their respective institutions, as was verified by each vendor. The authors affirm that all human research was performed in accordance with the relevant guidelines and regulations, and that informed consent was obtained as described above.

Note that full information on the approval of the study protocol must also be provided in the manuscript.

Field-specific reporting

Please select the one below that is the best fit for your research. If you are not sure, read the appropriate sections before making your selection.

☒ Life sciences ☐ Behavioural & social sciences ☐ Ecological, evolutionary & environmental sciences

For a reference copy of the document with all sections, see nature.com/documents/nr-reporting-summary-flat.pdf

Life sciences study design

All studies must disclose on these points even when the disclosure is negative.

Sample size	For cryo-EM experiments, the dataset size is primarily determined by microscope availability and so this could not be pre-determined. For electrophysiology experiments, only healthy oocytes were studied. Healthy oocytes were defined by a clear spherical shape with distinguishable animal and vegetal hemisphere, as well as evident currents induced by glycine and glutamate. Electrophysiological data collection for each antibody was measured using at least five NMDAR-expressing oocytes. No formal sample size calculation was performed; this sample size is consistent with standard practice in Xenopus oocyte electrophysiology studies where technical variability is low and n=5 is typically sufficient to detect biologically meaningful differences in receptor function. For surface plasmon resonance experiments, each antibody-receptor pair dataset reflects a single data collection. No replicate experiments were performed as single-cycle kinetics methodology generates binding data across multiple analyte concentrations within a single run, with each concentration point contributing to the kinetic fit. This approach is standard for SPR kinetic analysis (see PMID 16337141) and provides robust determination of binding parameters. For mouse experiments, the sample size was generally predetermined according to the type of experiment based on common practice. For B cell isolation experiments, tumors from at least five mice were pooled together to ensure we captured a representative sample of tumor-infiltrating B cells and to obtain sufficient cell numbers for downstream analysis.. For intracerebroventricular antibody infusion experiments to detect seizure thresholds, we estimated that a sample size of 20 animals (10 per group) would be required, based on the power calculation assuming a prevalence of any seizure of 5% in the MGO53-treated group and 60% in the SK3D-treated group, with an alpha of 5% and power of 80%. For intracerebroventricular antibody infusion experiments to detect differences in energy expenditure, we estimated that a sample size of 8 animals (4 per group) would be required. This is based on a power calculation assuming a mean energy expenditure of 0.6 kcal/hour (SD 0.4) in the control group, doubling to 1.2 kcal/hour in the SK3D-treated group, with an alpha of 5% and a power of 80%. For tumor treatment experiments in B-cell deficient mice, a sample size of 4 animals per group was used for this proof-of-principle study to demonstrate feasibility of the approach. For human sample experiments, all analyses were exploratory and no sample size calculation was performed.
Data exclusions	No outlier data points were manually excluded. For intracerebroventricular infusions, we deliberately included a C-terminal FLAG tag in SK3D IgG in order to exclude SK3D-treated mice where we could not detect clear hippocampal anti-FLAG staining on endpoint brain sections. There are multiple reasons why intracerebroventricular pumps can be blocked, including, but not limited to, mechanical blockage, infection, occlusion of the outflow point, and we believe this exclusion criteria substantially improves the power of our study to detect differences between groups. For cryo-EM analysis, no micrographs were excluded. For initial cryo-EM particle processing, particles were automatically excluded by multiple rounds of heterogenous refinement, using manually selected low-resolution volumes reflecting antibody-receptor complexes. For datasets where the proportion of bound particles was relatively low, antibody-bound 3D classes were manually selected.
Replication	All Western blot experiments were repeated at least three times. Histological stains including immunohistochemistry and RNAscope were performed on multiple tumor sections and representative images were selected for inclusion in the manuscript. B cell isolation (from tumors and from tumor-draining lymph nodes) and sequencing was performed on two separate occasions with independent cohorts of pooled mice, with NMDAR-binding B cell receptors isolated from both cohorts. For the structural experiments, protein expression of antibodies and NMDA proteins was successfully reproduced at least three times. Cryo-EM data collection for each antibody-receptor complex was generally performed in a single 24 hour period. In light of the very low proportion of bound particles in the SK5B-Germline dataset, this was repeated on two separate occasions. The underlying data for the seizure induction paradigm (Fig 5i) incorporates the results of three independent biological replicates, with the results of each individual replicate confirming the association between SK3D treatment and seizure propensity. An additional replicate of SK3D-induced seizure potentiation is shown in Fig. S25e. Metabolic cage data showing altered energy expenditure was replicated across at least three independent cohorts. Spatial RNA profiling was performed on a single TNBC tumor section as an exploratory analysis.Experiments with the 4T1-NMDAR tumor model, including tumor growth kinetics, longitudinal antibody titers, and immunofluorescence of tumor sections, were performed across at least three independent cohorts with consistent findings. B cell isolation from the 4T1-NMDAR model was performed across four independent cohorts of mice. Electrophysiology dose-response experiments were performed using at least five independent oocytes per antibody at each concentration tested. In vitro cytotoxicity assays were performed with multiple replicates per concentration showing consistent dose-dependent effects, and the core findings were replicated in at least two experiments. Patient plasma ELISA analysis was performed once per sample across 53 TNBC patients, with immunofluorescence and flow cytometry validation performed on available tissue from a subset. All replication attempts were successful.
Randomization	For comparison between SK3D-, SK5G- and mGO53- treated mice, the mice were randomized into treatment groups after the initial PBS run-in. For tumor treatment experiments in B-cell deficient mice (Fig S23d), mice were randomized to receive either mGO53 or SK3D treatment groups at the time of DOX initiation.For 4T1-NMDAR tumor experiments comparing DOX versus vehicle treatment (Fig 2, Fig S4), mice were randomly allocated to treatment groups when tumors reached 100 mm³. For B cell isolation experiments, mice were not randomly allocated but were instead selected based on high antibody titers (≥500 ng/ml) measured by ELISA, as the experimental objective was to isolate and characterize NMDAR-reactive B cells from mice with robust humoral responses. For electrophysiology experiments, oocytes from the same batch were randomly assigned to different antibody treatment conditions to control for batch-to-batch variability in receptor expression levels. For human patient sample analysis, samples were analyzed from consecutively recruited patients meeting inclusion criteria (female,

histologically confirmed TNBC, plasma collected at surgery). This was an observational study and no experimental allocation was performed.
For the subset of patients selected for immunofluorescence and flow cytometry validation, samples were selected based on antibody titer status (Ab-High vs No-Ab) and tissue availability.
For cryo-EM resolution estimation and to avoid overfitting, cryo-EM particles were randomly split into two sets during 3D refinement.

Blinding

For the majority of experiments, the investigators were not blinded to group allocation as they performed both the experiment and analysis making blinding not possible. Seizure scoring was performed by investigators who were not blinded to treatment group but all sessions were video recorded, and scoring was verified by an independent review of all recordings with timestamped seizure episodes. The seizure events assessed - generalized tonic-clonic seizures, forelimb clonus, tail dorsiflexion, and myoclonic jerks - represent distinctive, stereotyped behaviors that can be unambiguously identified on video review, minimizing the potential for observer bias
Notably, blinding was performed specifically for detection of NMDAR expression in histopathological slides and initial electrophysiological screening of matured antibodies.
For cryo-EM particle processing blinding was not possible as careful analysis of all intermediate results is required to generate high-resolution reconstructions.
For tumor volume measurements in mouse experiments, investigators were not blinded to treatment allocation. However, tumor dimensions were measured using calipers according to a standardized protocol, and the quantitative nature of these measurements limits the potential for bias.
For experiments with automated or quantitative readouts - including ELISA, flow cytometry, surface plasmon resonance, metabolic cage measurements (energy expenditure, activity, body weight), and RNA/DNA sequencing, blinding was not relevant as data acquisition and primary analysis were performed using automated instruments and computational pipelines that eliminate subjective interpretation.
For patient sample analysis, investigators analyzing plasma ELISA results were not blinded to clinical information. However, the quantitative nature of ELISA measurements and the observational study design make blinding not applicable to this analysis.

Reporting for specific materials, systems and methods

We require information from authors about some types of materials, experimental systems and methods used in many studies. Here, indicate whether each material, system or method listed is relevant to your study. If you are not sure if a list item applies to your research, read the appropriate section before selecting a response.

Materials & experimental systems

n/a	Involved in the study
☐	☒ Antibodies
☐	☒ Eukaryotic cell lines
☒	☐ Palaeontology and archaeology
☐	☒ Animals and other organisms
☒	☐ Clinical data
☒	☐ Dual use research of concern
☒	☐ Plants

Methods

n/a	Involved in the study
☒	☐ ChIP-seq
☐	☒ Flow cytometry
☒	☐ MRI-based neuroimaging

Antibodies

Antibodies used

Anti-NMDAR: 003-102 (recombinantly purified in this study, originally isolated from a patient in PMID 27543972), IgG2 (purified from hybridoma supernatant in the study, originally isolated from an immunized mouse in PBMID 35177668). We further report a panel of mouse-derived NMDAR-binding antibody clonotypes (SK3D, SK5A, SK5B, SK5G) and one human-derived NMDAR-binding antibody clonotype (OX1), with amino acid sequences provided in PDB files.
For Western blotting: anti-GluN1 (Cell Signaling, 5704, dilution 1:1000), anti-GluN2B (Cell Signaling, 4207, dilution 1:1000).
For immunohistochemistry or immunofluorescence:
Anti-GluN1: custom as above, dilution 1:150 (fluorophore-conjugated)
Anti-GluN2B: custom as above, dilution 1:150 (fluorophore-conjugated) or 1:250 (HRP-conjugated)
Anti-CD3: BioLegend, 100209, dilution 1:100
Anti-panCK: Novus Biologicals, NBP1-48348, dilution 1:200
Anti-CD45R: Proteintech, CL555-65139, dilution 1:100
Anti-FLAG: Cell Signaling Technology, 14793, dilution 1:500

Validation

Anti-NMDAR: A cryo-EM structure for the specific binding of 003-102 IgG to the NMDAR GluN1-ATD has been previously reported (PDB 8VUR). A cryo-EM structure for the specific binding of IgG2 IgG to the NMDAR GluN2B-ATD has been previously reported (PDB 7TE9). We performed additional verification of these antibodies using brain sections as a positive control, shown as Supplementary Figure 2. For mouse-derived NMDAR-binding antibodies described in this study, we report cryo-EM, ELISA and SPR data confirming NMDAR binding. For Western blot antibodies, manufacturers provide validation data using rat and mouse brain lysates, confirming a specific band at the expected molecular weight.
Anti-CD3: Manufacturer provides validation data, specifically they show staining in the expected anatomical distribution of mouse spleen. We performed additional verification of this antibody using mouse spleen as a positive control.
Anti-panCK: Manufacturer provides validation data, specifically showing staining of epithelial cells (e.g. HeLa) by flow cytometry and immunohistochemistry in epithelial tissues (e.g. breast carcinoma), Western blot for lysate of epithelial cells showing bands at the expected molecular weight for keratins. We have further confirmed that the distribution of positive staining in our samples corresponds to epithelial tissue as visible by H&E stained sections.
Anti-CD45R: RA3-6B2 clone has been previously validated. We performed additional verification of this antibody using mouse spleen as a positive control, which confirmed staining in the expected anatomical distribution. The manufacturer specifically reports immunohistochemical staining in mouse tonsil and mouse spleen samples, showing a pattern of staining in the expected anatomical

distribution; they further report positive staining by flow cytometry in mouse splenocytes.
Anti-FLAG: Manufacturer provides validation data (Western blot). We performed additional verification of this antibody by staining mouse brain sections through the hippocampus with FLAG-tagged anti-GluN1 antibody, and using these stained sections as a positive control.

Eukaryotic cell lines

Policy information about cell lines and Sex and Gender in Research

Cell line source(s)	4T1 cells were obtained from the laboratory of M.Egeblad, which were originally obtained from ATCC. Sf9 insect cells were obtained from Thermo Fisher Scientific (11496015). HEK293S GnTI- cells were obtained from American Type Culture Collection (CRL-3022). Xenopus oocytes were harvested from the frogs raised in the animal facilities of Cold Spring Harbor Laboratory.
Authentication	None of the cell lines were authenicated after arrival in our lab except for 4T1, for which a previously identified mitochondrial mutation was verified in our hands.
Mycoplasma contamination	All cell lines were tested for Mycoplasma and confirmed negative prior to use in experiments.
Commonly misidentified lines (See ICLAC register)	No misidentified lines were used in this study.

Animals and other research organisms

Policy information about studies involving animals; ARRIVE guidelines recommended for reporting animal research, and Sex and Gender in Research

Laboratory animals	Female BALB/c, BALB/c-IghJ-KO (Cyagen C001345), C57BL/6 mice (8–14 weeks old) were used for tumor implantation and antibody infusion experiments. Wild-type mice were obtained from Jackson Laboratory. All animals were housed under specific pathogen-free conditions with a 12:12 light-dark cycle with controlled temperature (21-23°C) and humidity (40-60%) in animal facilities at Cold Spring Harbor Laboratory (CSHL). Mice were allowed to acclimatize for at least one week after arrival in the facility. Xenopus laevis oocytes were harvested from outbred adult female frogs raised in the animal facilities at CSHL. Adult female Xenopus laevis (wild-type, outbred stock), ~2–4 years old, obtained from Xenopus 1 Corp. (Dexter, MI, USA).
Wild animals	No wild animals were used in this study.
Reporting on sex	In consideration of the clinical context, where TNBC1, ANRE2,3, and their co-occurrence3,4 are predominantly observed in female patients, we have proactively chosen to model the underlying biology in female mice to maximize translational relevance. Furthermore, there are significant differences in symptom frequency and severity between male and female ANRE patients5,6. This sexual dimorphism may be partly explained by sex hormone activity as estrogen receptor signaling directly modulates NMDAR expression7,8 in the brain. 1. Gucalp, A. et al. Male breast cancer: a disease distinct from female breast cancer. Breast Cancer Res. Treat. 173, 37–48 (2019). 2. Dalmau, J. et al. An update on anti-NMDA receptor encephalitis for neurologists and psychiatrists: mechanisms and models. Lancet Neurology 18, 1045–1057 (2019). 3. Titulaer, M. J. et al. Treatment and prognostic factors for long-term outcome in patients with anti-NMDA receptor encephalitis: an observational cohort study. Lancet Neurology 12, 157–165 (2013). 4. Will, A. & Akalin, M. Paraneoplastic Limbic Encephalitis with NMDA Receptor (NR1) Antibodies in Breast Cancer (S08.007). Neurology 78, S08.007-S08.007 (2012). 5. Viaccoz, A. et al. Clinical specificities of adult male patients with NMDA receptor antibodies encephalitis. Neurology 82, 556–563 (2014). 6. Miao, A. et al. Analysis of Relation Between Electroclinical Features and Cerebrospinal Fluid Antibody Titers in Patients With anti-NMDAR Encephalitis. Clin. EEG Neurosci. 50, 56–62 (2018). 7. Gegenhuber, B., Wu, M. V., Bronstein, R. & Tollkuhn, J. Gene regulation by gonadal hormone receptors underlies brain sex differences. Nature 606, 153–159 (2022). 8. Cyr, M. et al. Ovarian steroids and selective estrogen receptor modulators activity on rat brain NMDA and AMPA receptors. Brain Res. Rev. 37, 153–161 (2001).
Field-collected samples	No field collected samples were used in the study.
Ethics oversight	All animal experiments and care were performed in strict accordance with the Cold Spring Harbor Laboratory (CSHL) Institutional Animal Care and Use Committee (IACUC)

Note that full information on the approval of the study protocol must also be provided in the manuscript.

Plants

Seed stocks

N/A

Novel plant genotypes

N/A

Authentication

N/A

Flow Cytometry

Plots

Confirm that:

☒ The axis labels state the marker and fluorochrome used (e.g. CD4-FITC).

☒ The axis scales are clearly visible. Include numbers along axes only for bottom left plot of group (a 'group' is an analysis of identical markers).

☒ All plots are contour plots with outliers or pseudocolor plots.

☒ A numerical value for number of cells or percentage (with statistics) is provided.

Methodology

Sample preparation

For mouse tumor or tumor-draining lymph node scRNAseq suspensions - dissected tumors were minced and dissociated with the Tumor Dissociation Kit (Miltenyi Biotec, 130-096-730) and the gentleMACS Dissociator (Miltenyi Biotec) according to the manufacturer's protocol. For human tumor scRNAseq suspensions - viably frozen tumors were thawed and dissociated with the Tumor Dissociation Kit (Miltenyi Biotec, 130-095-929) and the gentleMACS Dissociator (Miltenyi Biotec) . After RBC lysis, cells were resuspended in flow cytometry buffer (PBS with 2% FBS) and incubated in Fc blocking buffer (mouse or human). Cells were then washed and stained with corresponding antibodies (+/- labeled NMDAR) in the dark for 30 minutes. For DOX-treated 4T1-NMDAR cells, To prepare cells for flow cytometry, adherent cells were trypsinized and then the trypsin was neutralized with serum-containing media before cells were resuspended in flow cytometry buffer (PBS with 2% FBS).

Instrument

For tumor scRNAseq sorting - Sony SH800. For flow cytometry on DOX-treated 4T1-NMDAR cells - Guava EasyCyte. For flow cytometry on mouse and human tumor suspensions - Dual Fortessa Cell Analyzer.

Software

For tumor scRNAseq sorting - Sony Cell Sorter Software. For flow cytometry on DOX-treated 4T1-NMDAR cells - Guava InCyte software. For flow cytometry on mouse and human tumor suspensions - BD FACSDiva software.

Cell population abundance

For tumor scRNAseq sorting of NMDAR-reactive B cells, sorting was performed in 'semi-purity' mode which is expected to yield cell purity above 97%. To characterize other components of the tumor microenvironment, this pure fraction was mixed with CD45-negative cells. For flow cytometry of DOX-treated 4T1-NMDAR cells, and flow cytometry analysis of mouse and human tumor suspensions, no sorting was performed, only phenotypic analysis.

Gating strategy

Gating strategy for intratumoral cell populations are displayed in Fig. S5a, Fig. S6a and Fig. S65a. Briefly, putative cells (cf. debris) and singlets were identified from FSC-A/SSC-A plots and FSC-A/FSC-H plots, respectively, using a standard gating approach. Live cells were identified from histograms of log-scaled LIVE/DEAD Violet staining according to the manufacturer's protocol, selecting the lower peak of the bimodal distribution. For the CD45, CD86, IgD, CD138, CD3 and CD19 channels, negative cells and positive cells were selected as the lower and higher peaks of the bimodal distribution, respectively. For the PE channel, reflecting capture of labeled NMDAR, we manually selected the tail of the distribution.

☒ Tick this box to confirm that a figure exemplifying the gating strategy is provided in the Supplementary Information.